Ollscoil na hÉireann, Corcaigh
NATIONAL UNIVERSITY OF IRELAND, CORK

An Investigation of High-*k* Materials in Metal-Insulator-Metal Capacitor Structures

A Thesis Presented to

The National University of Ireland, Cork

For the Degree of Doctor of Philosophy

By

Barry James Hutchinson BA (Mod)

College of SEFS,
Tyndall National Institute,
University College Cork.

April 2017

Head of Department: Professor Paul Ross
Supervised by Dr Ian M. Povey, Prof. Paul K. Hurley & Dr Scott Monaghan

Table of Contents

Declaration

This is to certify that the work I am submitting is my own and has not been submitted for another degree, either at University College Cork or elsewhere. All external references and sources are clearly acknowledged and identified within the contents. I have read and understood the regulations of University College Cork concerning plagiarism

_____

Signature of author

_____

Date

Table of Figures

Table of Tables

Acknowledgments

First of all, I would like to extend my sincerest gratitude to my supervisors, Dr Ian Povey, Professor Paul Hurley and Dr Scott Monaghan for this research opportunity at the Tyndall National Institute. In particular, I would like to give special thanks to Dr Ian Povey for his support, advice and direction during my time at Tyndall. In addition, a special thanks to Dr Mircea Modreanu for his great advice and support in many aspects of my research and, in particular, his Raman work that is contained in this thesis.

Most importantly I would like to thank my partner Aoife (and our new arrival, little Tadhg) for her patience, support and belief during my academic journey over the last many years. Additionally, a special thank you for my parents for all of their help throughout my life. Furthermore, I would like to sincerely thank Professor Jonathan Coleman for enabling me to start my higher education journey and for his encouragement in those early years. In addition, special thanks to Professor Donall Mac Donaill for all of his help and advice during my early academic years.

A special thanks to Adrian Walsh for his help, friendship and advice, especially during stressful occasions. Furthermore, I would like to thank Dr Patrick Harnedy, Dr Gerard Duffy, Dr Brendan Sheehan, Dr Jack Bates, Dave Pierce and Dr Patrick Carolan for their friendship and advice over many years. In addition, I would like to thank all members of both the Advanced Materials and Surfaces Group and the Nanoelectronic Material and Devices Group, both past and present including Dr

Shane O'Brien, Dr Karim Cherkaoui, Dr Éamon O'Connor, Dr Richard Winfield, Melissa McCarthy, Louise Ryan, Igor Kazadojev, Dr Vladimir Djara and Mary-Claire O'Regan who have all contributed to making my time spent at Tyndall a very enjoyable experience.

Particular thanks to Dr Patrick Carolan, Dr Brendan Sheehan for the microscopy work which is contained in this thesis and to Dan O'Connell for device fabrication. Furthermore, special thanks to Dr V. S. Teodorescu and Dr R. Negrea for their microscopy work that is contained in this thesis.

The FIB / TEM sample characterisation in this thesis was performed by Dr Brendan Sheehan, Dr Patrick Carolan, Dr V. S. Teodorescu and Dr R. Negrea.

The EDX sample characterisation in this thesis was performed by Dr V. S. Teodorescu and Dr R. Negrea.

The Raman sample characterisation in this thesis was performed by Dr Mircea Modreanu.

The irradiation of samples in this work was performed by the European Space Agency.

Barry Hutchinson was awarded a studentship under the framework of the Irish Government's Programme for Research in Third Level Institutions Cycle 5, National Development Plan 2007-2013 with the assistance of the European Regional Development Fund.

Abstract

Metal insulator metal (MIM) capacitors are vital components of many devices such as various communication band beamformers, analogue to digital conversion, micro-electromechanical systems, medical, automotive, RF communication IC's and dynamic random access memory (DRAM) applications. Current MIM capacitors technology utilises low dielectric constant (*k*) materials (*k*~3.9 - 7), however, these materials achieve the required electrical properties of high electric field breakdown strength and minimal leakage current. Furthermore, aggressive scaling is critical for the technological needs of applications such as DRAM cells where continual scaling is required for increased performance and density. The low *k* value of the current materials presents a substantial risk to the future development of many technologies and the integration of high-k materials in MIM capacitor structures has become absolutely vital to achieve scaling needs

In this work we investigate the electrical properties of a hafnium silicate material system in MIM capacitors with sputtered aluminium electrodes. A conduction mechanism study of both interfaces was performed and an investigation of the dielectric reliability was carried out using the time dependent dielectric breakdown methodology. The reliability results were analysed using Weibull statistics and the material was determined to have excellent reliability characteristics.

In addition, further samples of the above hafnium silicate capacitors were irradiated with total radiation dosages of 16 krad(Si) and 78 krad(Si) which were equivalent to shielded and unshielded total dosages for LEO satellites respectfully. The electrical properties of both samples were characterised and their reliability characteristics were determined. The shielded sample was determined to have excellent radiation hardness and the unshielded sample displayed a minor decrease in overall performance.

Furthermore, we investigate the growth of hafnium silicate films by plasma assisted atomic layer deposition on a metal electrode and compare with a previous growth study performed under experimental parameters that differ only in the nature of the substrate. Previous films were found to exhibit excellent electrical properties over a range of substrate materials and were consistent with hafnium silicate. In this study the dielectric growth was heavily influenced by the bottom electrode material. High resolution transmission electron microscopy (HRTEM) analysis and Raman spectroscopy indicate that the main crystalline phase is monoclinic HfO_2 with a k value of ~18. Despite the crystalline nature of the HfO_2 no hysteresis was observed in the capacitance voltage measurements. The scanning transmission electron microscopy (STEM) analysis also reveals the presence of nanoparticles, located primarily towards the lower platinum metal layer at the HfO_2 grain boundaries. Based on energy-dispersive x-ray spectroscopy (EDX) analysis the nanoparticles are consistent with silicon oxide inclusions.

Finally, preliminary observations by in-situ spectroscopic ellipsometry of the atomic layer deposition (ALD) of dielectric materials on a range of substrates. It was observed that the initial phases of thermal HfO_2 ALD is inhibited by the presence of

native oxides. For the growth of HfSiOx by plasma enhanced ALD a more complex mechanism suggested a two stage nucleation process where nucleated silicon precursor inhibits further growth.

1. Introduction

1.1 Overview

Ultra large scale integrated circuit (ULSI) technology has benefited from the continuous scaling of active devices such as the MOSFET for many decades. Passive devices such as capacitors, resistors and inductors were not a significant component of ULSI technology and, therefore, the same aggressive scaling was not as necessary. However, many integrated circuits (IC) such as radio frequency (RF), analogue mixed signal (AMS), filter and converter applications rely on passive components such as capacitors, resistors and inductors. These passive components can take up large areas in IC's as shown below in Figure 1.1.

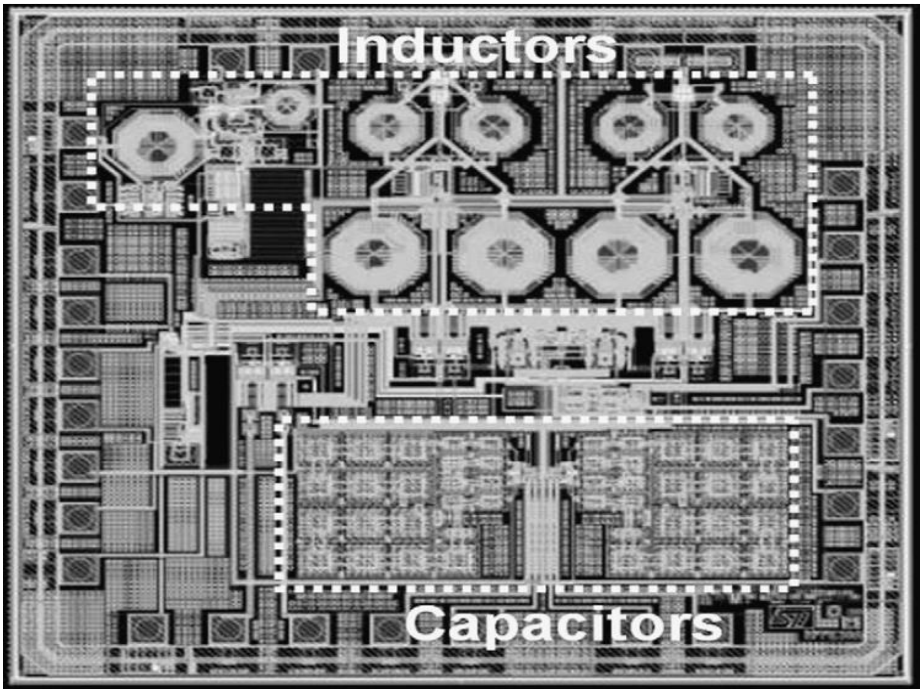

Figure 1.1 The large amount of area occupied by Metal-Insulator-Metal (MIM) capacitors and inductors is shown in this RF reception circuit for mobile phones [1].

These technologies have come to the fore in recent times due to the growth of the markets in mobile devices and wireless communications. Hence, the drive to low cost, low power multi standard chips that are capable of operating across multiple communication protocols, signal conditions and battery status with the lowest power dissipation possible. However, current transistor scaling alone cannot achieve this and further integration of analog technology with CMOS processes is necessary to accomplish gains through technologies such as System-on-Chip (SoC) which enables the integration of an entire electronic system in a chip or multiple chips, system-in-package (SiP) [2]–[4].

Furthermore, in SoC or SiP based wireless communication systems analog signal processing is being replaced by digital signal processing and there is a push to more digital circuitry in general with replacement of analog systems with digital based solutions to increase speed and reduce cost. An additional benefit of this trend is to improve programmability and reconfigurability of systems such as radio sytems [5], [6]. Additionally, the benefit from digital signal processing encourages further replacement of traditional components with CMOS technologies and it has been predicted that future wireless communication SoC's will comprise of mostly CMOS compatible technologies [7], [8]. The performance of passives such as capacitors in RF and AMS devices quite often determines the overall performance and integrating these passives in to SoC's or SiP's is critical for future scaling needs and cost reduction. However, passive components in CMOS technologies tend to be inferior in terms of precision and cost [9]–[11]. Capacitors are the most commonly used passive and for many years SiO_2 with a dielectric constant (k) = 3.9 [12] or Si_3N_4 (k = 7 [13])

were the dielectric in the capacitor components of RF and AMS IC's, and increases in capacitance density was achieved through increasing the area of capacitors or reducing the dielectric thickness. However, this has physical limits with regard to available area within the IC and permissible levels of leakage current. Hence, new dielectric materials with higher dielectric constants that are CMOS compatible are needed to achieve integration of surface mounted capacitors and the requirements for the integrated capacitors are the same as the surface mounted variants. The Metal-Insulator-Metal (MIM) capacitor is a simple parallel plate structure as shown in Figure 1.2.

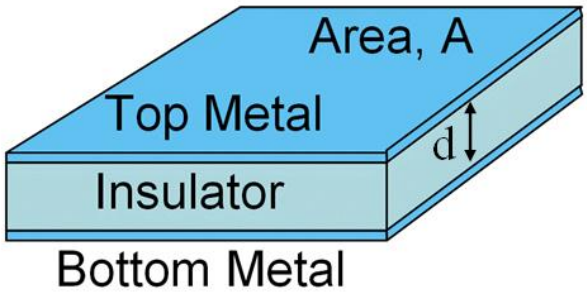

Figure 1.2 Schematic of parallel plate MIM capacitor.

They are preferential for RF and AMS since Metal-Oxide-Semiconductor and Polysilicon-oxide-Polysilicon capacitors suffer from large electrode resistance, depletion effects and low quality factor due to capacitance loss to the substrate [14]–[17], which results in limited RF capability in the GHz range [18]. An example of integrated MIM capacitors in 0.18 μm SiGe BiCMOS technology is shown in Figure 1.3 below where the MIM capacitors have been integrated in to the BEOL process.

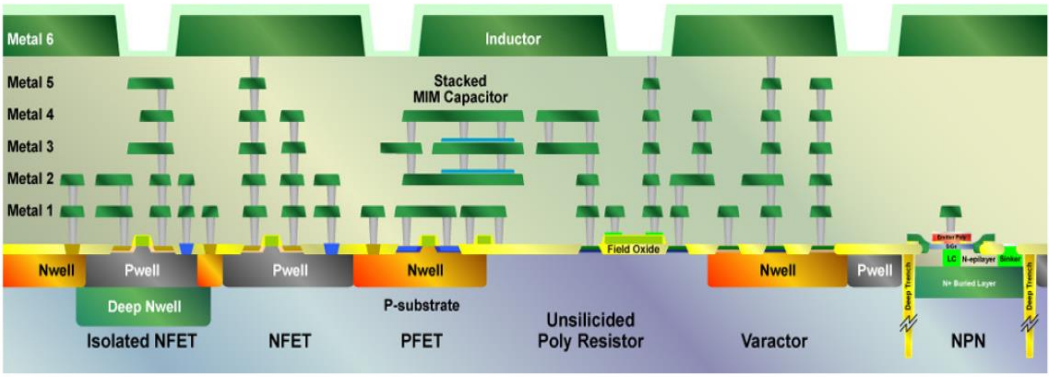

Figure 1.3 Schematic cross section of 0.18 um SiGe BiCMOS technology with stacked Si3N4 based MIM capacitors with a capacitance density of 2.8 fF/μm² each [19].

1.2 Embedded Passive Technology Parameters

The key parameters for MIM capacitors that are relevant to RF and AMS are capacitance density, leakage current, voltage linearity, quality factor, temperature linearity and matching. The future requirements for RF MIM capacitors according to the ITRS roadmap (2012) are below in table 1 [20].

Table 1-1 ITRS roadmap (2012) Embedded passive technology requirements [20].

Production Year	**2017**	**2018**	**2019**	**2020**	**2021**	**2022**	**2023**	**2024**	**2025**	**2026**
MIM Capacitor										
Capacitance Density (fF/μm²)	**7**	**10**	**10**	**10**	**12**	**12**	**12**	**12**	**15**	**15**
Voltage linearity (ppm/V²)	**<100**	**<100**	**<100**	**<100**	**<100**	**<100**	**<100**	**<100**	**<100**	**<100**
Leakage current (A/cm²)	**<1e-8**	**<1e-8**	**<1e-8**	**<1e-8**	**<1e-8**	**<1e-8**	**<1e-8**	**<1e-8**	**<1e-8**	**<1e-8**
σ Matching (%μm)	**0.3**	**0.2**	**0.2**	**0.2**	**0.2**	**0.2**	**0.2**	**0.2**	**0.1**	**0.1**
Q (5 GHz for 1 pF)	**>50**	**>50**	**>50**	**>50**	**>50**	**>50**	**>50**	**>50**	**>50**	**>50**
Manufacturable solutions known										
Manufacturable solutions NOT known										

Furthermore, the high-*k* material must be CMOS compatible with no cross contamination and an additional constraint of a thermal budget below 400˚C for back end of line (BEOL) integration [1]. Additionally, and perhaps most importantly, a guaranteed lifetime of 10 years is required for most terrestrial electronic applications and an increased lifetime is generally required for space applications. Hence, the reliability physics of any candidate high-*k* material must be thoroughly characterised, especially, since reliability characterisation usually involves accelerated testing methods and the extrapolation of their results to operational conditions. Each of these parameters is discussed in more detail below after a brief overview of MIM capacitor physics.

1.3 MIM capacitor physics

Parallel plate capacitor physics are discussed below since integrated MIM capacitors are parallel plate capacitors. This type of device is a charge storage device composed of two conducting plates and an insulator between them. The capacitance (C) which is measured in Farads (F) of this device is fundamentally related to the charge (Q) on each plate and the voltage (V) applied across them as follows.

$$Q = CV \qquad (1)$$

The charge on the plates with a vacuum (or ~ air) insulator is related to ε_0, the permittivity of free space. Placing other insulating material between the plates of a capacitor which were connected to a voltage source was found to increase the charge

on the plates [21]. This increase in charge was by a factor of ε_r or *k* (relative permittivity or dielectric constant or *k* value) compared to a vacuum. The permittivity (ε) of a material is a measure of its ability to polarise in the presence of an electric field which effectively reduces any field set up in it. The value of the permittivity can vary significantly with the frequency of the ac component of the electric field for most materials due to the different mechanisms of polarisation such as orientational, ionic and electronic. The direction of the polarisation will change with the direction of the electric field and this realignment does not occur instantaneously. Each mechanism eventually ceases to contribute to the permittivity as the frequency increases, typically ~ 10^{11} Hz, ~ 10^{13} Hz and ~ 10^{15} Hz for orientational (dipole), ionic and electronic respectively. Hence, above ~ 10^{15} Hz the dielectric constant is equal to that of a vacuum.

The ratio of the permittivities of a given material to a vacuum is the dielectric constant. Hence, *k* is related to ε_0 as follows.

$$\kappa = {}^{\varepsilon}/_{\varepsilon_0} \qquad (2)$$

In an ideal situation where the electric field lines between the capacitor plates are straight lines (ie: no edge effects), the plates are infinitely large and planar symmetry is assumed, we can calculate the electric field using Gauss's law as follows.

$$\Phi = \oint_A \vec{E}\, d\vec{A} = {}^{q_{enc.}}/_{\varepsilon_0} \qquad (3)$$

where Φ is the electric flux, $\vec{E}$ is the electric field vector, $d\vec{A}$ is the surface vector and q_{enc} is the enclosed electric charge. The electric field is related to the electric flux as follows.

$$E = \frac{\Phi}{A} = \frac{q_{enc}}{A\varepsilon_0} = \frac{CV}{A\varepsilon_0} \qquad (4)$$

The electric field is related to voltage and distance between the plates (d) as follows.

$$E = \frac{V}{d} = \frac{CV}{A\varepsilon_0} \qquad (5)$$

Rearranging for C allows for the determination of capacitance for a parallel plate capacitor with a vacuum and the addition of *k* allows for the inclusion of other dielectric materials. Also, capacitance density (C_D) is capacitance divided by area and is a commonly used for comparing the capacitance of MIM capacitors.

$$C = \frac{\varepsilon_0 A}{d} \qquad (6) \qquad C = \frac{\kappa\varepsilon_0 A}{d} \qquad (7) \qquad C_D = \frac{\kappa\varepsilon_0}{d} \qquad (8)$$

Capacitance equivalent thickness (CET) allows for the comparison of electrical properties of high *k* dielectrics directly with SiO_2 as described below.

$$CET = \frac{A\kappa_{SiO_2}\varepsilon_0}{C_{Meas}} \qquad (9)$$

where κ_{SiO_2} is the dielectric constant of SiO_2 and C_{Meas} is the experimentally measured capacitance. The value of CET is that it estimates the thickness of SiO_2 to provide the same capacitance and allows direct comparison. However, if there is an interface layer present between the high *k* dielectric and the metal electrode the

calculation of CET requires modification. Firstly, the interface and high *k* layers can be treated as capacitors in series as below [22]–[24].

$$\frac{1}{C_{Tot}} = \frac{1}{C_{High-\kappa}} + \frac{1}{C_{Int}} \qquad (10)$$

where C_{Tot}, $C_{High-\kappa}$ and C_{Int} are the total, high *k* and interface capacitances respectfully. Then the CET equation is modified as follows.

$$CET = \frac{A\kappa_{SiO_2}\varepsilon_0}{C_{To\square}} = A\kappa_{SiO_2}\varepsilon_0\left(\frac{1}{C_{High-k}} + \frac{1}{C_{Int}}\right) = \frac{\kappa_{SiO_2}}{\kappa_{High-k}}\left(d_{High-k}\right) + \frac{\kappa_{SiO_2}}{\kappa_{Int}}\left(d_{Int}\right) \quad (11)$$

The contribution from the interface layer is very much dependent on the difference in *k* between it and the high *k* layer and of course the thickness of each layer. However, interface layers tend to be very thin; therefore, the *k* value differential will mostly determine the influence the total capacitance. Although, interfaces are best avoided if possible due to the negative impact on capacitance and more generally, electrical properties.

1.4 Capacitance Density

It is obvious from equation (8) that the *k* value must increase or d must decrease to boost the C_D. Although, as the *k* value increases generally the band gap decreases, Figure Figure 1.4 (top), and this may result in increased leakage current. Also, there is empirical evidence of a strong trend that indicates the breakdown strength (E_{BD}) of the dielectric decreases with increasing k ($E_{BD} \sim k^{-0.5}$), Figure 1.4 (bottom), and this may reduce the voltage operational range. This trend is also predicted by the thermochemical model [25].

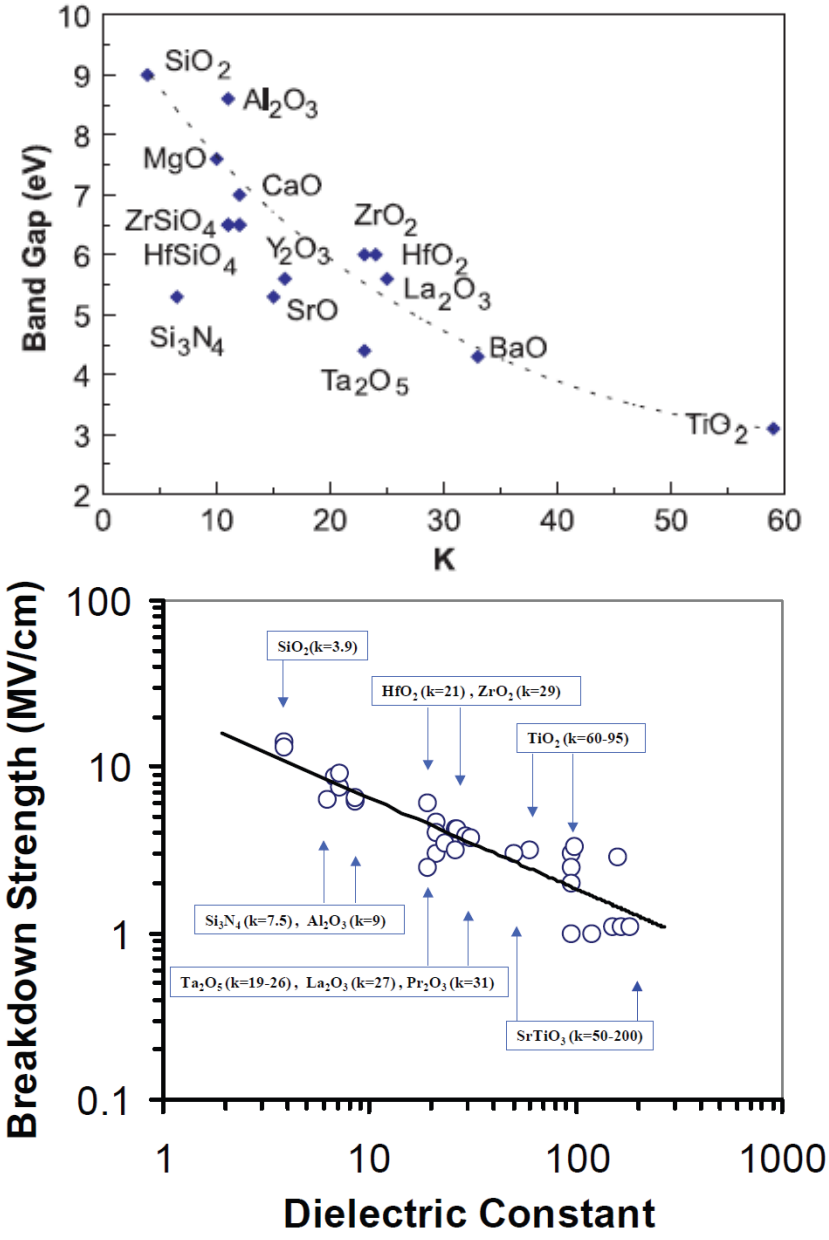

Figure 1.4 (top) Band gap versus k for several dielectrics [26] and (bottom) there is a strong correlation (0.81) over a diverse range of dielectrics between Breakdown strength E_{BD} versus dielectric constant k ($E_{BD} \sim k^{-0.5}$) [27]. This trend of breakdown strength as a function of k is predicted by the Thermochemical model [25].

Decreasing the dielectric thickness, d, will increase C_D, however, this will also increase the voltage coefficients of capacitance (VCC) and the leakage current.

The level of crystallinity and grain size in the thin film will greatly affect *k* and the leakage current. Hence, ideally a trade off is necessary between increasing *k* and decreasing d to achieve the desired C_D for the industry roadmap.

1.5 Leakage current

The acceptable level of leakage current will be determined by the application and this in turn will establish the maximum operational voltage range for a MIM capacitor. Generally, tunnelling leakage mechanisms are not an issue at the thicknesses used for RF or AMS MIM capacitors applications. However, Schottky and Poole-Frenkel conduction mechanisms are commonly observed in high-*k* dielectrics.

Thermionic Emission is the emission of a carrier over the dielectric barrier in to the conduction band of the dielectric. It is called Schottky emission when it happens in the presence of an electric field that effectively lowers that barrier to the conduction band of the dielectric due to the image charge theorem.

Schottky emission is described as follows

$$J_{SE} = AT^2 exp\left(\frac{-q(\phi_B - \sqrt{qE/4\pi\varepsilon_0\varepsilon_r})}{k_B T}\right) \qquad (12)$$

where J_{SE} is the Schottky current density, A is the effective Richardson coefficient, q is the elementary charge, ϕ_B is the Schottky barrier height, E is the electric field, ε_0 is the vacuum permittivity and ε_r is the dynamic dielectric constant. Schottky emission was observed as the dominant leakage mechanism in many MIM capacitor systems such as $SrTiO_3$ and $Ho_2Hf_2O_7$ [28], [29].

Poole-Frenkel has been observed as the dominant conduction mechanism in dielectrics with a large trap density where tunnelling conduction mechanisms have been disregarded due to the thickness of the dielectric. The traps hamper the transport of electrons in the conduction band of the dielectric by trapping and de-trapping them and hence moderating the current.

Poole-Frenkel emission is described as follows

$$J_{PF} = CEexp\left(\frac{-q(\phi_t - \sqrt{qE/\pi\varepsilon_0\varepsilon_r})}{\xi k_B T}\right) \qquad (13)$$

where J_{PF} is the Poole Frenkel current density, C is the pre-exponential factor, ξ is a factor that depends on acceptor compensation which is commonly set to 1 [30]–[32], and ϕ_t is the trap energy level below the conduction band. Poole-Frenkel has been observed as the dominant conduction mechanism in HfO_2 [33], [34].

1.6 Voltage linearity

The non-linear change in capacitance with voltage can be analysed by fitting $\Delta C/C_0$ versus V with a second order polynomial as shown below [35].

$$C(V) = C_0(\alpha V^2 + \beta V + 1) \qquad (14)$$

where α and β are quadratic and linear voltage coefficients of capacitance (VCC) respectively. Circuit design can reduce the linear VCC β to an acceptably low level [36], [37]. However, there is no similar way to reduce the quadratic VCC α and as such this is an important parameter for certain applications such as analog to digital

(ADC) or digital to analog converters. An illustration of the magnitude of the error associated with the quadratic VCC is shown below in Figure 1.5 for an ADC and this may affect the accuracy of the converter.

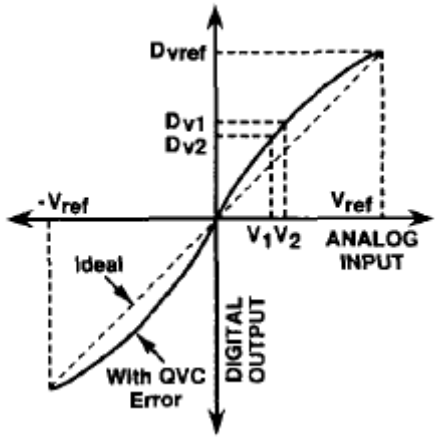

Figure 1.5 An illustration of how the quadratic VCC α parameter affects ADC transfer curves [37].

The ITRS roadmap specifies a value for α (< 100 ppm/V^2) as shown above in table 1. α tends to increase significantly with decreasing film thickness, an empirical relationship of $\alpha \propto d^{-n}$ has been observed for many high *k* materials including HfO_2 and Al_2O_3 [15], [16], [38]–[44]. There have been many models proposed for the origin of the quadratic VCC α, such as electrode polarization, the ionic motion of metal ions between different lattice sites, temperature dependent movement of rotating dipoles, ionic polarisation, the electrostriction model, a thermodynamic model based on entropy change and an electron hopping vacancies model [42], [45]–[51]. However, the origin of the mechanism currently remains an open question.

1.7 Quality factor

The quality factor (Q) is essentially the ratio of energy stored to energy losses per cycle in a capacitor and the reciprocal of the dissipation factor (tan δ). These losses can be attributed to equivalent series resistance (ESR or R_s) in which the energy is lost as heat, Q and R_s are related as follows.

$$Q = \frac{X_C}{R_S} = \frac{1}{\tan \delta} \qquad (15)$$

where X_C is the reactance of the capacitor. Q also reduces with increasing frequency.

1.8 Reliability

Reliability can be thought of as a measure of the ability of an item to perform required functions for the prescribed period under operational conditions. Therefore, reliability measurements are a function of time. In the semiconductor industry the time dependent failure rate of devices follows a "bathtub curve" which can be seen in Figure 1.6 below. The three regions of the curve are classified as: early, constant and wear-out failure regions. This curve is the sum of the early failure rate which decreases steadily over time, the random failure rate which exhibits a constant value, and the wear-out failure rate which increases steadily over time. The area of interest is the wear-out region which can be attributed to the time dependent dielectric breakdown (TDDB) mechanism when considering MIM capacitors [52].

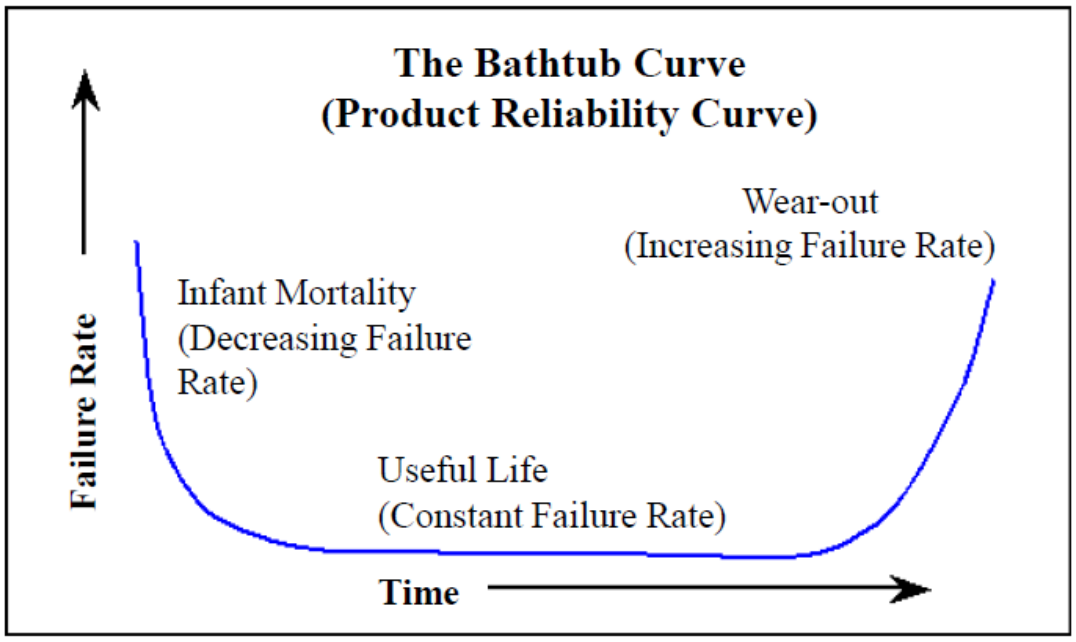

Figure 1.6 Time dependent failure rate of semiconductor devices.

1.8.1 TDDB Models

There have been several models suggested to account for TDDB in gate oxides over many years: the E model [53]–[55], the 1/E model [56]–[58], the power law model [59] are the most popular while more recently the $\sqrt{E}$ [60], $1/\sqrt{E} + \sqrt{E}$ [61] and E^2 [62] have been proposed based on different physical mechanisms that may lead to TDDB. Two models have been suggested for the reciprocal field model and both are based on electron injection through Fowler-Nordheim tunnelling, hence, these models are not considered due to the dielectric film thickness (~ 120 nm) under investigation. The Power Law model results in an exponential extrapolation of the lifetime from high electric field test measurements to low field operating conditions which has been shown to adequately describe thin high-*k* gate oxides in recent times [63]–[65]. However, the E model has been chosen for this analysis as it results in a more

conservative lifetime and has been applied most frequently in the literature to describe TDDB behaviour in dielectrics for several decades. The E model is described as follows

$$t_{BD} = t_0 e^{-\gamma E} \qquad (16)$$

where t_{BD} is the time to electrical breakdown, t_0 is an arbitrary scale factor, dependent upon materials and process, E is the electric field, and γ is the field acceleration parameter.

The E model is based on many decades of research on SiO_2 and it is assumed that the dielectric breakdown is a thermodynamic process and the electric field interacts with the weak silicon-silicon bonds that arise from oxygen vacancies. The applied electric field eventually breaks the bond and creates a permanent defect [66]–[68]. This leads to a silicon atom with a localised unpaired electron that's also bonded to three oxygen's [69]. The log of the mean time to failure (MTTF) is observed to be linearly dependent on electric field. The statistical distribution of TDDB can also be described by the percolation of randomly generated defects in an applied electric field that leads to a conduction path in the dielectric [52]. Two models have been suggested for the reciprocal field model and both are based on electron injection through Fowler-Nordheim tunnelling. The first one [57], [70], [71] assumes that holes can then be produced through impact ionization and they result in an increase in the local electric field. Hence, an avalanche effect of more electron injection and more hole generation is followed by dielectric breakdown. The second one [55], [58], [72] suggests that the tunnelling electrons transfer energy to holes at the anode and they are injected

(tunnel) into the dielectric. In this case the lifetime is predicted to be dependent on the reciprocal of the electric field. The statistical distribution of TDDB can also be described by the percolation of randomly generated defects in an applied electric field that leads to a conduction path in the dielectric [52].

1.8.2 High-*k* Reliability Issues

High-*k* materials generally suffer from high leakage current densities, variations in leakage mechanisms, low breakdown fields, soft breakdowns prior to hard breakdown, poor temperature stability and non-linearity of capacitance. Their electrical properties can fluctuate with varying film thickness, frequency and temperature [73]. They tend to have high defect densities including oxygen vacancies that allow leakage current to flow through a hopping mechanism. These oxygen vacancies have also been linked to the non-linearity of capacitance in MIM capacitors [74]. The bonding in high-*k* dielectrics is generally ionic (such as in HfO2) and these bond energies are much weaker than the covalent bonds found in low-*k* dielectrics (such as in SiO2). This weaker ionic bonding structure may lead to the generation of oxygen vacancies and hence the bonding structure may be partly responsible for the inferior properties of high-*k* materials [75]. It has been proposed theoretically that oxygen in silicate materials covalently exists adjacent to the Si atom, consequently the ionic bonding nature is reduced and the covalent bonding nature is increased [23], [75], [76]. Therefore this increased covalent bonding structure may lead to more stabilised oxygen in the silicate material lattice [75].

The reliability models described previously are intended for application to low-*k* SiO2 systems over a large range of film thicknesses. Models to effectively describe high-*k* systems in which the bonding has a larger ionic component, compared to SiO_2, are unknown and still a matter of debate [77].

1.8.3 Analysis of reliability data

Constant voltage stress (CVS) measurements until dielectric breakdown are carried out on the sample of interest to investigate its reliability. A broad range of time to breakdown (t_{BD}) values can be expected when multiple samples of the same oxide are stressed under identical conditions in capacitor structures. This range of t_{BD} values is statistical in nature due to the effect of the random traps that may lead to the formation of a conduction path between the electrodes. This statistical distribution is commonly described by a 2 parameter Weibull cumulative distribution function which is defined as follows

$$F(t) = 1 - exp\left[-\left(\frac{t}{n}\right)^{\beta}\right] \qquad (17)$$

where t is time, $F(t)$ is the cumulative failure with time (unreliability function), n is the scale factor which is the time taken for 63% cumulative failure of the sample set and β is the shape parameter (slope) of the distribution [78]–[80].

The above equation is linearised as follows.

$$\ln\left[-\ln\left(1 - F(t)\right)\right] = \beta \ln(t) - \beta \ln(n) \qquad (18)$$

Then plotting $\ln\left[-\ln\left(1-F(t)\right)\right]$ versus $\ln(t)$ achieves a linear fit of which the slope is β and then n can be calculated for 63% cumulative failure (n_{63}) from the y intercept. There are a number of ways to estimate the parameters, β andn_{63}, such as Least Squares method, however, maximum likelihood estimation (MLE) is commonly chosen. The MLE results in more accurate values by being weighted in favour of where breakdown is more prevalent in the distribution.

1.9 Atomic layer deposition

The continuous scaling requirement of the semiconductor industry roadmap has increased the need for the conformal deposition of nanometre scale pinhole free films of high-k dielectric oxides for planar and high aspect ratio CMOS transistors and MIM capacitors [81]. Well defined and controlled film properties at these thicknesses require an understanding of both the nucleation on appropriate substrates and the bulk growth process. Presently, atomic layer deposition (ALD) is one of the few candidate deposition technologies capable of delivering the precise growth control required [82]–[86]. An ALD cycle typically consists of two separate surface reactions that are self-limiting thus allow the control of film growth at the monolayer level. This self-limiting behaviour is often exploited by in-situ mechanistic studies as the process can be assumed to be in a steady state in the purge cycles between the ALD precursor pulses. We employ in-situ spectroscopic ellipsometry (SE) to examine the growth processes of Al_2O_3 and two high-k materials HfO_2 and $HfSiO_x$, in real time, on a range of technologically relevant substrates. In particular we focus on the nucleation

processes and highlight the influence of both process parameters and the nature of the substrate.

As already alluded to, an ALD cycle consists of two separate surface reactions that are self-limiting, thus once precursor pulses are in excess of saturation the growth per cycle (GPC) is determined by a combination of available surface adsorption sites, sticking coefficients and steric hindrance of ligands and their reaction products on the substrate surface. Hence, extremely accurate thickness control can be obtained in a well-controlled ALD process. In addition the self-limiting chemistry enables conformal growth even with high aspect ratios and complex geometries.

The two most popular types of ALD are thermal and plasma enhanced (PEALD), the thermal ALD process is the most studied and longest established while PEALD has gained momentum in recent years. In thermal ALD the surface reactions are driven purely by thermal energy whereby an increasing temperature gradient from precursor to substrate is utilised to maximise chemisorption and thus growth [86]. Similarly, PEALD utilises a more energetic oxidant in the form of oxygen plasma, this allows the thermal budget to be decreased further for ALD processes which, due to the high reactivity provided by the plasma, may enable the ALD of new material systems or improved material properties [87].

Generally, ALD film growth is considered to possess two regimes, nucleation and bulk growth. As nucleation may differ considerably depending on the substrate it is well recognised that the nucleation should be studied in detail. However, it is often

assumed that bulk growth proceeds at a constant rate irrespective of substrate. Such a hypothesis is not without problems; nucleation may lead to a bulk film of a particular phase (templating), mixed phases, or strain that may influence the bulk GPC. Also, other factors such as changes in reactor temperature, wall deposits, plasma characteristics and precursor condition and delivery can influence film growth at any point in the process. For this reason both the nucleation and bulk growth behaviours of ALD grown films require detailed study.

1.10 Spectroscopic Ellipsometry

SE is an important technique which enables the in-situ or ex-situ characterisation of thin films to determine the thickness and refractive index. It also allows insight in to the nucleation and growth regimes of thin film growth. SE measures the change in polarization as light reflects from and transmits through a material. Electromagnetic waves consist of an electronic component and a magnetic component orthogonal to each other. In SE it is only necessary to discuss the electric field behaviour in space and time, this is called polarization. SE uses linearly polarized light which when reflected off a sample changes polarization to elliptical as shown in Figure 1.7 (left).

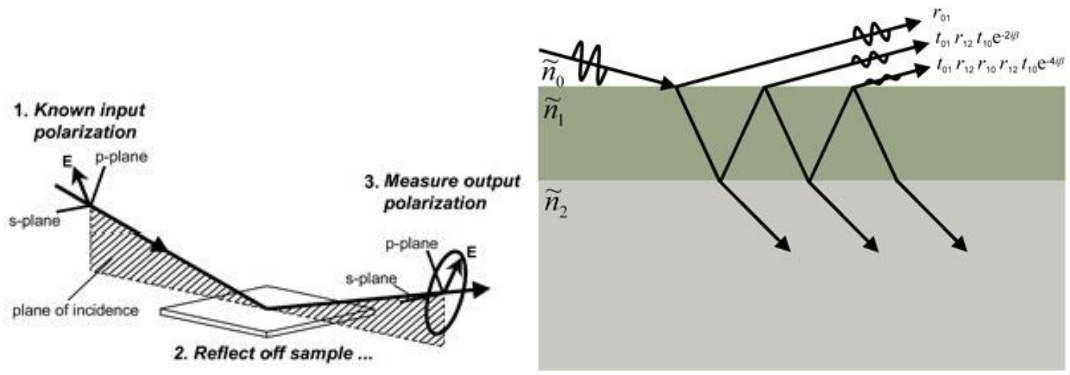

Figure 1.7 (left) Diagram showing a simplistic SE operation where the supplied polarized light reflects of the substrate's surface and changes polarization and then it can be collected by a detector for analysis. (right) Diagram of a more realistic sample where there are reflection and refraction at multiple interfaces within the various layers of a sample [88].

This change in polarization is represented as an amplitude ratio, Ψ, and the phase difference, Δ. The response of the material is dependent on its thickness and optical constants, Figure 1.7 (right), and this has been used to establish the thickness or optical constants of thin films [89], [90]. It is a non-invasive technique that has the sensitivity to possibly detect nominal thickness changes in the sub angstrom (0.1) measurement range and has been used in many studies in the literature [91]–[97]. The sensitivity of this optical technique complements its use as an in situ monitoring system for the growth of thin films by ALD.

1.11 High-*k* materials

There has been great interest in high-*k* dielectrics for many years and this has led to the successful integration of high-*k* metal gate in CMOS by Intel [98], [99]. Many high-*k* dielectrics have been investigated for RF and AMS MIM capacitor applications [100]–[107]. However, the progress has been slower for high-*k*

integration in MIM capacitors for analog electronics. The material systems can be categorised in to several types such as single layer binary and ternary or more metal oxides, and multilayered or stacked metal oxides. This section will give an overview of that research.

1.11.1 Single layer dielectrics

Al_2O_3

This binary oxide has low loss tangent, large band gap (8.7 eV), little frequency dispersion and a deposition temperature compatible with BEOL [108], [109]. However, it has a reasonably low *k* value ~ 8 to 9 and large quadratic VCC which limit its effectiveness for RF and AMS applications [43], [110], [111].

HfO_2

The advantages of HfO_2 are that it has a good *k* value ~ 15-25 within the CMOS thermal budget and its band gap is reasonable ~ 5.8 eV [110], [112], [113]. However, its quadratic VCC increases substantially as its thickness decreases. The quadratic VCC increased from ~ 238 ppm/V^2 to ~ 831 ppm/V^2 for film thicknesses from 30 nm to 10 nm, furthermore, low E_{BD} can be an issue for certain applications [38].

Ta_2O_5 and $SrTiO_3$

Both of these materials were originally considered for memory applications but they suffer from very high leakage currents due to the small band gaps, which leads to disproportionate leakage current increase with temperature when compared to SiO_2 or

Si_3N_4 [110], [114], [115]. Hence, they are not considered to be of practical use for RF and AMS applications as single layer dielectrics.

La_2O_3, Y_2O_3 and Sm_2O_3

Rare earth dielectrics have achieved high capacitance densities, 11.4 fF/μm^2, 8.5 fF/μm^2 and 7.5 fF/μm^2 in MIM capacitors [116]–[118]. However, the quadratic VCC values were very high, 671 ppm/V^2, 14100 ppm/V^2, 234 ppm/V^2 respectfully and not compatible for precision analog applications [116]–[118].

Single layer dielectric material systems that attempt to combine the best properties of two or more metal oxides have been investigated for RF and AMS applications over the years. TaZrO, $SrTiO_3$ achieved an excellent capacitance density of 12 fF/μm^2 and 44 fF/μm^2, though, they have large quadratic VCC 1236 ppm/V^2 and 3180 ppm/V^2 [119], [120]. However, the quadratic VCC of $SrTiO_3$ does decrease significantly with frequency, 54 ppm/V^2 at 2 GHz and 42 ppm/V^2 at 10 GHz, though, the E_{BD} ~ 1 MV/cm which may limit its applications [120]. MIM capacitors with sputtered $HfAlO_x$ have achieved high capacitance densities of 3.5 fF/μm^2 to 6 fF/μm^2, although, again the quadratic VCC values were relatively high, >100 ppm/V^2 and the devices suffered from high leakage current [121], [122]. It has been reported that HfLaO also suffers from a large quadratic VCC, >1000 ppm/V^2, for capacitance densities for 7.5 fF/μm^2 to 16 fF/μm^2 [123]. It is apparent that no single dielectric film meets all of the requirements of the ITRS roadmap [81].

1.11.2 Stacked dielectrics

Stacking two or more different dielectric films in a MIM capacitor has been investigated in numerous studies with the aim of achieving a device with better overall electrical properties by combining the best properties of the chosen dielectrics. Results from several of these investigations are shown in table 2 below.

Table 1-2 Comparison of stacked dielectric metal-insulators-metal capacitor systems. Adapted from [124].

Dielectric Stack	**d (nm)**	**C_D (fF/µm^2)**	**QVCC α (ppm/V^2)**	**J @ 1V (A/cm^2)**	**Deposition**	**Process Temp. (˚C)**
HfO_2/SiO_2 [125]	**12/4**	**6**	**14**	**$2.0x10^{-9}$**	**ALD/PECVD**	**420**
Sm_2O_3/SiO_2 [73]	**7.5/4**	**7.3**	**-46**	**$1.8x10^{-8}$**	**PVD/PECVD**	**420**
Er_2O_3/SiO_2 [126]	**8.8/3**	**7**	**-73**	**$4.2x10^{-9}$**	**PVD/MOCVD**	**400**
STO/ZrO_2 [127]	**20/20**	**11.5**	**-60**	**$3.5x10^{-8}$**	**PVD/MOCVD**	**550**
STO/Al_2O_3/ STO [128]	**25.5/1/ 25.5**	**19.1**	**610**	**$1.0x10^{-9}$**	**ALD**	**600**
ZTO/BZTO [129]	**17/7**	**13.4**	**14**	**$7.5x10^{-9}$**	**E-Beam**	**400**
SiO_2/HfO_2/ SiO_2 [130]	**3/4/3**	**12.4**	**32**	**$1.0x10^{-9}$**	**ALD**	**300**
Al_2O_3/SiO_2 [124]	**3.7/1.9**	**10.1**	**-20**	**$6.8x10^{-9}$**	**PEALD**	**200**
HfO_2/La_2O_3 [107]	**13 Total**	**20.8**	**101**	**$9.6x10^{-9}$**	**PLD**	**700**
$Si_3N_4/(Al_2O_3$/ HfO_2) [131]	**11.2/18.4**	**4.2**	**106**	**$1.01x10^{-8}$**	**PECVD/ALD**	**400**
Al_2O_3/ZrO_2/ SiO_2/ZrO_2/ Al_2O_3 [132]	**1/7/3/7/1**	**7.4**	**-121**	**$3.08x10^{-8}$**	**ALD**	**420**
ITRS 2020 [81]		**10**	**<100**	**$<1x10^{-8}$**		**400**

This approach has had some success such as the Al_2O_3/SiO_2 stack, table 2 above, which has good electrical properties and a CMOS compatible thermal budget. Although, the dielectric stacks in table 2 while representing some improvement on the requirements for meeting the ITRS roadmap, they still involve a compromise in terms of using complex materials, multiple deposition methods or thermal budgets incompatible with BEOL. The stack dielectric method appears to add considerable complexity to the MIM capacitor system and perhaps considerable cost.

1.11.3 $HfSiO_x$

Hafnium silicate is a CMOS compatible material system that can be deposited by ALD within BEOL thermal budgets and has the additional benefit of being an alloy of two of the most researched dielectrics. Many hafnium silicate material systems with varying ratios of Hf to Si have been investigated for use in MIM and MOS capacitors and have reported *k* values of ~ 10-11 [133]–[135]. However, the film properties including the *k* value are very dependent on the ratio of Hf to Si and the phase of the material [136]–[139].

It has been reported that MIM capacitors with a hafnium silicate dielectric containing a certain ratio of Hf to Si in a particular phase results in excellent electrical properties [140].

In this work we investigate the electrical characteristics of a single layer binary oxide material system ostensibly single crystal $HfSiO_4$ (Hafnon, equal ratios of Hf to Si).

Hafnon, has been previously synthetically grown by a high temperature furnace method and, thus, not suitable for electrical characterisation [141], [142].

1.11.4 New High-k Material System

It has been reported that a new material system, $M_xSi_{1-x}O_2$, has been proposed for capacitor, electronic or memory devices [140]. The material system has a high-*k* value combined with an low bulk quadratic VCC, low leakage current density at operation voltage, low deposition temperature compatible with CMOS processes, a low quadratic VCC|, high E_{BD} and negligible hysteresis or charge trapping. Furthermore, this material system may be radiation hard and suitable for space applications.

1.12 Motivation of the thesis

This thesis investigates the electrical properties and reliability of a promising patented high-*k* material system grown by ALD. The aluminium- $M_xSi_{1-x}O_2$-aluminium material system is electrically characterised in planar MIM capacitor structures through CV and IV analysis. Furthermore, electrical reliability characterisation is performed through TDDB analysis for terrestrial and space applications. Further characterisation of the material systems electrical properties are also investigated for ALD growth on various metal electrodes (aluminium, titanium tungsten alloy and platinum). Furthermore, a structural analysis of the platinum devices is performed,

and the nucleation and growth of dielectric material systems on various substrates is investigated by in-situ SE during ALD growth.

2. Reliability of Hafnium Silicate Grown by Atomic Layer Deposition on Sputtered Aluminium Electrode

2.1 Introduction

Metal insulator metal (MIM) capacitors are fundamental components of devices such as analogue to digital conversion, micro-electromechanical systems, medical, automotive and dynamic random access memory (DRAM) applications [40], [73], [143], [144]. MIM capacitors currently employ low dielectric constant (*k*) materials (*k*~3.9 - 7) to achieve the required electrical properties of high breakdown field and low current leakage. However, due to aggressive scaling that is required for applications such as DRAM cells for increased performance and density, the low *k* value of these materials presents a significant challenge to the future development [145] and it has become compulsory to integrate high-*k* materials to achieve scaling requirements.

In this chapter, we examine the electrical characteristics of a 120 nm hafnium silicate ($HfSiO_x$) film in MIM capacitors ($Al/HfSiO_x/Al$) on a SiO_2 isolation layer on a Si substrate. The main focus of the study was on the time dependent dielectric breakdown (TDDB) behaviour of the film under constant voltage stress (CVS). The accelerated lifetime test are conducted at high electric field and extrapolated to low field where the target is a minimum of 10 years TDDB device lifetime at 0.1 cm^2 0.01% cumulative failure. Some electron trapping was evident in the CVS

measurements beyond a certain voltage and this led to an investigation to identify the conduction mechanisms responsible.

2.2 Methods and Materials

MIM capacitors with Aluminium electrodes (top and bottom) and $HfSiO_x$ dielectric were fabricated by the following methods. The 120 nm $HfSiO_x$ film was grown by atomic layer deposition at 250˚C. The metal sources, Tetrakis(dimethylamino) hafnium and Tetrakis(dimethylamino) silane were pulsed simultaneously as the first half cycle with a remote oxygen plasma (300 W) pulse completing the cycle. The dielectric was deposited on to a sputtered bottom aluminium electrode on a high quality silicon dioxide isolation layer. The top aluminium electrode was deposited by an e-beam process. The devices defined by lift-off, were 1×10^{-8} m^2 in order to minimize extrinsic defects and determine the intrinsic oxide breakdown behaviour for the TDDB measurements.

Capacitance voltage (CV) measurements were recorded using an Agilent E4980a LCR meter following open-circuit calibration. Current voltage (IV) and CVS measurements were recorded using an Agilent 4156C precision semiconductor parameter analyzer. All electrical measurements were performed at room temperature in a micro chamber probe station Cascade Microtech, model Summit 12971B. Transmission electron microscopy (TEM) specimens for cross section analysis (XTEM) were prepared using the conventional method: gluing face to face small pieces cut from the area of interest using M-bond, followed by mechanical polishing and ion milling in a Gatan PIPS model 691 apparatus. TEM was performed using a

Jeol ARM 200F electron microscope, performing TEM imaging, high resolution (HRTEM).

2.2.1 Dielectric breakdown criteria

The dielectric breakdown criteria specifies that breakdown has occurred when a sudden exponential increase in the measured current (I_{Meas}) is detected. This current level should be carefully selected from multiple current voltage (JV) measurements. It is defined as an increase of 100 times I_{Meas}, due to the consistent catastrophic hard breakdown (short) associated with an exponential increase in leakage current in the high-*k* MIMCAP material system.

All data in this study was measured on the following devices, square MIM capacitors with an area of 10^{-4} cm^2 and 120 nm of $HfSiO_x$ between top and bottom aluminium electrodes.

2.3 Results and Discussion – Electrical Characterisation and Analysis

A TEM image of a cross section of a 1×10^{-8} m^2 MIM capacitor with the $HfSiO_x$ dielectric between top and bottom aluminium electrodes is shown in Figure 2.1 The $HfSiO_x$ layer appears to be amorphous and the measured physical film thickness of the $HfSiO_x$ layer is 120 nm with reasonably good thickness uniformity.

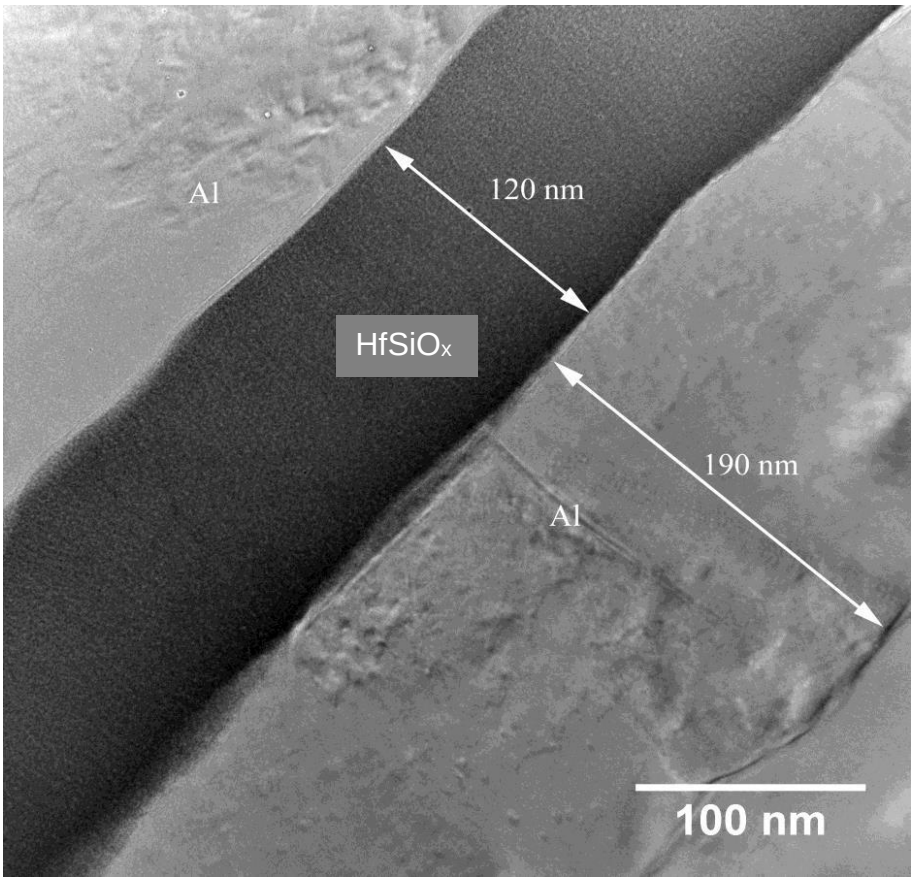

Figure 2.1 Cross-section TEM of a 120 nm thick hafnium silicate dielectric between aluminium electrodes, the structure appears amorphous and uniform.

Electrical characterization of the above sample was carried out and an overview of the results is shown in Figure 2.2 and Figure 2.3. There is negligible hysteresis and minimal frequency dispersion (<1%) from 1 kHz to 1 MHz evident in the capacitance density versus gate voltage (C_D-V_G) double sweeps in Figure 2.2 (left) and k ~ 13.2. However, the minimum capacitance in the CV sweep was offset by -3 V at 1 kHz, also, the offset reduced at higher frequency, -1 V at 1 MHz, and this would indicate the presence of positive charge in the dielectric, in the bulk or at the interfaces. The

non-linear change in capacitance with voltage can be analysed by fitting $\Delta C/C_0$ versus V with a second order polynomial [35]

$$C(V) = C_0(\alpha V^2 + \beta V + 1) \qquad (1)$$

where α and β are quadratic and linear voltage coefficients of capacitance respectively. The value of α (< 100 ppm/V^2) is important for certain applications such as RF or AMS. α tends to increase significantly with decreasing film thickness. The fit to the measured data in Figure 2.2 (right) resulted in α ~ 15 ppm/V^2.

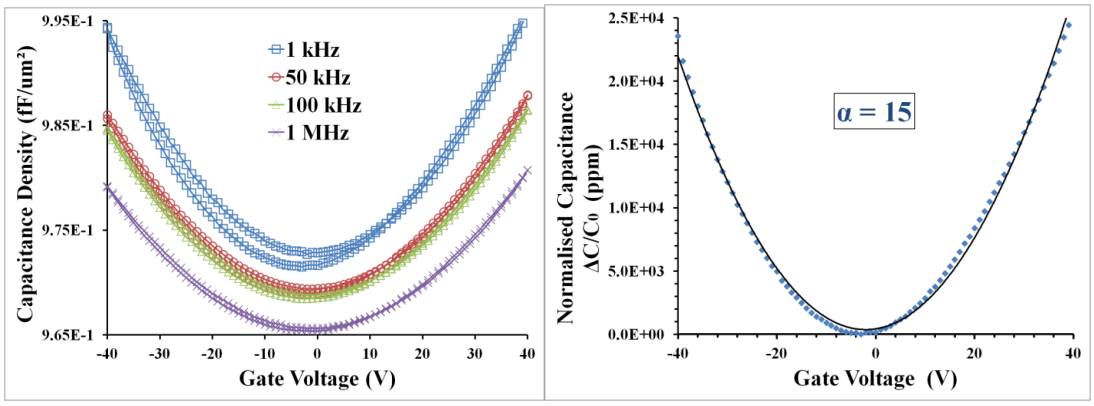

Figure 2.2 CD-VG double sweeps at multiple frequencies (left), Quadratic voltage coefficient of capacitance extracted from polynomial fit to normalised capacitance at 1 kHz (right).

Leakage current in Figure 2.3 (top) is of the order of 10^{-8}A/cm^2 or less up to ~ 40V while the shape of the IV trace is reasonably symmetric for both polarities and the electric field breakdown strength (E_{BD}) ~ 8.1 MV/cm. The E_{BD} value is in agreement with published results [139] for an amorphous $HfSiO_x$ with a ratio of hafnium to silicon of 4:1. Also, it is evident in Figure 2.3 (bottom) that this work was generally

consistent with the empirical dependence of E_{BD} on dielectric constant ($E_{BD} \sim k^{-0.5}$) [27].

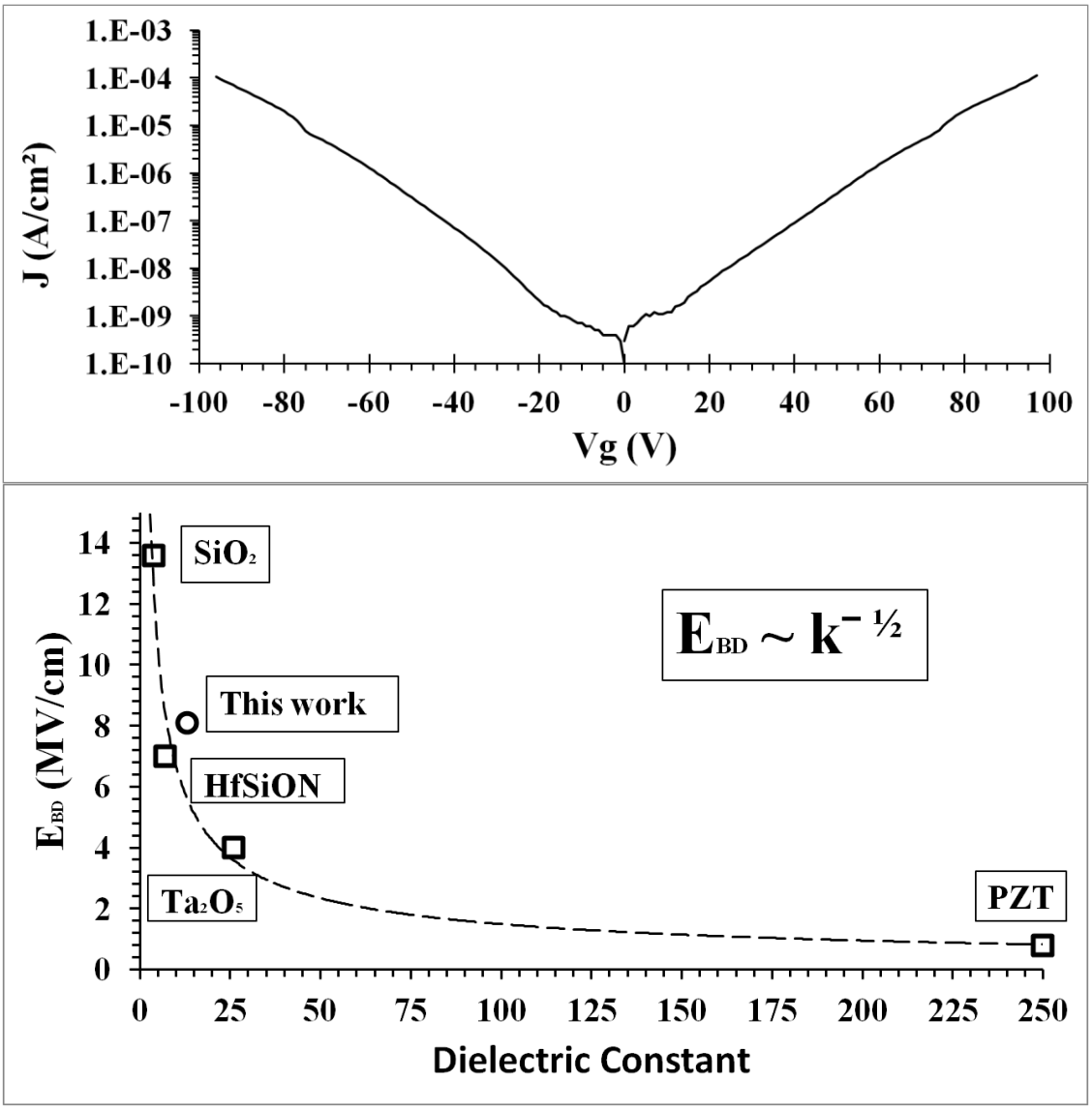

Figure 2.3 J-V traces (top) and E_{BD}-dielectric constant for this work and previously published work (bottom), the previously published work was found to have ~ $k^{-0.5}$ dependence [27].

2.3.1 Reliability Characterisation and Analysis

The intrinsic reliability characteristics of this $HfSiO_x$ film were investigated according to the TDDB technique where CVS measurements were taken with a positive bias on the gate electrode (resulting in bottom electron injection) until hard breakdown occurred which was defined to be a five or more orders of magnitude increase in leakage current. These measurements were repeated multiple times at each voltage (89V, 85V, 80V and 76.5V) to build a statistically relevant population across four orders of magnitude in time (10^1 - 10^4 s). I-t traces for all CVS measurements can be observed in 4. The leakage current trace under CVS decreases with time which may be attributed to electron trapping in the bulk oxide[146], which is also clearly visible to a greater extent in several of the traces. However, as the CVS progresses the rate of decline in leakage current moderates and this may be due to stress induced defects such as neutral traps which result in a stress induced leakage current (SILK) component [147].

Constant voltage stress was observed to effect on the value of α especially during the initial 100 second time period where it was reduced by almost 30%. Thereafter, this reduction moderated considerably, although, a small decrease with time was still evident. This effect could possibly be attributed to the polarizability of defects such as vacancies in the oxide that are quickly filled with trapped electrons at high electric fields as was indicated in the CVS I-t traces above.

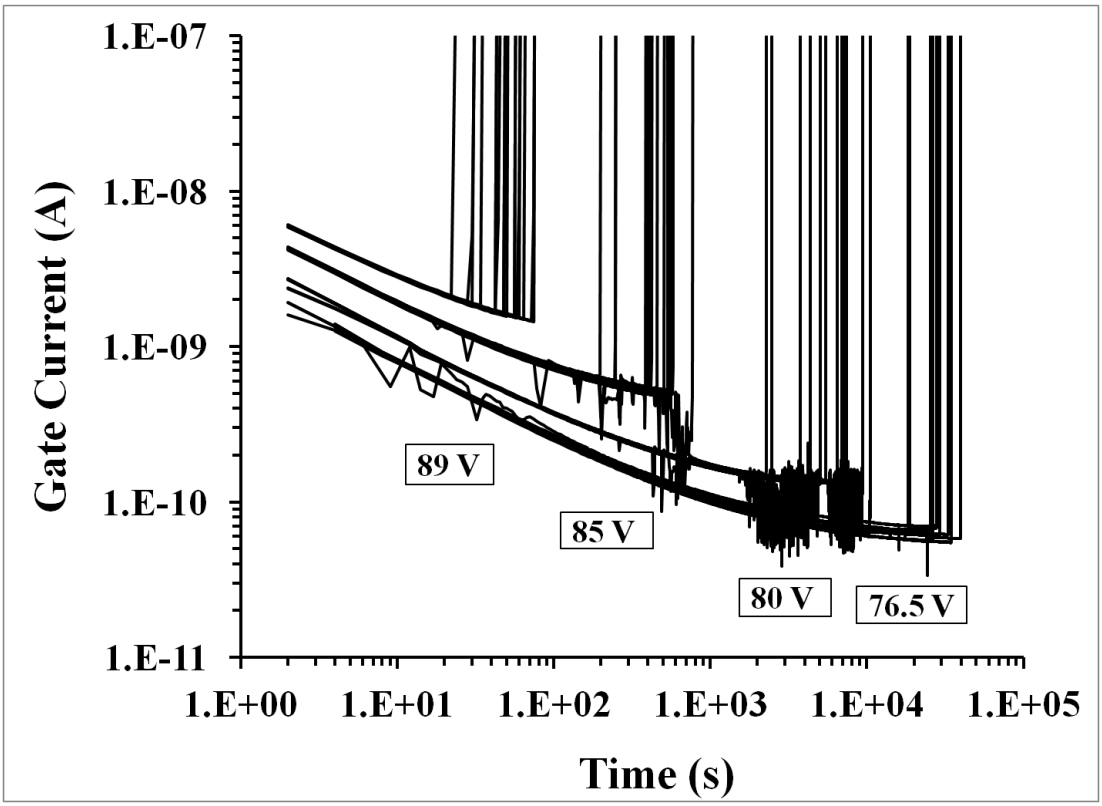

Figure 2.4 I-t traces for CVS measurements at 89, 85, 80 and 76.5 V. All measurements were performed with a positive CVS on the gate.

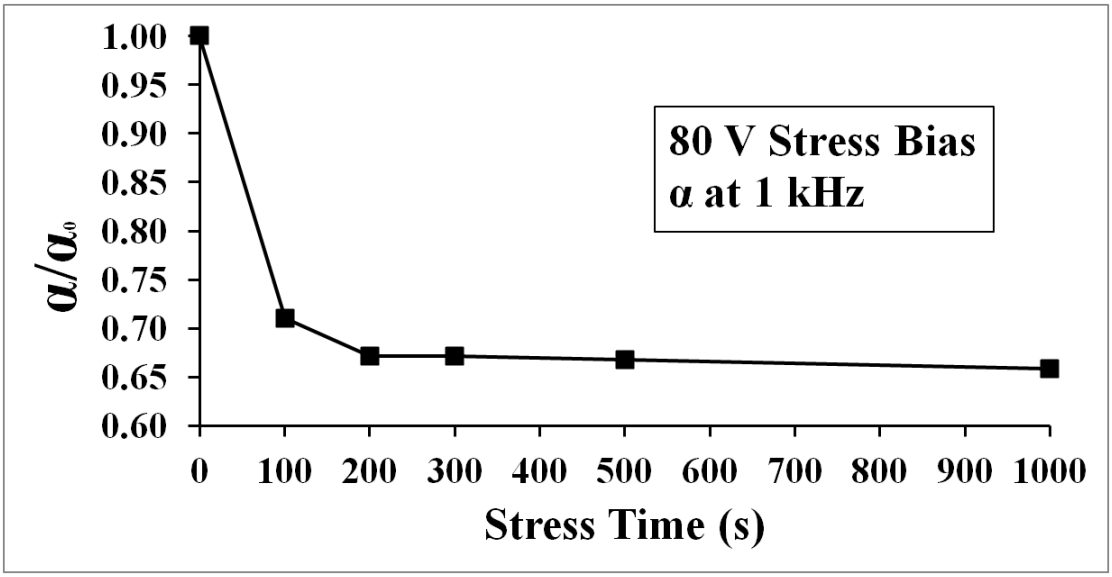

Figure 2.5 Quadratic voltage coefficient of capacitance (α at 1 kHz) variation as a function of stress time under a constant stress bias of 80 V, positive bias on the gate.

Over sixty measurements in total were taken for the four distributions to provide a reasonable level of accuracy of the Weibull parameters. These Weibull distributions of the time to breakdown (t_{BD}) at multiple voltages are shown in Figure 2.6 and the Weibull slope or shape parameter (β) was determined by maximum likelihood algorithm fitting ~ 3.4, in addition, the t_{BD} was determined at 63% cumulative failure (n_{63}) for each CVS Weibull distribution. The β value measures the tightness of the distribution and a larger value increases confidence in the merit of the extrapolated 10 year, area and low percentile scaled value. Also, the larger the value the less scaling required due to the role of β in the calculation of this value. β in this case is lower than would be expected for SiO_2, β ~ 9 for 10 nm film and increases with film thickness [148]. However, the β value of some material's such as ZrO_2 and Al_2O_3 have has been shown to be independent of film thickness [149] and it is suggested that this hafnium silicate materials' β value may be independent of or loosely correlated with film thickness. Since β ~ 2 has been observed for 4 nm thick amorphous $HfSiO_x$ (Hf:Si 4:1) in MIM (TiN electrodes) capacitor structures [139] and this is similar to our value β ~ 3.4 for $HfSiO_x$ ~ 120 nm.

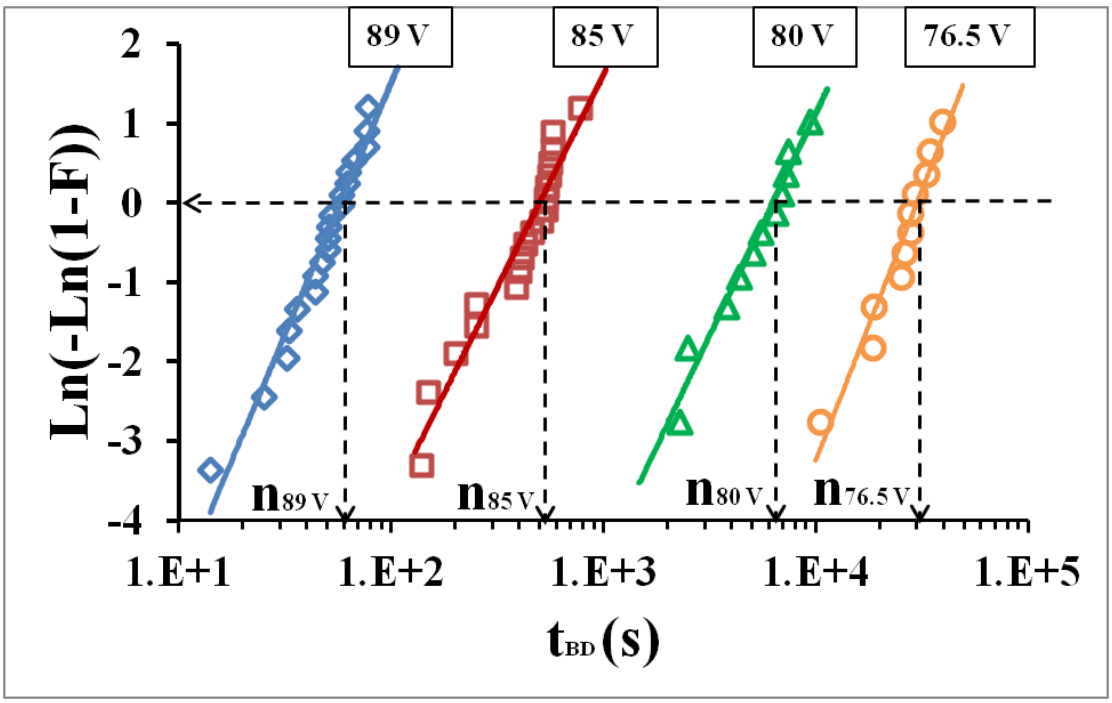

Figure 2.6 Weibull distributions of hard breakdown measured at room temperature for positive bias CVS on the top electrode at the labelled voltages. The average value of the β shape parameter is 3.4 and the n values at 63% cumulative failure are indicated for each voltage

The linear E-model was utilised for the TDDB analysis since it is the most conservative of the field acceleration models and it is based on many decades of research on SiO_2 breakdown behaviour. According to the linear E-model the time to breakdown is related to the electric field as follows

$$t_{BD} = t_0 exp(-\gamma E) \qquad (2)$$

the parameter t_0 is the y intercept, γ is the voltage acceleration factor and E is the electric field. It is based on the assumption that the dielectric breakdown is a thermodynamic process and the electric field interacts with the weak silicon-silicon

bonds that arise from oxygen vacancies. The applied electric field eventually breaks the bond and creates a permanent defect [66], [67], [150]. This leads to a silicon atom with a localised unpaired electron that's also bonded to three oxygen atoms [69] and eventually results in the creation of a conductive path between the electrodes. The maximum operating voltage to give a MTTF at 10 years was found to be 58 V from the n_{63} data in Figure 2.7 (top). The field acceleration factor was shown to be 6.0 (cm/MV) from a linear fit of this data as shown in Figure 2.7 (top inset). This value was compared to other published values which were deemed to be correlated [27]. It was considered to be approximately 2.8 cm/MV smaller than the ideal value that the trend would suggest for a dielectric constant of 13.2.

The above values suggest a reliable dielectric that has an operational voltage with a lifetime of 10 years well above required limits (~ 30% to 40% of E_{BD}), however, this lifetime is for a 63% cumulative failure point in the distribution which is not practical for electronic devices.

This maximum operating voltage value has not been area scaled (assuming Poisson's area scaling). The lifetime at specification conditions can be determined by the following methodology. Firstly, the n_{63} values are determined by extrapolating the gate voltage to the operational range of interest ((30, 35 and 40) V 30% to 40% of E_{BD} for analogue device operation) using an exponential model as in Figure 2.7. Then these values are area scaled to specification area of 0.1 cm^2 [151] followed by further scaling to low failure percentiles of 0.01%. The scaling equations for voltage, area and failure percentiles, (3), (4) and (5) respectively are specified below.

$$n_2 = t_0 exp(c v_2) \quad (3)$$

$$n_2 = n_1 \left(\frac{A_1}{A_2}\right)^{1/\beta} \quad (4)$$

$$\ln[-\ln(1-F)] = \beta \ln t - \beta \ln n \quad (5)$$

where n_2 is the scaled or extrapolated lifetime, c is a constant, v_2 is the voltage chosen to calculate the lifetime, n_1 is 63% cumulative failure lifetime, A_1 and A_2 are the measured device area and approximate chip area respectively, F is the cumulative failure, t is the time and n is the lifetime.

The maximum operating voltage to for 10 years operation at 0.1 cm^2 and 0.01% failure has been scaled according to the aforementioned methodology and was determined at 49V as shown in Figure 2.8. The scaled and extrapolated values are reasonably close to the initial values due to the size of β. This 49 V well exceeds the operation range of analogue applications for this film thickness.

The Weibull distribution β shape parameter for TDDB measurements of SiO_2 capacitors has been shown to vary with film thickness, however, there was negligible or weak observed variance with temperature 303 k – 473 k [64]. However, β was observed to be strongly temperature dependent for the amorphous hafnium silicate dielectric in this study as shown in Figure 2.9 (right) and this dependence was best described by a second order polynomial fit for the temperature range 294 k – 398 k.

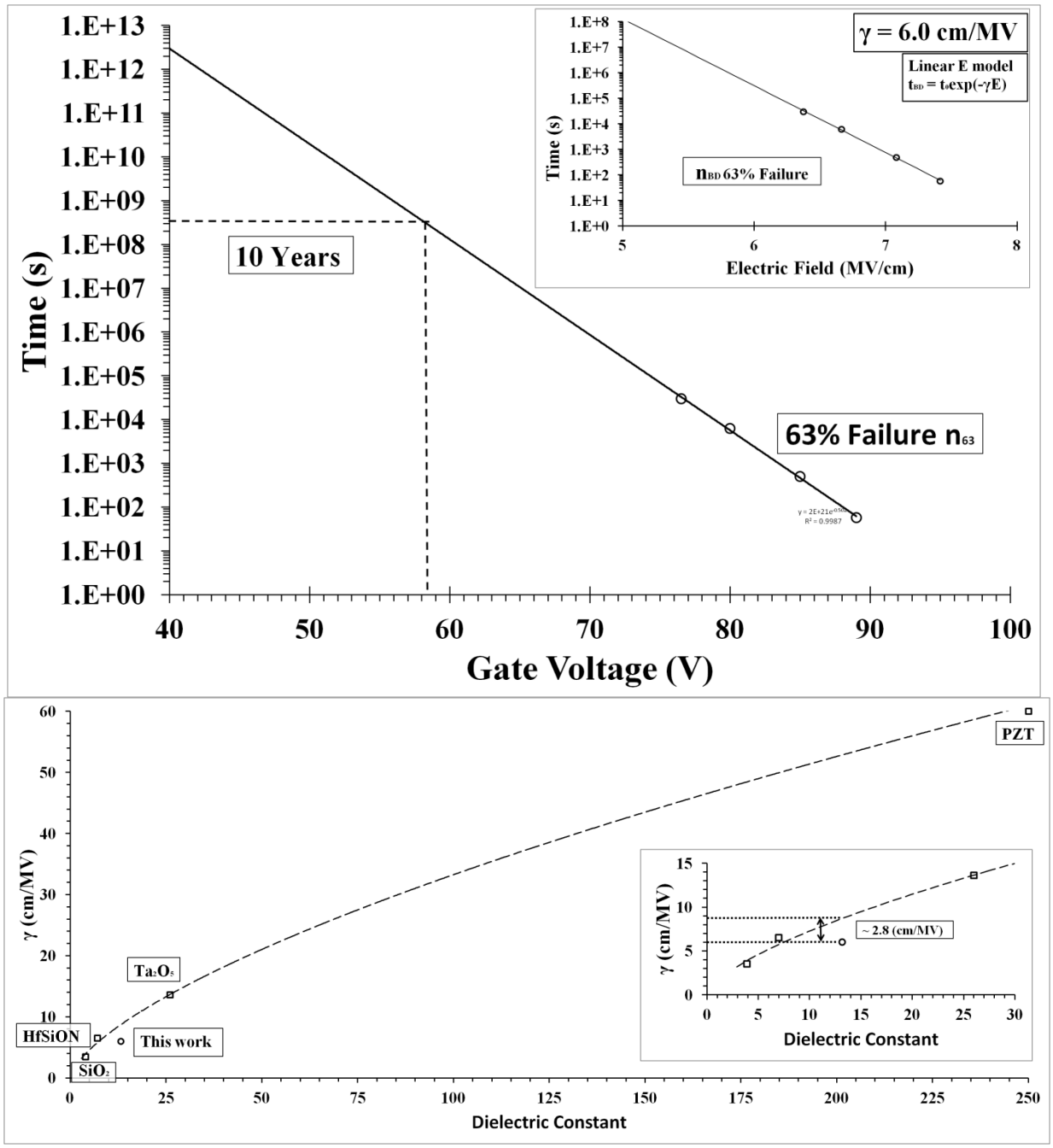

Figure 2.7 Median time to failure for n63 with extrapolation to maximum operating voltage at 10 years lifetime (top) and determination of the associated field acceleration parameter γ (inset).

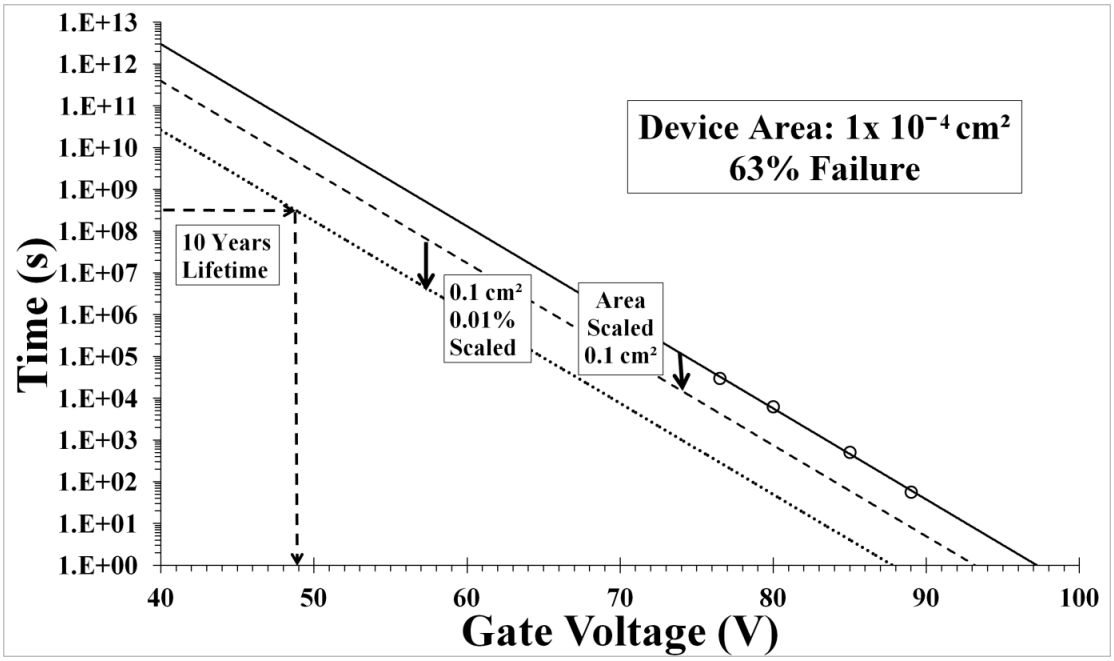

Figure 2.8 TDDB extrapolation fit after scaling to 0.1 cm2 and 0.01% failure, for this sample a gate voltage of 49 V is extrapolated to a lifetime value of 10 years.

A temperature dependent β has been observed previously for ZrO_2 MIM capacitors [152] and these results have been re-plotted in Figure 2.9 (top) to determine the fit that best describes the data, which is also a second order polynomial fit. The increase in β with increasing temperature has been attributed to temperature sensitive defects that may become mobile with additional thermal energy [152] and this thermally activated redistribution of defects becomes an increasingly dominant cause of failure, hence, narrows the failure distribution spread leading to an increase in β. Oxygen vacancies are thought to be the major source of electrically active defects in both studies, however, the effect was much more pronounced for the material system in this study and this may indicate that the energy barrier to vacancy migration is lower in this hafnium silicate material than the ZrO_2 dielectric in the other work.

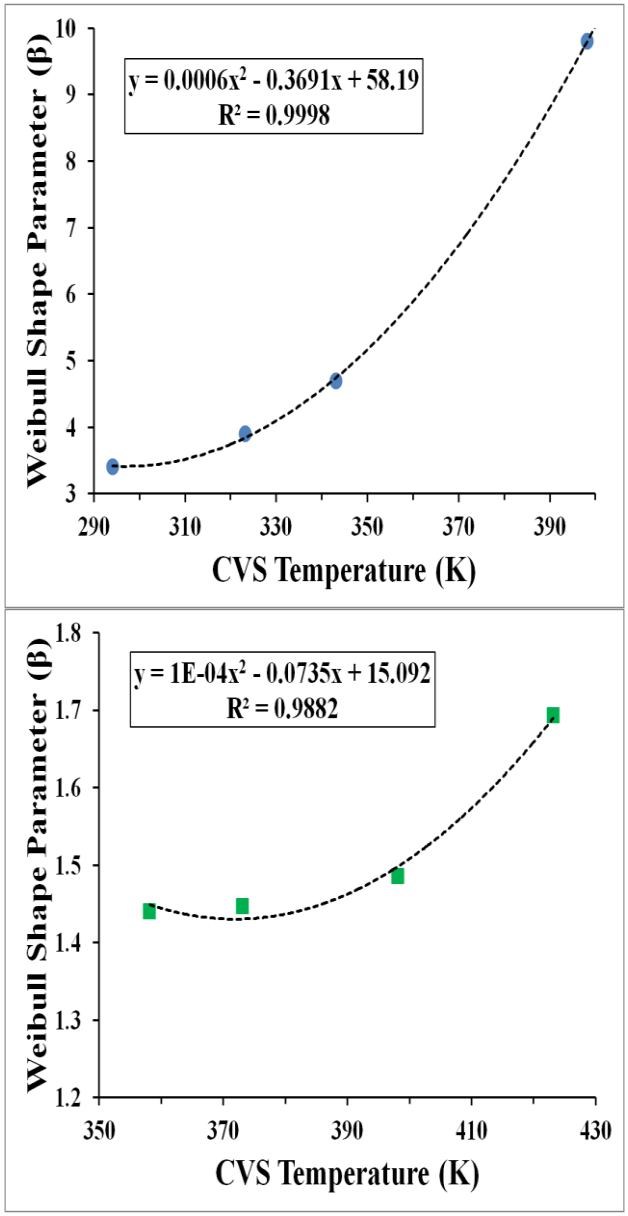

Figure 2.9 Weibull distribution β shape parameter for hard breakdown of the MIM capacitors (55 in total for 4 distributions) in this study for various temperatures 294 K – 398 K (top) and β values for Weibull distribution data from a published study on ZrO2 ~ 8 nm MIM capacitors with TiN electrodes for various temperatures 358 K – 423 k [152].

According to the Thermochemical model the local electric field (E_{Loc}), described by the Lorentz relation

$$E_{Loc} = \left(\frac{2+k}{3}\right) E \qquad (6)$$

The local electric field distorts the bonds and reduces the enthalpy of activation (with E = 0) for bond breakage (ΔH_0^*) of polar molecules. This effect increases with k value. The weakened bonds are more susceptible to breaking and this may result in the generation of neutral traps which may eventually lead to a conductive path (percolation theory) and then electrical breakdown of the dielectric [25]. The activation energy (ΔH) required to break a bond is related to E as follows [153]

$$\Delta H = \Delta H_0^* - P_0 \left(\frac{2+k}{3}\right) E \qquad (7)$$

where ΔH_0^* is the activation energy required for bond breakage in the absence of E and the active molecular dipole moment is P_0. For dielectric breakdown ΔH → 0 as enough bonds are broken to form a permanent conductive path and this occurs at E_{BD}, hence

$$E_{BD} = \frac{\Delta H_0^*}{a} \qquad (8)$$

where the effective dipole moment for bond breakage $a = P_0(2 + k)/3$. The Weibull distribution of t_{BD} can be related to E and ΔH_0^* as follows [154]

$$\ln(t_{BD}) = \frac{\Delta H_0^*}{k_B T} - \gamma E \qquad (9)$$

$$\gamma = \frac{P_0\left({}^{2+k}/_{3}\right)}{k_B T} \qquad (10)$$

and from (7) and (9) it follows

$$\gamma E_{BD} = \frac{\Delta H_0^*}{k_B T} \quad (11)$$

Also by simple substitution

$$\gamma = \frac{a}{k_B T} \quad (12)$$

The extracted activation energy of bond breakage ΔH_0^* value calculated from (11) was ~ 1.3eV and a ~ 15.2 eÅ was also determined from (12). The activation energy is quite low when compared to SiO_2 ~ 2 eV, attributed to an Si-O bond [153] or an Si-H bond [155]. However, a value of ~1 eV is also found in the literature [67] and it is thought to be attributed to an oxygen vacancy [66]. Therefore, the 1.3 eV could possibly be attributed to an oxygen vacancy, although, the effective dipole moment of bond breakage a ~ 15.2 eÅ would suggest not, as it is much larger than the oxygen vacancy value a ~ 7 eÅ. Also, the electronegativity is considerably lower for Hf ~ 1.3 compared to the value for Si ~ 1.8 [156] and this results in the Hf-O bond being more polar as there is around ~ 90% electron transfer from the Hf to O [156] whereas it is ~ 90% for O to Si [66] which along with the differences in electric susceptibility would lead to the effective dipole moment for bond breakage approximating a multiple of 1.96 times that of SiO_2 [156]. The values for SiO_2 range between 7.4-13 eÅ [66] and, therefore, Hf-O values could range from 14.5-25.5 eÅ which compares well with our calculated value. The difference in electronegativity coupled with the longer bond length of Hf-O ~2.17 Å [157] compared to Si-O ~ 1.62 Å [158] would indicate a substantially lower bond strength for Hf-O which may account for the

extracted activation energy of bond breakage ΔH_0^* ~ 1.3 eV which is in good agreement with a published value of ΔH_0^* ~ 1.26 eV [159]. This hafnium silicate obviously has a mix of both Hf-O and Si-O bond types; however, this analysis suggests that the Hf-O bonds play a major role in time dependent dielectric breakdown mechanism.

Four CVS measurements were taken at an I_G of 76 V, however, the t_{BD} was beyond the time out of the measurement, however, this data is noteworthy due to the response of leakage current at this lower CVS value as shown in Figure 2.10 (top). There appears to be a considerable increase in t_{BD} between 76.5 V and 76 V which may point to the application of a power law for the lifetime extrapolation. The power law model has been verified for ultra-thin high-*k* gate oxides [64], however, more data at lower E_{BD} would be required to confirm this hypothesis. The I_G values are shown to oscillate after pronged stress in Figure 2.10 (top) and this is indicative of a large amount of electron trapping [160]. This mechanism was also observed for four data sets (out of total data set of 61) between 85 V, 80 V and 76.5 V, although, less electron trapping was observed for a considerably shorter portion of the measurement time and this was followed quite quickly by hard breakdown as shown in the representative data in Figure 2.10 (bottom). Whereas, at 76 V CVS the electron trapping reduces the leakage current over several orders of magnitude in Figure 2.10 (top) and was evident for almost the duration of the measurement. Hard breakdown was not observed to follow the electron trapping behaviour as the measurements

timed out. This data led on to further investigation in to the leakage mechanisms responsible for conduction in this sample as discussed below.

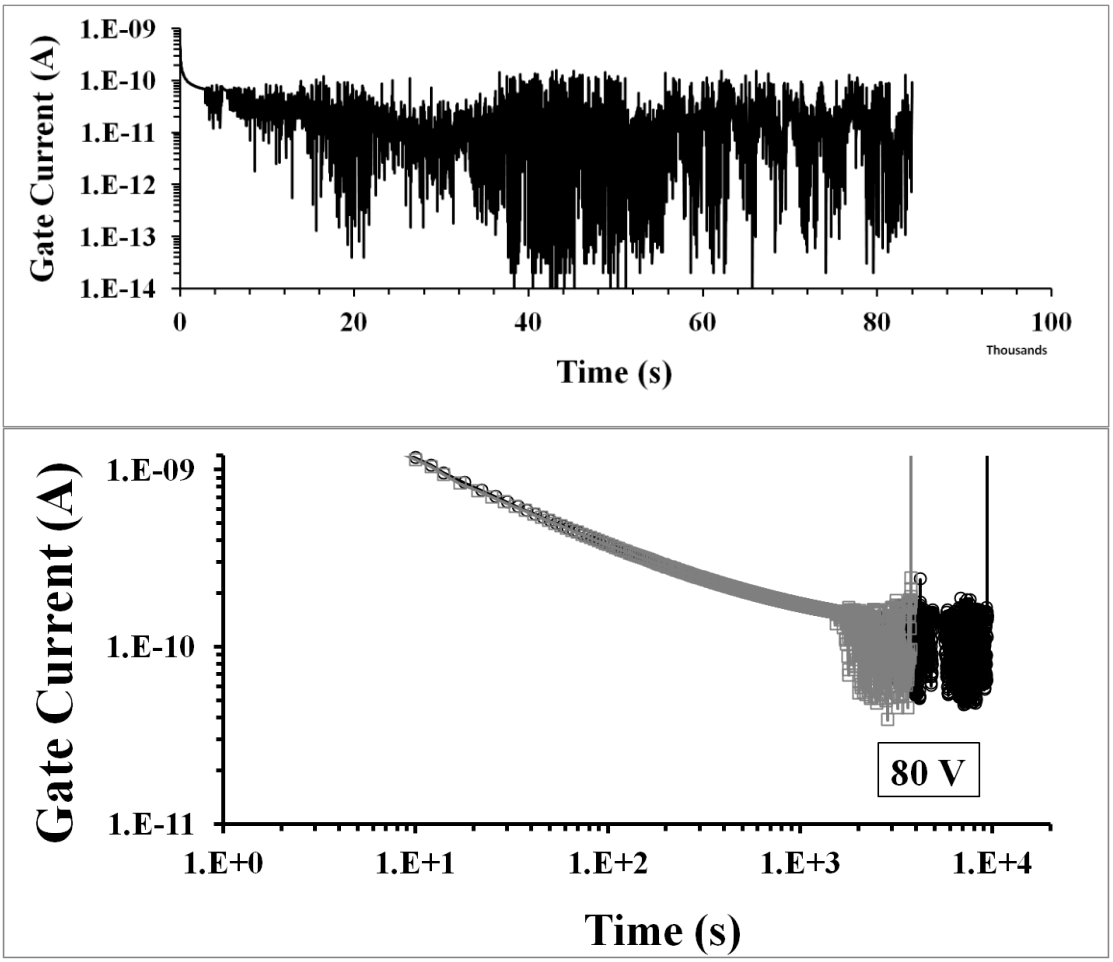

Figure 2.10 I-t trace of CVS at 76 V (84 (ks) timeout), electron trapping is evident after approximately 3000 seconds stress time (top). I-t traces of CVS at 80 V with some electron trapping evident (bottom).

2.3.2 Characterisation and Analysis of Conduction Mechanism

Multiple IV sweeps in both polarities were performed over a range of temperatures from 21ºC to 125ºC to investigate the origin of the leakage current conduction

mechanism. The leakage current in the J-V traces in Figure 2.11 are observed to increase with temperature, however, considerably more dispersion is evident in the positive bias compared to the negative, as is indicated between the arrows.

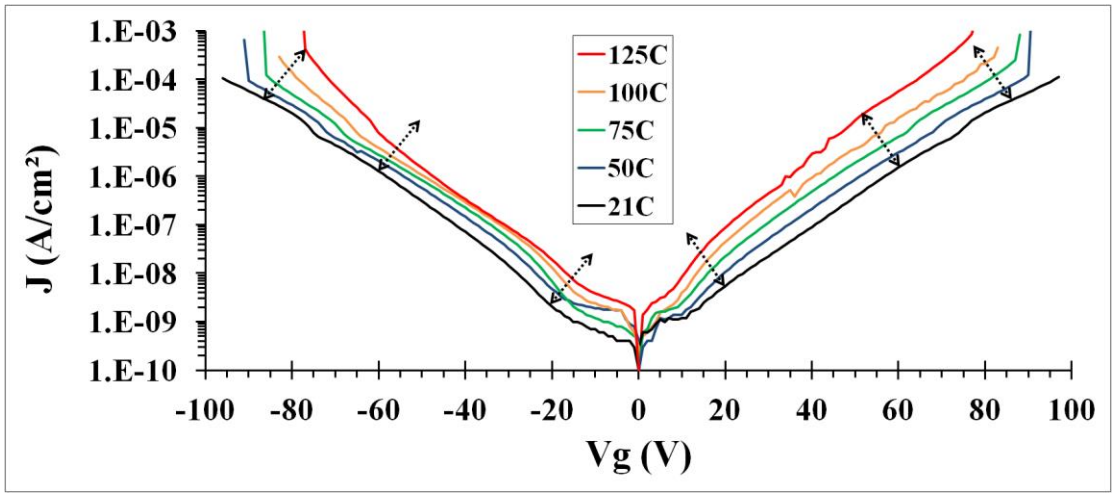

Figure 2.11 I-V traces for positive and negative biases on the gate at multiple temperatures as indicated.

The data in Figure 2.11 was plotted with the absolute value of the negative bias sweeps to directly compare with the positive bias sweeps for clarity in Figure 2.12. The increase in dispersion in the leakage current I-V traces with temperature is evident in Figure 2.12 (top), between at 21˚C were it is almost nonexistent compared to 125˚C where there is approximately an order of magnitude difference for most of the sweep. The progression of the dispersion with increasing temperature can be observed over the intermediate values, 50˚C, 75˚C, 100˚C in Figure 2.12 (bottom A, B, C respectfully). This data would seem to indicate that the conduction mechanisms differ with increasing temperature above 21˚C depending on the gate bias.

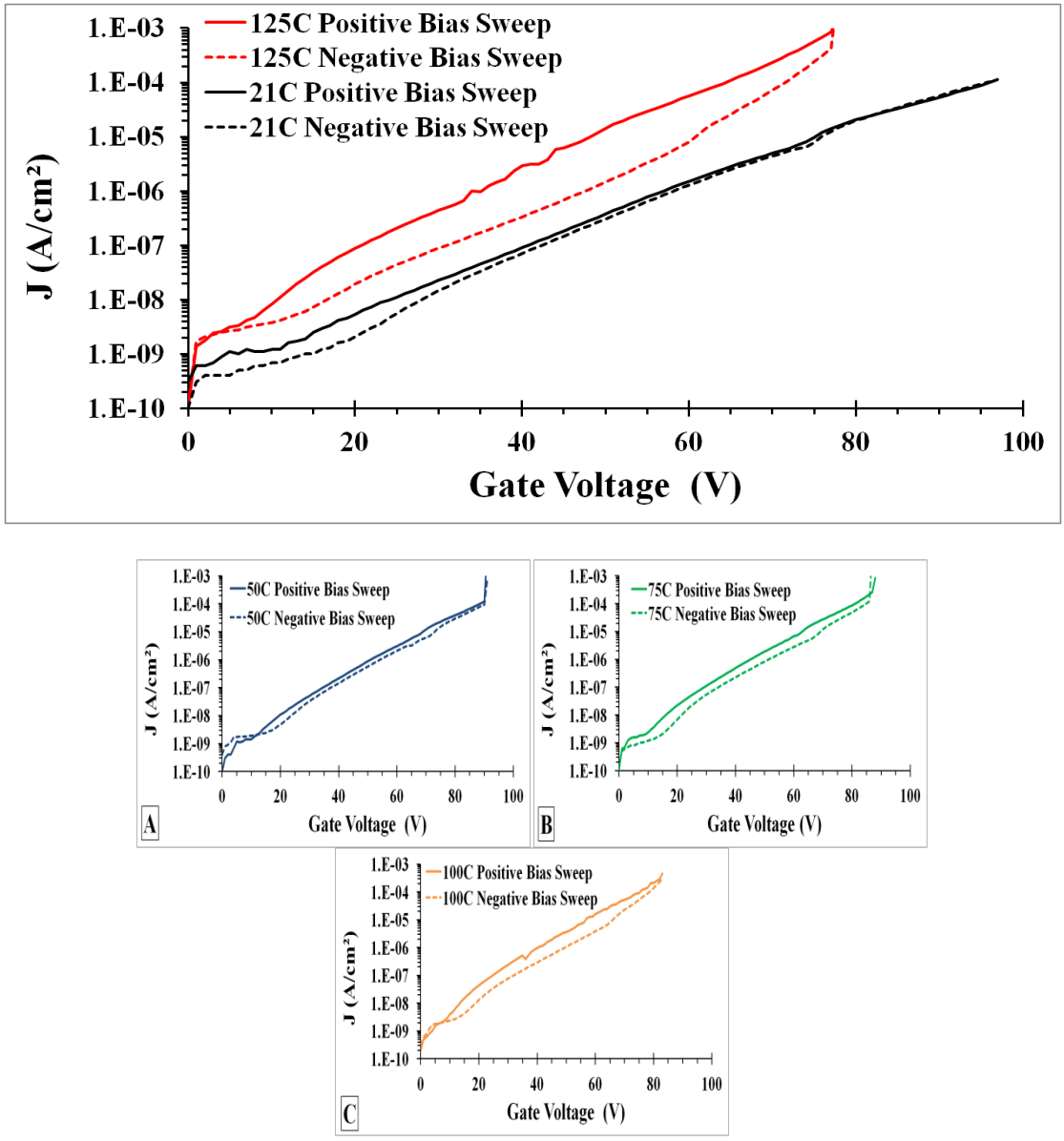

Figure 2.12 Positive (solid line) and negative (broken line) bias sweeps for IV data at 125˚C and 21˚C (top) and 50˚C (bottom A), 75˚C (bottom B) and 100˚C (bottom C).

Schottky and Poole-Frenkel conduction mechanisms have been frequently observed as the dominant leakage current mechanism at high electric field in many high-k metal oxides capacitor systems.

Thermionic Emission is the emission of a carrier over the dielectric barrier into the conduction band of the dielectric. It is called Schottky emission when it happens in the presence of an electric field that effectively lowers that barrier to the conduction band of the dielectric due to the image charge theorem.

Poole-Frenkel has been observed as the dominant conduction mechanism in dielectrics with a large trap density where tunnelling conduction mechanisms have been disregarded due to the thickness of the dielectric. The traps hamper the transport of electrons in the conduction band of the dielectric by trapping and de-trapping them and hence moderating the current.

Schottky emission is described as follows

$$J_{SE} = AT^2 exp\left(\frac{-q\left(\phi_B - \sqrt{qE/4\pi\varepsilon_0\varepsilon_r}\right)}{k_B T}\right) \qquad (13)$$

where J_{SE} is the Schottky current density, A is the effective Richardson coefficient, q is the elementary charge, ϕ_B is the Schottky barrier height, E is the electric field, ε_0 is the vacuum permittivity and ε_r is the dynamic dielectric constant.

The equation (13) above can be linearised as follows

$$\ln\left({J_{SE}}/{T^2}\right) = \frac{\sqrt{q/4\pi\varepsilon_0\varepsilon_r}}{k_B T}\sqrt{E} - \frac{q\phi_B}{k_B T} + \ln(A) \quad (14)$$

and the slope (m) and y intercept (y_0) are

$$m = \frac{\sqrt{q/4\pi\varepsilon_0\varepsilon_r}}{k_B T} \qquad (15) \qquad y_0 = -\frac{q\phi_B}{k_B T} + \ln(A) \qquad (16)$$

The I-V data for multiple temperatures was plotted according to a (14) for the positive bias sweep in Figure 2.13 (top) and for the absolute values of the negative bias sweep in Figure 2.14 (top).The high field (≥ 2.25 MV/cm) region of both plots was fitted in a linear fashion and the R^2 values demonstrated very good fits for the positive bias in Figure 2.13 (bottom) and good fits for the negative bias data up to 75˚C after which some deterioration was evident in Figure 2.14 (bottom). The Schottky barrier height and the dynamic dielectric constant / refractive index ($n = \sqrt{\varepsilon_r}$) were calculated from the acquired slopes (15) and y intercepts (16) for each data set (21˚C - 125˚C), ϕ_B ~ 0.38 (negative bias on the gate), ϕ_B ~ 0.29 eV (positive bias on the gate), ε_r ~ 4.1 – 1.9 (at optical frequencies, hence, lower than values extracted from CV's) and n ~ 2 – 1.4. The ε_r (n) values were similar for positive and negative bias sweeps.

Poole-Frenkel emission is described as follows

$$J_{PF} = CEexp\left(\frac{-q(\phi_t - \sqrt{qE/\pi\varepsilon_0\varepsilon_r})}{\xi k_B T}\right) \qquad (17)$$

where J_{PF} is the Poole Frenkel current density, C is the pre-exponential factor, ξ is a factor that depends on acceptor compensation which is commonly set to 1 [30]–[32] and ϕ_t is the trap energy level below the conduction band.

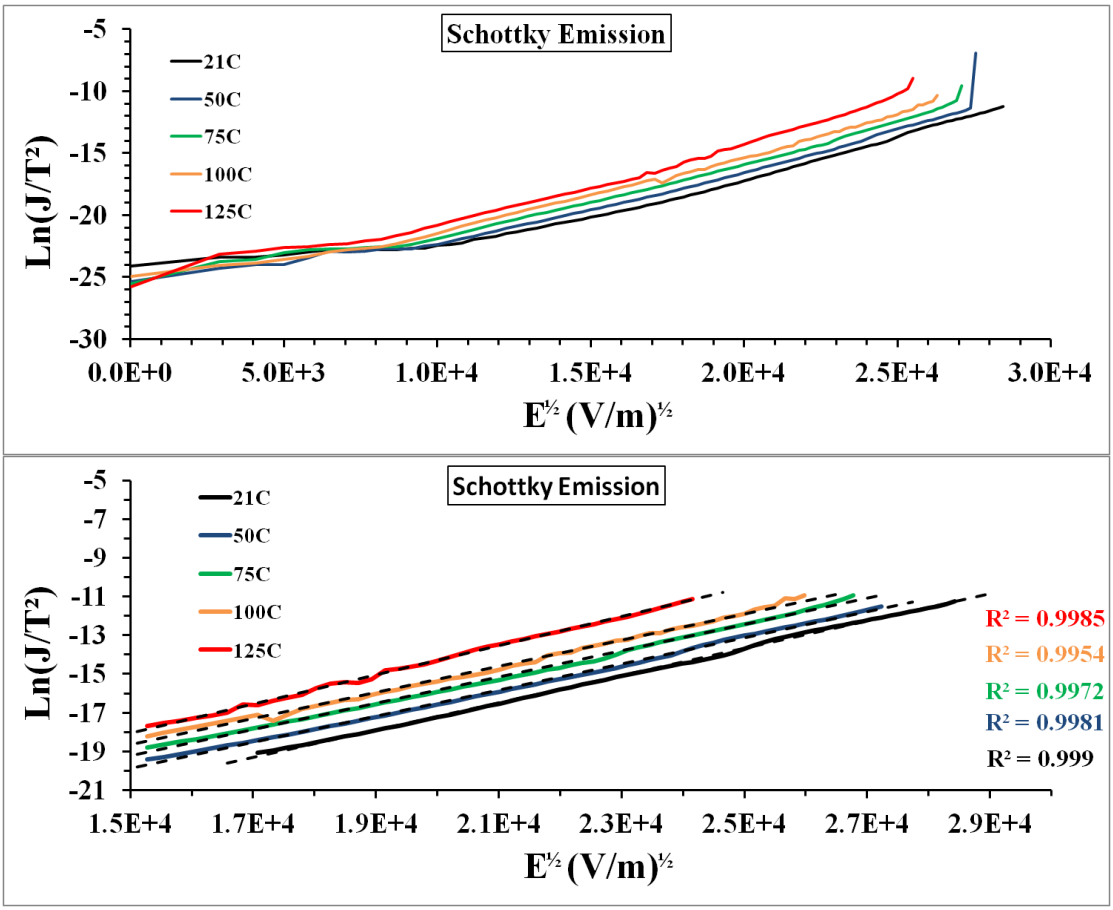

Figure 2.13 High field I-V data from positive bias sweeps at multiple temperatures fitted with the Schottky emission conduction model (top) and linear fits to each temperature at high field with associated R2 values (bottom).

The equation (17) can be linearised and plotted $\ln(J_{PF}/E)$ versus $\sqrt{E}$ were the slope (m) and y intercept (y_0) are

$$m = \frac{\sqrt{q^3/\pi\varepsilon_0\varepsilon_r}}{\xi k_B T} \qquad (18) \qquad y_0 = -\frac{q\phi_t}{\xi k_B T} + \ln(C) \qquad (19)$$

A similar analysis to the Schottky emission above of the multiple temperature IV data was performed for a linearised version of the Poole-Frenkel emission equation for

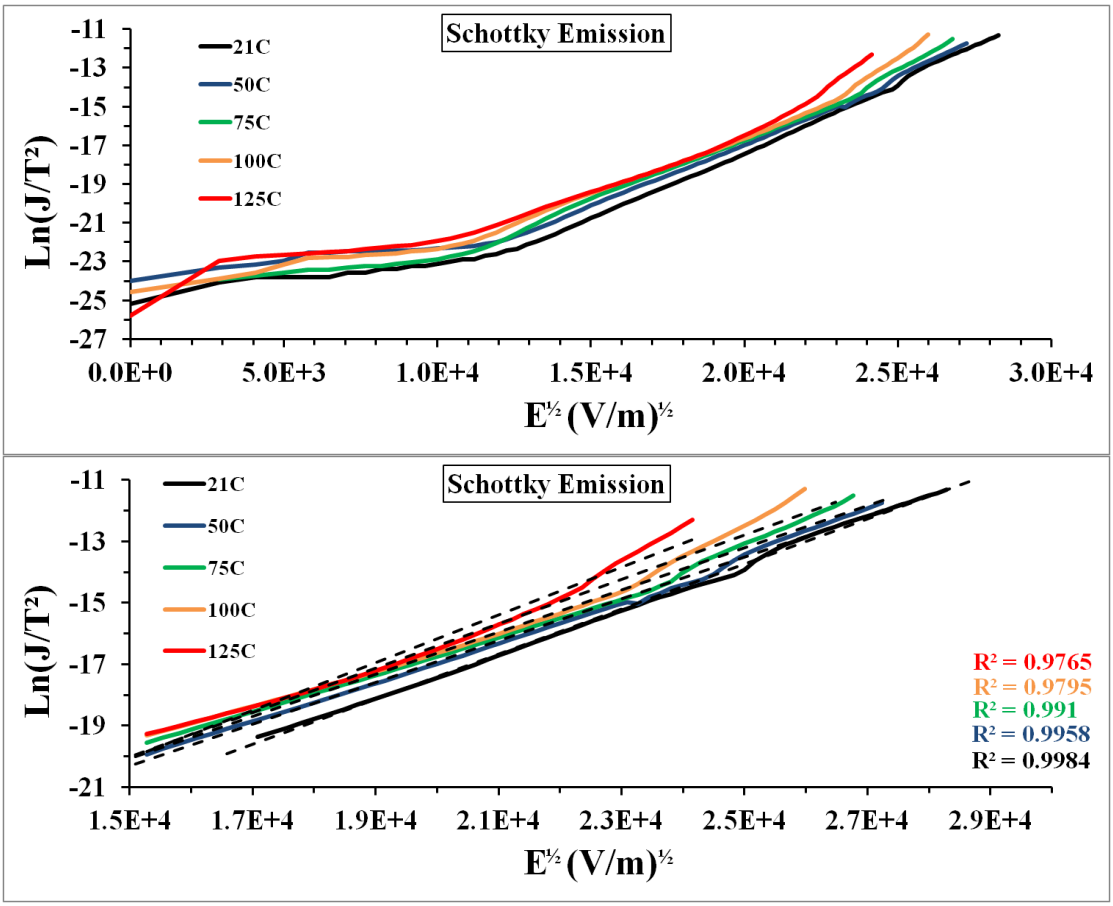

Figure 2.14 High field I-V data from negative bias sweeps at multiple temperatures fitted with the Schottky emission conduction model (top) and linear fits to each temperature at high field with associated R2 values (bottom).

positive bias data in Figure 2.15 and negative bias in Figure 2.16. The R^2 values were very good for the positive bias and good for the negative bias up to 50˚C, however, then the R^2 values deteriorated with increasing temperature similarly to the Schottky emission fits. Also, an overlap is apparent ~ 15,000 - 20,000 $\sqrt{E}$ $(V/m)^{-1/2}$ for the 100˚C and 125˚C traces in Figure 2.16 (top), this saturation of current with temperature would imply that the trap barrier has been reduced to zero in this regime.

Again, as with the Schottky analysis several parameter were calculated from the slopes (18) and y intercepts (19), (21˚C - 125˚C), ϕ_t ~ 0.35 (negative bias on the gate), ϕ_t ~ 0.29 eV (positive bias on the gate) below the $HfSiO_x$ conduction band, ε_r ~ 5.1 – 3.4 and n ~ 2.3 – 1.8, there was little variance between ε_r (n) values for the positive and negative biases. The mean value for the refractive index was ~ 2.1 ± 0.2 which would indicate a low Si content in the hafnium silicate and as mention earlier the E_{BD} ~ 8.1 agrees well with a value in the literature that has a 20% Si content.

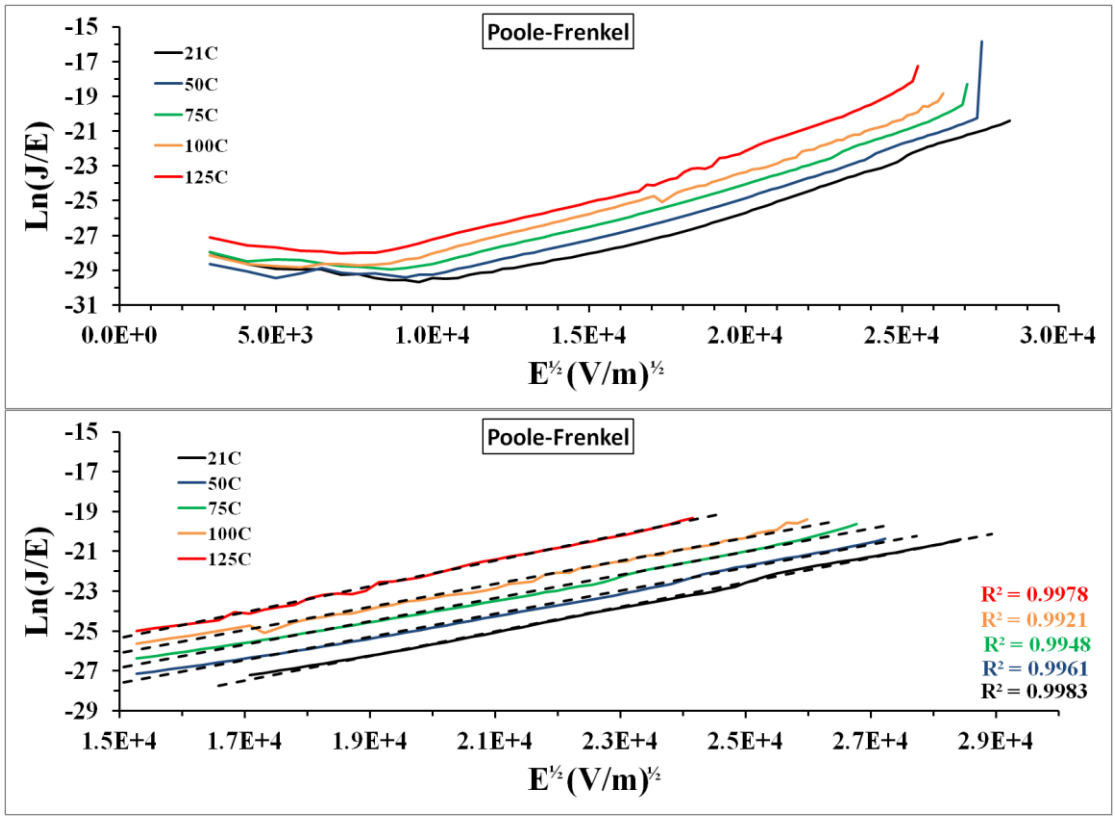

Figure 2.15 High field I-V data from positive bias I-V sweeps at multiple temperatures fitted with the Poole-Frenkel conduction model (top) and linear fits to each temperature at high field with associated R2 values (bottom).

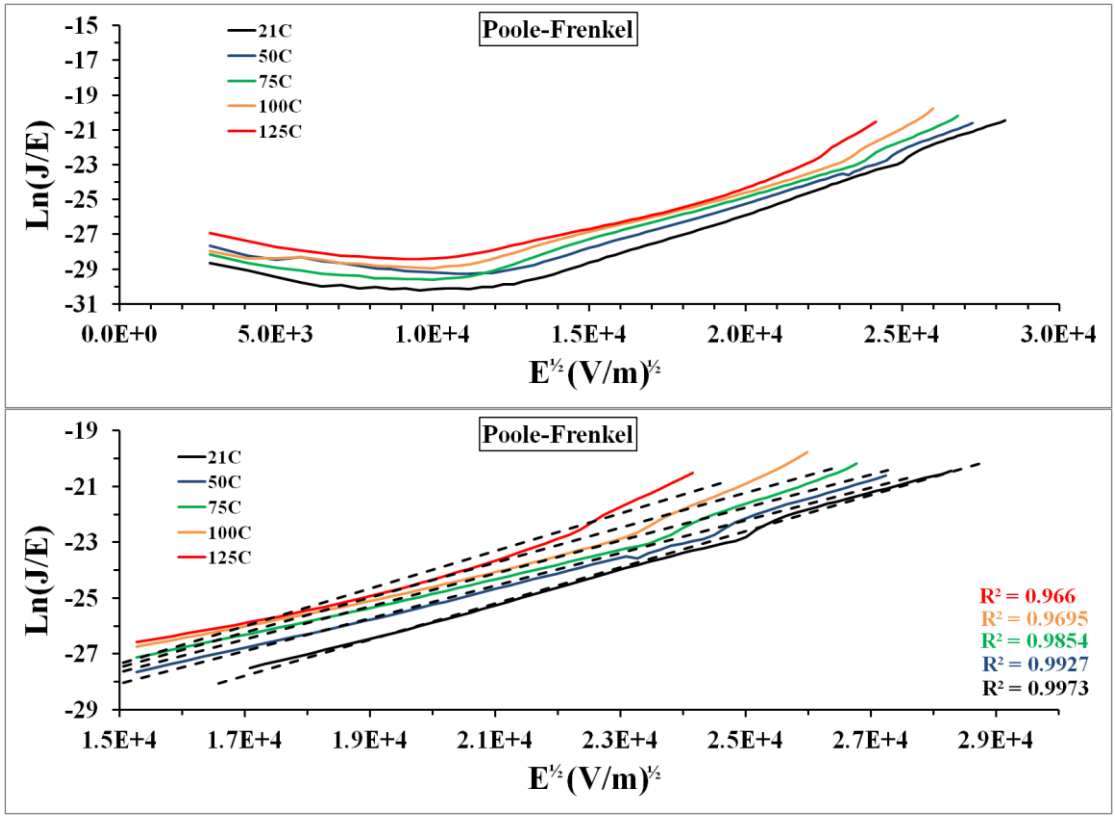

Figure 2.16 High field I-V data from negative I-V bias sweeps at multiple temperatures fitted with the Poole-Frenkel conduction model (top) and linear fits to each temperature at high field with associated R2 values (bottom).

It has not been possible thus far to differentiate between Schottky and Poole-Frenkel emission as the dominant conduction mechanism in our sample. Therefore, additional analysis is required to further understand the conduction mechanism. Many temperature dependent leakage mechanisms follow an Arrhenius type relationship between leakage current density and temperature. This allows for the extraction of the

energy barrier to conduction and may permit identification of the dominant conduction mechanism.

The linearised version of the Poole-Frenkel emission was plotted as $\ln(J_{PF}/E)$ versus $1/T$ which predicts Arrhenius behaviour [30], [161] and the slope which is proportional to the reduced trap barrier, which reduces with increasing electric field, is as follows

$$m = \frac{q\phi_t - \sqrt{q/\pi\varepsilon_0\varepsilon_r}\sqrt{E}}{\xi k_B} \qquad (20)$$

The equation (20) above may be plotted as m versus $\sqrt{E}$ for a number of electric field values in the positive and negative biases and ϕ_t can be determined from the y intercept at $\sqrt{E} = 0$ as shown below.

$$y_0 = \frac{q\phi_t}{\xi k_B} \qquad (21)$$

The leakage current for different stress voltages from the I-V data in the temperature range 21˚C - 100˚C was plotted in Figure 2.17 (top) for the positive bias and Figure 2.17 (bottom) for the negative bias in the temperature range 21˚C - 125˚C according to the above Arrhenius relationship. The temperature and voltage ranges are different for each bias since this provided a best fit for the data.

The slopes from the Arrhenius plot (positive I-V sweeps) for various voltages (30-75 V) were plotted in Figure 2.18 (top) to verify the suitability of Poole-Frenkel emission as the dominant leakage current mechanism in the positive bias and to determine the trap energy level below the conduction band.

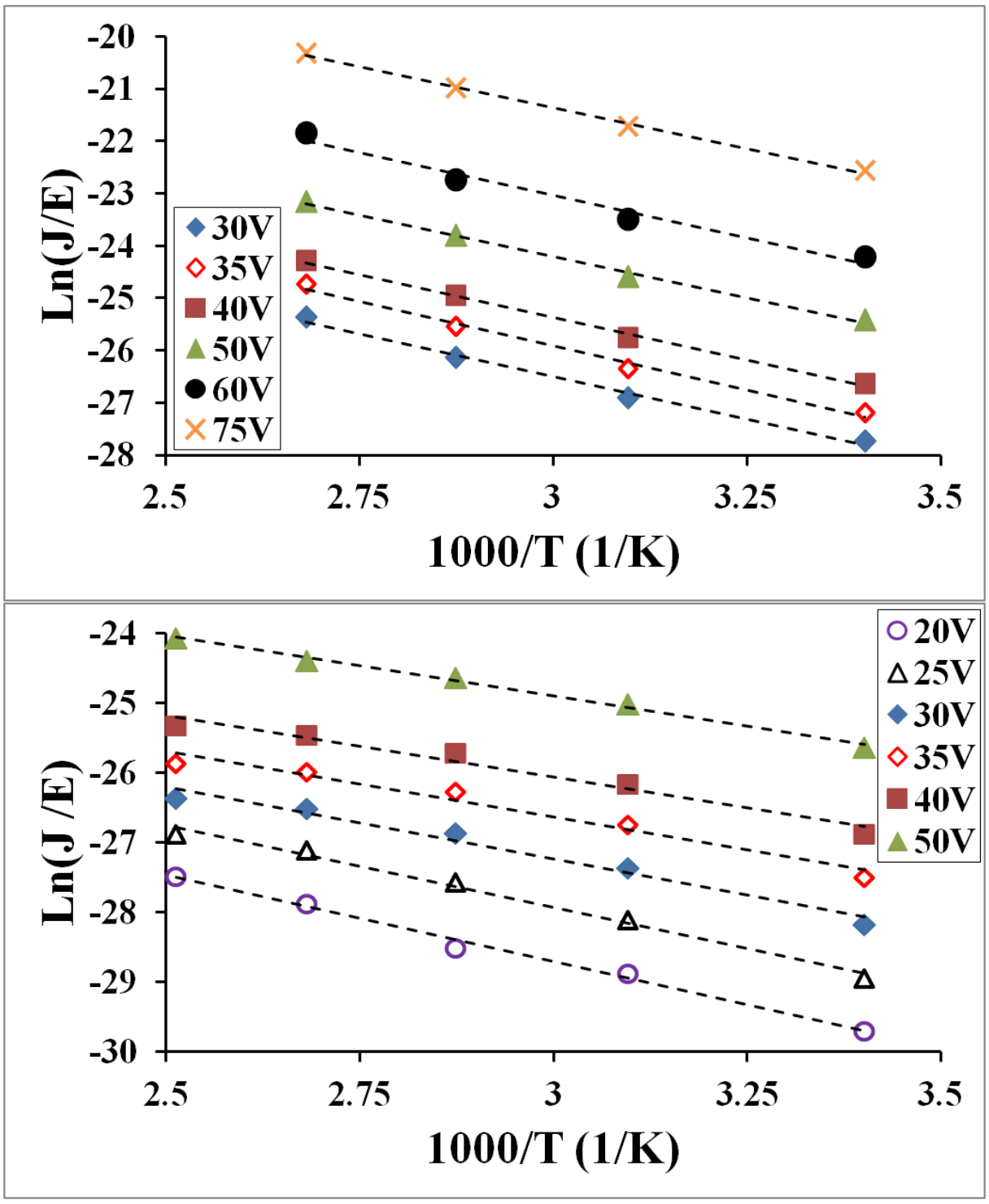

Figure 2.17 Poole-Frenkel Arrhenius plot of leakage current measured at different stress voltages for the positive bias, temperature range 21-100˚C (top) and the absolute values of the negative bias, temperature range 21-125˚C (bottom).

According to the equation (20) the value of the slopes should decrease with increasing electric field, there is a distinct trend towards that direction. A linear fit was applied to the data with an R^2 = 0.7707 and the trap energy below the conduction band was calculated from the y intercept, ϕ_t ~ 0.33 eV. However, this data indicates that the Poole-Frenkel is clearly not the dominant conduction mechanism due to the reduced trap barrier height not decreasing sequentially for increasing electric field as the theory predicts.

Similarly, the slopes from the Arrhenius plot for the negative bias in the voltage and temperature ranges, 20 V - 50 V, 21˚C - 125˚C, were plotted in Figure 2.18 (bottom). The results were in reasonably good agreement with Poole-Frenkel as the reduced trap barrier height decreases with increasing electric field and the linear fit had an R^2 = 0.9202. The trap energy below the conduction band was calculated, ϕ_t ~ 0.33 and the value was in agreement with the value for the positive bias.

A linearised version of the Schottky emission equation was plotted as $\ln(J_{SE}/T^2)$ versus $1/T$ to observe Arrhenius behaviour. The slope was as follows

$$m = \frac{q\phi_B - \sqrt{q/4\pi\varepsilon_0\varepsilon_r}\sqrt{E}}{\xi k_B} \qquad (22)$$

As with the Poole-Frenkel analysis, m versus $\sqrt{E}$ was plotted for a number of electric field values in the positive and negative biases and ϕ_B was calculated at $\sqrt{E} = 0$.

$$y_0 = \frac{q\phi_B}{\xi k_B} \qquad (23)$$

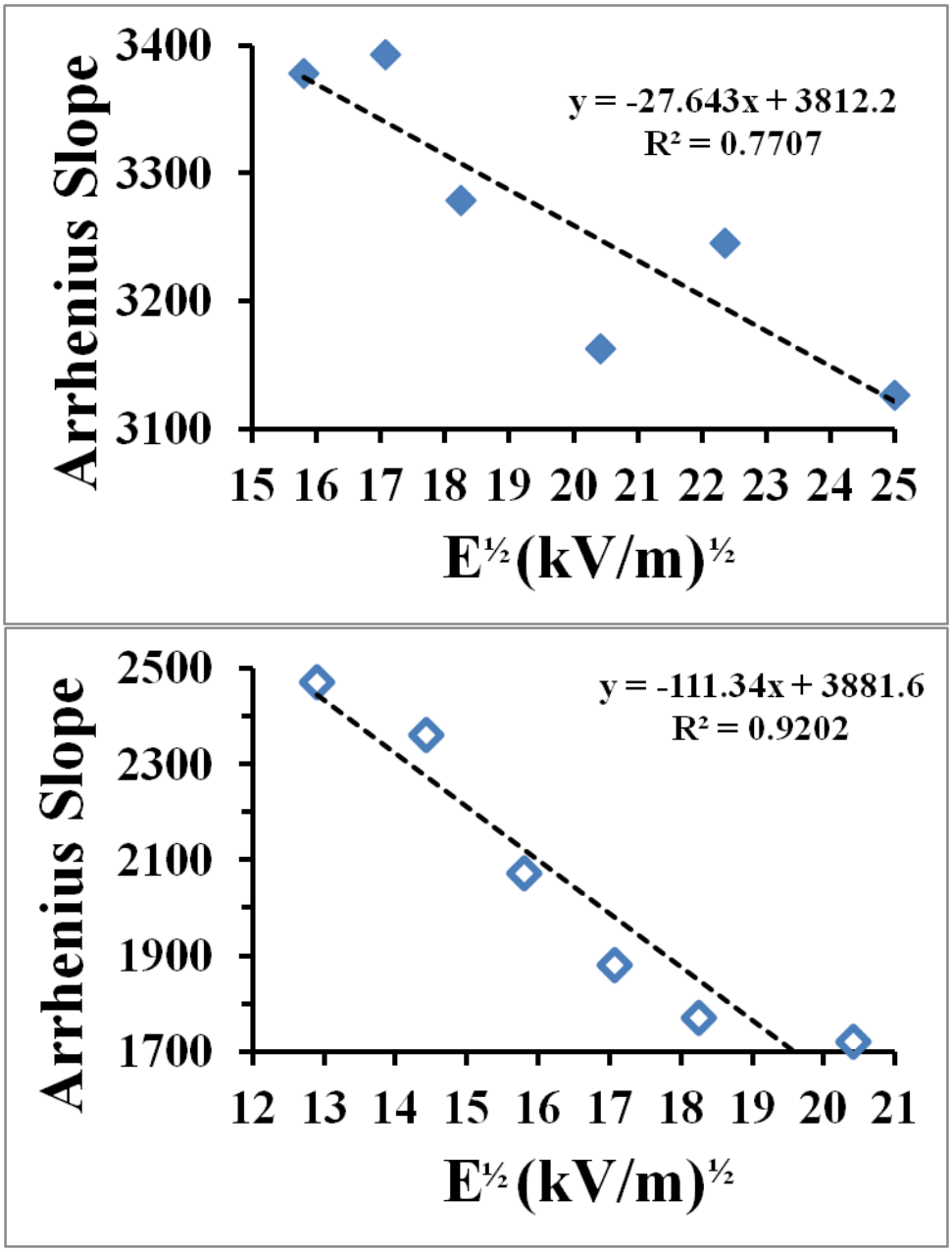

Figure 2.18 The slopes of the Arrhenius plots in Figure 2.17 were plotted versus √E according to equation (20) for the positive (top) and negative (bottom) biases. The trap energy barrier may be calculated from the y intercept in the provided equations in each plot.

The slopes from the Arrhenius plot (positive I-V sweeps on the gate) for various voltages (35-75 V) were plotted in Figure 2.20 (top) to check whether Schottky emission was the dominant mechanism in the positive bias and to calculate the Schottky barrier energy. Again, the slopes should decrease with increasing electric field, however, a trend is apparent (R^2=0.69). A linear fit was applied to the data with an R2 = 0.6917 and the Schottky barrier energy was calculated from the y intercept, ϕ_B ~ 0.27 eV. This value does not agree with the conduction band offset / Scottky emission barrier in these structures which was estimated at ϕ_B $\geq$ 2.2 eV. It was calculated from the work function of aluminium ~ 4.2 eV [162] minus the electron affinity for HfO_2 ~ 2.0 [163].

It was assumed that the electron affinity of the $HfSiO_x$ was similar to or likely lesser than that of HfO_2 due to the presence of the SiO_2 content whose electron affinity ~ 1.1 eV [26]. The indications for Poole-Frenkel as the dominant mechanism for the electron injection (negative bias on the gate) are much stronger and Shottky emission can ultimately be dismissed based on this data.

Similarly, the slopes from the Arrhenius plot for the negative bias on the gate in the voltage and temperature ranges, 20 V - 50 V, 21˚C - 125˚C, were plotted in Figure 2.20 (bottom). The slopes decrease with increasing electric field and the linear fit had an R^2 = 0.9201. The Schottky barrier at zero volts was calculated, ϕ_B ~ 0.28 and again this falls far short of the expected value. The indications for Poole-Frenkel as the dominant mechanism for the electron injection (negative bias on the gate) are much stronger and Shottky emission can ultimately be dismissed based on this data.

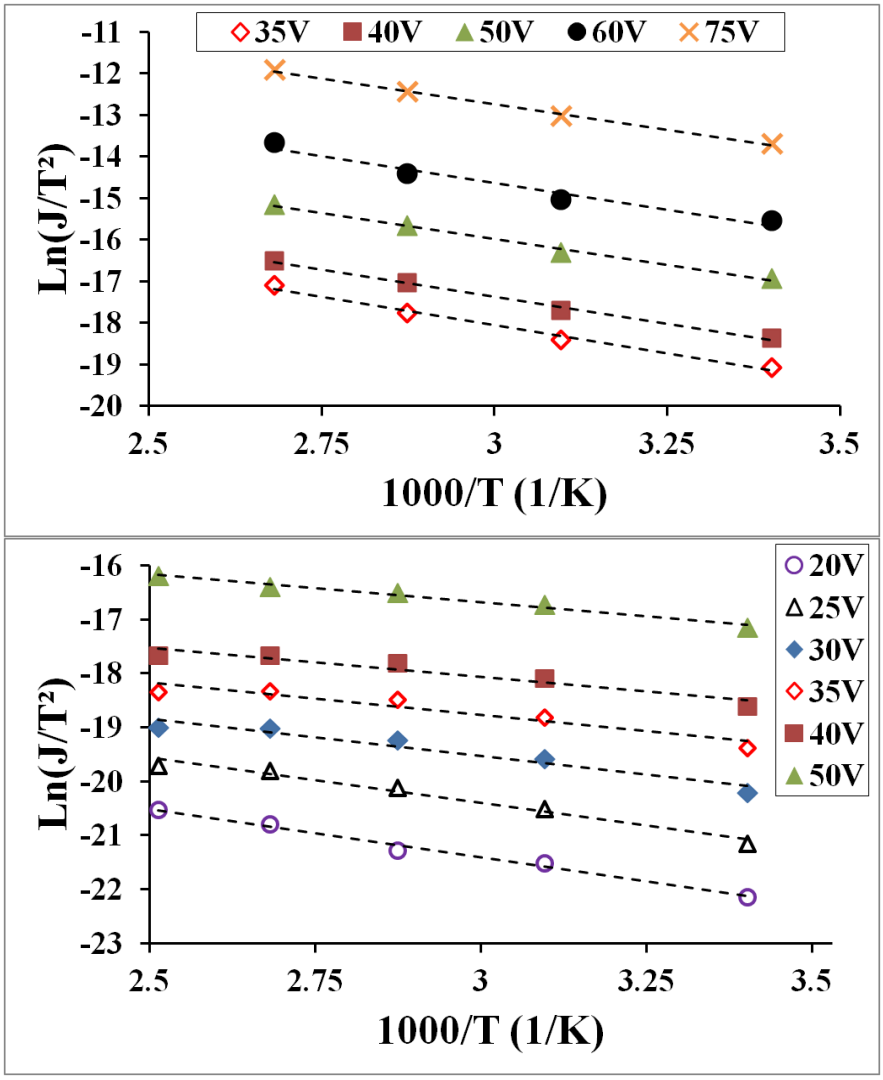

Figure 2.19 Schottky emission Arrhenius plot of leakage current measured at different stress voltages for the positive bias, temperature range 21-100˚C (top) and the absolute values of the negative bias, temperature range 21-125˚C (bottom).

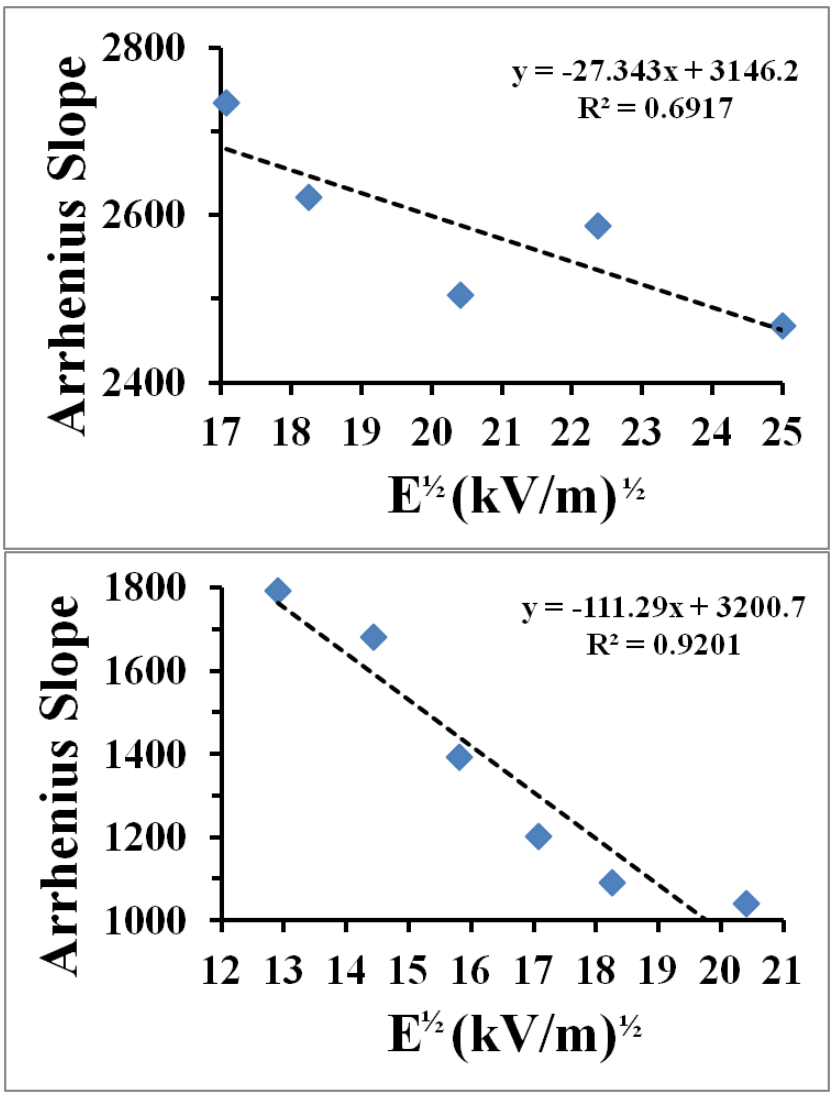

Figure 2.20 The slopes of the Arrhenius plots (Schottky) in Figure 2.19 plotted versus √E according to equation (22) for the positive (top) and negative (bottom) biases.

Ultimately, while Poole-Frenkel was likely the dominant leakage mechanism for electron injection from the gate, the dominant mechanism for electron injection from the substrate (voltage range of 25 V to 60 V, from 21˚C to 125˚C) is less clear due to the lower value of the coefficient of determination (R^2). Tunnelling mechanisms are not deemed appropriate due to the $HfSiO_x$ film thickness ~ 120 nm. The electron

injection is from the aluminium substrate electrode in this bias and both electrodes are sputtered aluminium with no adhesion layer, hence, electron injection from either would likely lead to conduction by the same mechanism. However, the bottom electrode may have a native Al_2O_3 layer as shown in Figure 2.21 which is not present at the top electrode interface. It would seem reasonable that this may influence the electron injection at the interface and affect the conduction mechanism. Electron injection from this interface results in a substantial increase in current with temperature compared to electron injection from the gate interface (without an interlayer) as shown in Figure 2.12. The analysis has shown that neither Poole-Frenkel nor Scottky emission are responsible and further investigation is required to identify the dominant conduction.

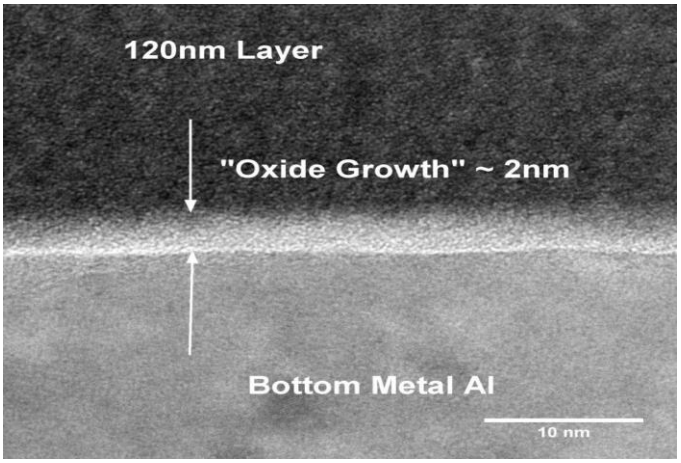

Figure 2.21 Cross-section TEM of a 120 nm thick hafnium silicate dielectric showing the interface at the bottom aluminium electrode, an interfacial layer is indicated.

2.4 Conclusions

Electrical characterisation was carried out on 120 nm $HfSiO_x$ MIM capacitors (1 x 10^{-8} m^2) with aluminium electrodes. Weibull statistics were applied and resulted in the following, β = 3.4, maximum operational voltage for 10 year lifetime at 63% cumulative failure = 58 V and this was scaled to 0.1 cm^2 0.01% 10 year lifetime where the maximum operational voltage was 49 V. The field acceleration factor was ~ 6.0 cm/MV, activation energy for bond breakage ΔH_0^* value ~ 1.3eV and a ~ 15.2 eÅ were also determined. There was a large amount of electron trapping at low voltage 76 V which was rarely observed at voltages higher than ≥ 76.5 V. The leakage current was up to three orders of magnitude greater at t_0 than for the rest of the measurement for all data sets and was considered to be related to positive charge in the oxide possibly defects at the interfaces. This current decreased with time under CVS and this was attributed to charge trapping. A large amount of electron trapping is observed for CVS at 76 V and the mechanism responsible for this appears to activate at lower field strength. This may indicate that different mechanisms operate at high and low fields in this material which adds more complexity to the extrapolation of lifetimes at device operation fields. The conduction mechanisms for electron injection from the substrate and gate interfaces were further investigated by multiple temperature I-V sweeps on the gate electrode. Schottky and Poole-Frenkel emission were considered likely candidates. Schottky emission was fitted to the data and resulted in the following, ϕ_B ~ 0.28 eV (electron injection from the gate) and ϕ_B ~ 0.27 eV (electron injection from the substrate), ε_r ~ 4.1 – 1.9 and n ~ 2 – 1.4. Poole-Frenkel fitting to the data resulted in the following ϕ_t ~ 0.33 (electron

injection from the gate) and ϕ_t ~ 0.33 eV (electron injection from the substrate), ε_r ~ 5.1 – 3.4 and n ~ 2.3 – 1.8, The Poole-Frenkel mean value for n ~ 2.1 ± 0.2 would indicate a low Si content in the hafnium silicate and as mention earlier the E_{BD} ~ 8.1 agrees well with a value in the literature that has a 20% Si content.

An Arrhenius analysis was performed to further investigate both conduction mechanisms and resulted in the dismissal of Schottky emission for electron injection from both interfaces due to the difference in the calculated barrier energy value, ϕ_B ~ 0.28 eV and ϕ_B ~ 0.27 eV (electron injection from the gate and substrate respectfully), compared to the estimated Schottky barrier, $\phi_B \geq 2.2$ eV (Al work function 4.2 eV – 2.2 eV electron affinity HfO_2). Poole-Frenkel was considered a good candidate for the dominant conduction mechanism for electron injection from the gate with trap energy below the conduction band of ϕ_t ~ 0.33 eV. However, for the electron injection from the substrate it is less clear due to the lower value of the coefficient of determination (R^2). This may be attributed to an interlayer, possibly Al_2O_3, at the substrate interface. Further investigation is required to fully identify the dominant conduction mechanism from this interface.

3. Time Dependent Dielectric Breakdown Study of Gamma Ray Irradiated Hafnium Silicate Metal-Insulator-Metal Capacitors

3.1 Introduction

Electronic systems operating in radiation environments such as space vehicles, satellites, medical imaging and nuclear facilities are exposed to considerable radiation doses. The performance of CMOS devices has improved with respect to Total Ionizing Dose (TID) effects due to continuous scaling of dielectrics which has reduced charge trapping [164]–[166]. However, analog applications rely on thicker dielectrics and these older technology nodes are more susceptible to TID effects [167]–[169]. In particular, space systems tend to be conservative and use electronics that are several generations behind the latest technology node. There are large gains to be made from leveraging newer technology nodes such as reducing weight, power and cost while increasing functionality, efficiency, redundancy and capability. However, while the radiation response of a traditional dielectric such as SiO_2 is reasonably well understood [170] scaling has led to the necessity to integrate high-*k* dielectrics of which little is known about the radiation response of these materials. Although, some studies in the literature have found irradiation damage in materials such as HfO_2 and others has resulted in trapped positive charge in the bulk and at the interfaces which has degraded the performance of the devices and their reliability [171]–[174].

Gamma ray irradiated hafnium silicate devices were previously reported to perform well compared to HfO_2 and the level of radiation hardness was considered similar to that of SiO_2, however, with an increased level of defects [175]. In the previous chapter, hafnium silicate metal-insulator-metal (MIM) capacitors with k ~ 13.2 were determined to have excellent reliability characteristics (Chapter 2) and could possibly be a replacement candidate material for SiO_2 in analog applications. Hence, in this chapter the reliability of gamma ray irradiated hafnium silicate devices was characterized for possible use in radiation environments.

3.2 Materials and Methods

All devices characterised in this chapter were fresh untested devices from the same wafer as the material in chapter 2. The data in this study was measured on the following devices, square MIM capacitors with an area of 10^{-4} cm^2 and 120 nm of $HfSiO_x$ between top and bottom aluminium electrodes.

3.2.1 Irradiation conditions

A fully processed sample was diced in to three samples and one piece was kept as a control sample while the other two were irradiated as follows. The two samples were irradiated at zero volts using gamma radiation from a Co^{60} source, total dose for sample one was 16 krad (Si) at 210rad/mi and total dose for sample two was 78 krad (Si) also at 210 rad/min. The 16 krad (Si) sample was designed to simulate the expected dosage at low earth orbit (LEO) shielded and similarly for the 78 krad (Si) sample, LEO unshielded.

3.3 Results and Discussion – Electrical Characterisation and Analysis

The TID response of hafnium silicate MIM capacitors was investigated for specific total radiation dosages corresponding to the expected conditions for shielded and unshielded electronics in low earth orbit. Gamma ray radiation may break the ionic bond between Hafnium and oxygen bond and create oxygen vacancies [176]. Multiple I-V sweeps in both polarities were performed on the sample which had received a total dose of 16 krad(Si) from a gamma-ray Co^{60} source. This radiation dosage has not increased the leakage current response or indeed, reduced the electric field breakdown value (E_{BD} ~ 8.1 MV/cm) when compared to the control sample as shown in Figure 3.1.

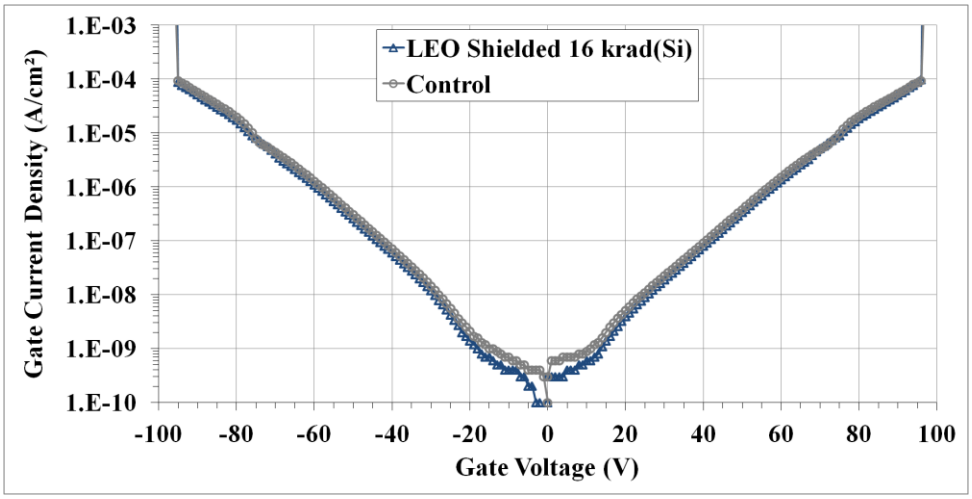

Figure 3.1 J-V traces for both polarities for 16 krad(Si), low earth orbit shielded, sample and non-irradiated control sample for comparison.

Similarly, multiple I-V measurements were performed for both polarities on the 78 krad(Si) sample. The leakage current was consistent in the negative sweep, although, there was some dispersion mostly up to ~ 40 V in the positive sweep as shown in Figure 3.2 and the breakdown voltages were consistent. Leakage current was comparable with the control sample, though, as mentioned earlier the positive sweep deviated slightly from the control sample. The leakage mechanism was analysed previously (Chapter 2) and found to differ depending on the bias sweep polarity on the gate. The gamma-ray irradiation appears to modify the positive gate bias sweep mechanism (≤ 40 V) which was not previously identified; however, Poole-Frenkel and Shottky emission were both excluded after an Arrhenius type analysis. The negative bias sweep on the gate which was determined as Poole-Frenkel is not affected by this radiation dosage. Also, minor degradation in the E_{BD} ~ 7.8 MV/cm was apparent in Figure 3.2 and this differential was symmetric for both polarities.

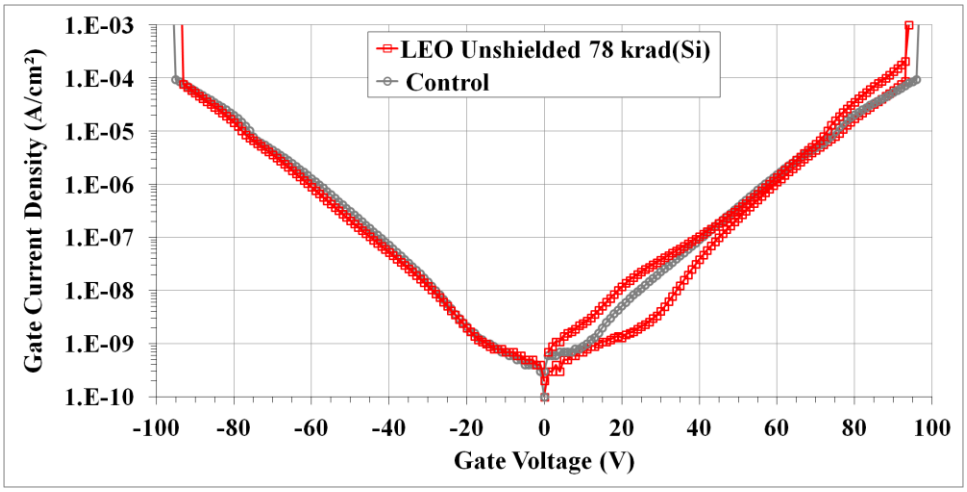

Figure 3.2 J-V traces for both polarities for 78 krad(Si), low earth orbit unshielded, sample and non-irradiated control sample for comparison.

The C-V sweeps for both 16 krad(Si) and 78 krad(Si) total dose showed practically no hysteresis as shown in Figure 3.3, top and bottom respectively. In Figure 3.3 zero volt capacitances, C_0 ~ 0.94 fF/um^2 (top) and 0.965 fF/um^2 (bottom), compared well with the control sample C_0 ~ 0.975 fF/um^2, deviation of ~ 3.5% which is within expected margins for ALD. Hence, the radiation dosages appeared not to degrade the dielectric films' capacitance properties for both sweep biases on the gate even though the positive bias sweep I-V showed some deviation.

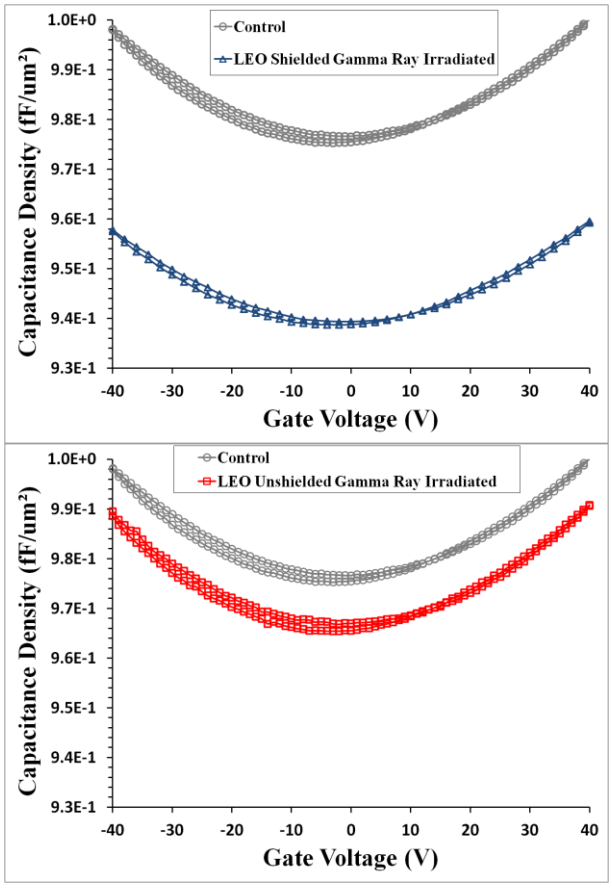

Figure 3.3 CD-VG double sweeps for LEO shielded gamma ray-irradiated total dose 16 krad(Si) sample (blue triangle) and control sample (top) and also LEO unshielded gamma-ray irradiated total dose 78 krad(Si) sample (red squares) and control sample (bottom).

The non-linear change in capacitance with voltage can be analysed by fitting $\Delta C/C_0$ versus V with a second order polynomial [35]

$$C(V) = C_0(\alpha V^2 + \beta V + 1) \qquad (1)$$

where α and β are quadratic and linear voltage coefficients of capacitance respectively. The value of α (< 100 ppm/V^2) is important for certain applications such as RF or AMS. α tends to increase significantly with decreasing film thickness. The quadratic voltage coefficient of capacitance calculated from (1) at 1 kHz was found to deviate from α ~ 14.4 ppm/V^2 for the 16 krad(Si) sample to α ~ 15.4 ppm/V^2 for the 78 krad(Si) sample, Figure 3.4 middle and bottom respectively. These values were in reasonable agreement with the control sample at 1 kHz, α ~ 15.0 ppm/V^2, Figure 3.4 top. α was observed to decrease with increasing frequency and at approximately the same rate for the irradiated and control samples as shown in Figure 3.4. These radiation dosages appear not to influence the mechanism that manifests itself as the capacitance-voltage nonlinearity described by the α parameter in this 120 nm hafnium silicate film.

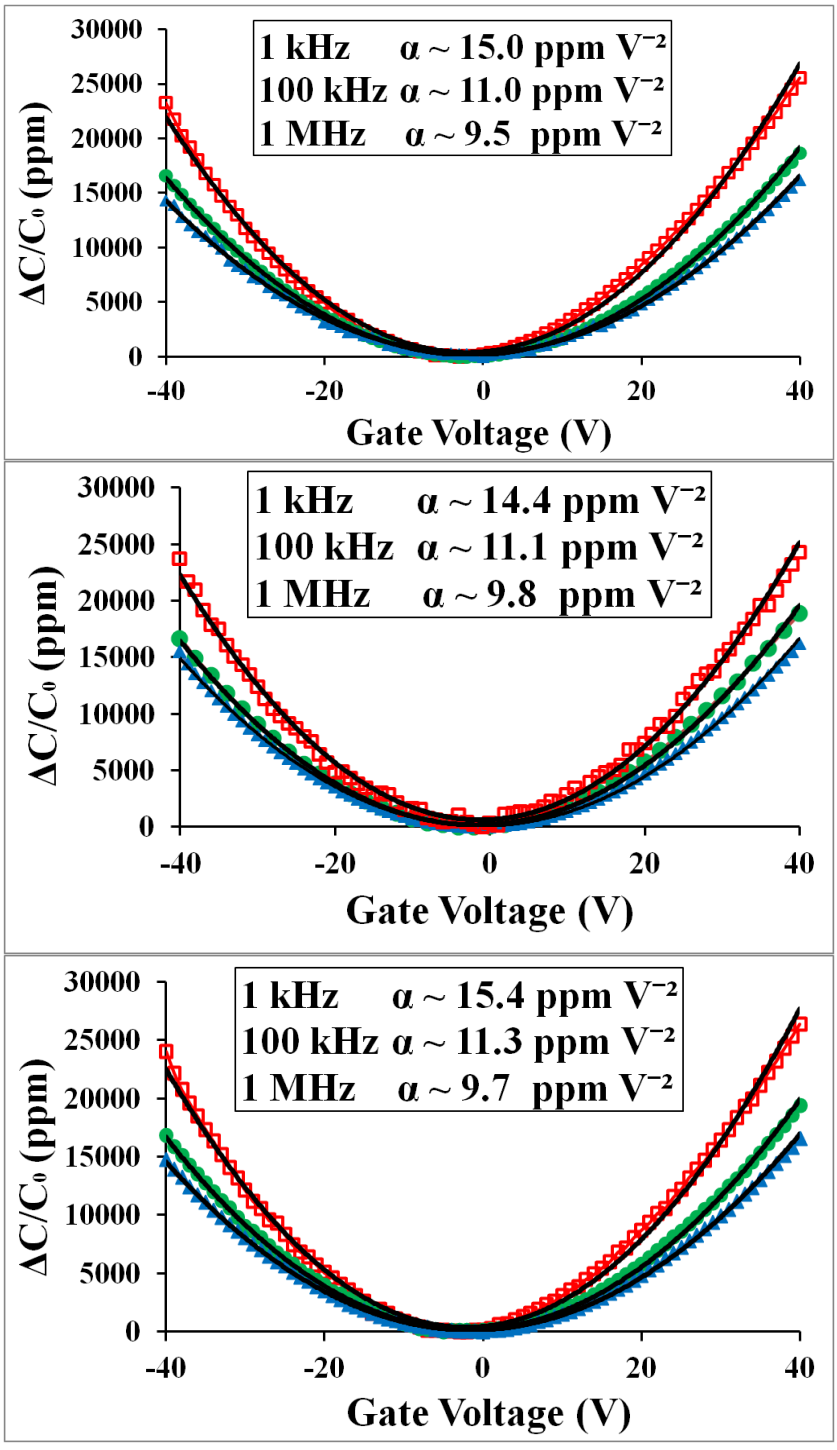

Figure 3.4 Quadratic voltage coefficient of capacitance (α) extracted from polynomial fit to normalised capacitance at 1 kHz, 100 kHz and 1 MHz for the control sample (top), 16 krad(Si) (middle) and 78 krad(Si) (bottom).

3.3.1 Reliability Characterisation and Analysis

The intrinsic reliability of the control hafnium silicate film has been previously investigated (Chapter 2) by the time dependent dielectric breakdown methodology (TDDB) and the I-t traces (CVS) are shown below in figure 2.4 for comparative purposes. Noticeably, the I-t traces are grouped together according to the CVS voltage, ie: essentially very little dispersion in the leakage current trace at each stress voltage until electrical breakdown. The leakage current decreased with time which was indicative of electron trapping in the bulk [147] and this was more evident in some of the I-t traces where considerable electron trapping and de-trapping was observed, typified by a type of oscillation behaviour in the leakage current, most obvious at 80 V in figure 3.4. However, the rate of decline in leakage current moderates with time and this may be due to stress induced defects such as neutral traps which result in a stress induced leakage current (SILC) component [148].

There was a slight increase in the dispersion of the I-t traces for positive bias CVS on the gate of the 16 krad(Si) sample, in Figure 3.5. This was observed for the higher electric field CVS measurements, 92 V and 88 V, while the 84 V and 80 V measurements were similar to the control sample. This was considered to be as a result of minor radiation induced damage. The shape of the I-t traces themselves were similar to the control sample were the leakage current reduced with time and the rate of this reduction moderated with time. Also, there was some oscillation in the leakage current in a small number of the measurements, particularly noticeable at 84 V. Again, electron trapping was considered responsible for the above observations.

Overall, the total radiation dose that this sample was subjected to appears to have resulted in minimal damage to the electronic properties.

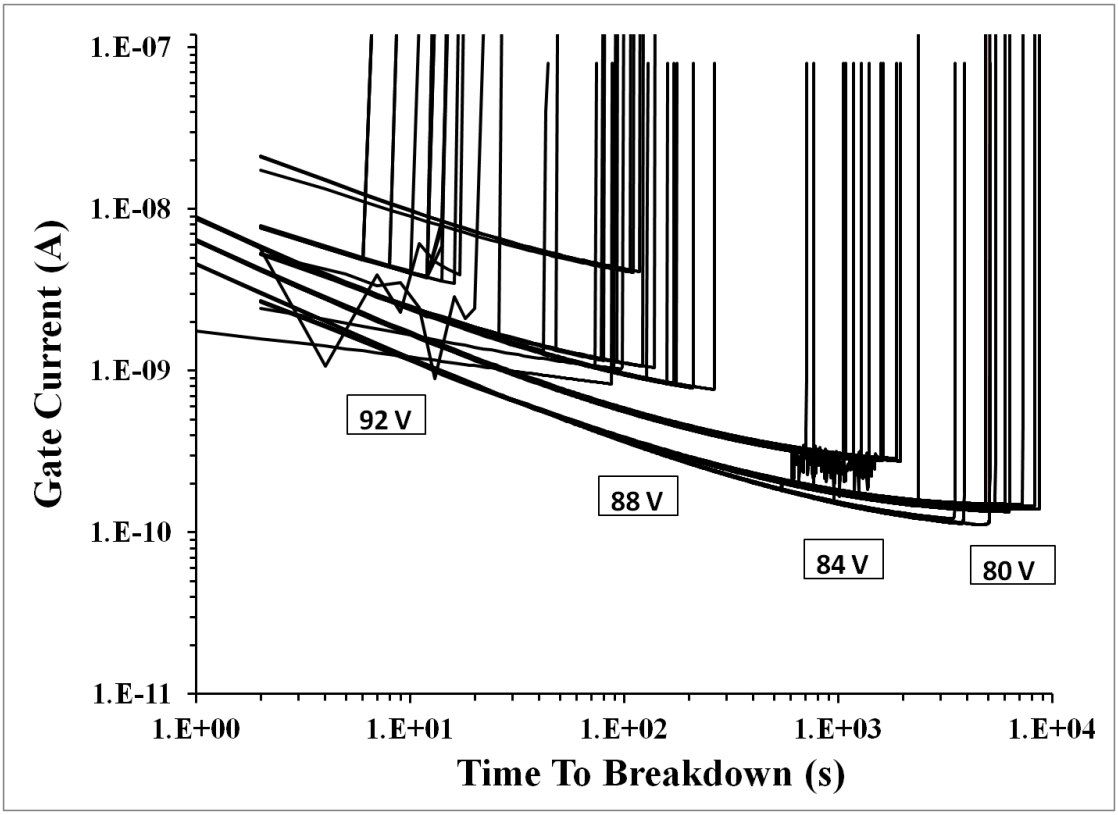

Figure 3.5 I-t traces corresponding to constant voltage stress (CVS) data at 92, 88, 84 and 80 V for the 16 krad(Si) gamma-ray irradiated sample. All measurements were performed with a positive CVS on the gate.

The CVS I-t traces in Figure 3.6 were broadly similar to the control sample, leakage current reducing and moderating with time. Although, the dispersion in the traces has increased considerably for the 78 krad(Si) sample compared to the control sample. This dispersion is evident for all measured electric fields; however, no leakage current oscillation was observed. The breakdown behaviour was hard, no soft or progressive breakdown features which was consistent with the other samples.

However, there was a distinctive shift to reduced time to breakdown for the measurements. The total radiation dosage of 78 krad(Si) appears to have generated an increased level of damage in the dielectric which has influenced the leakage mechanism in the positive CVS bias on the gate.

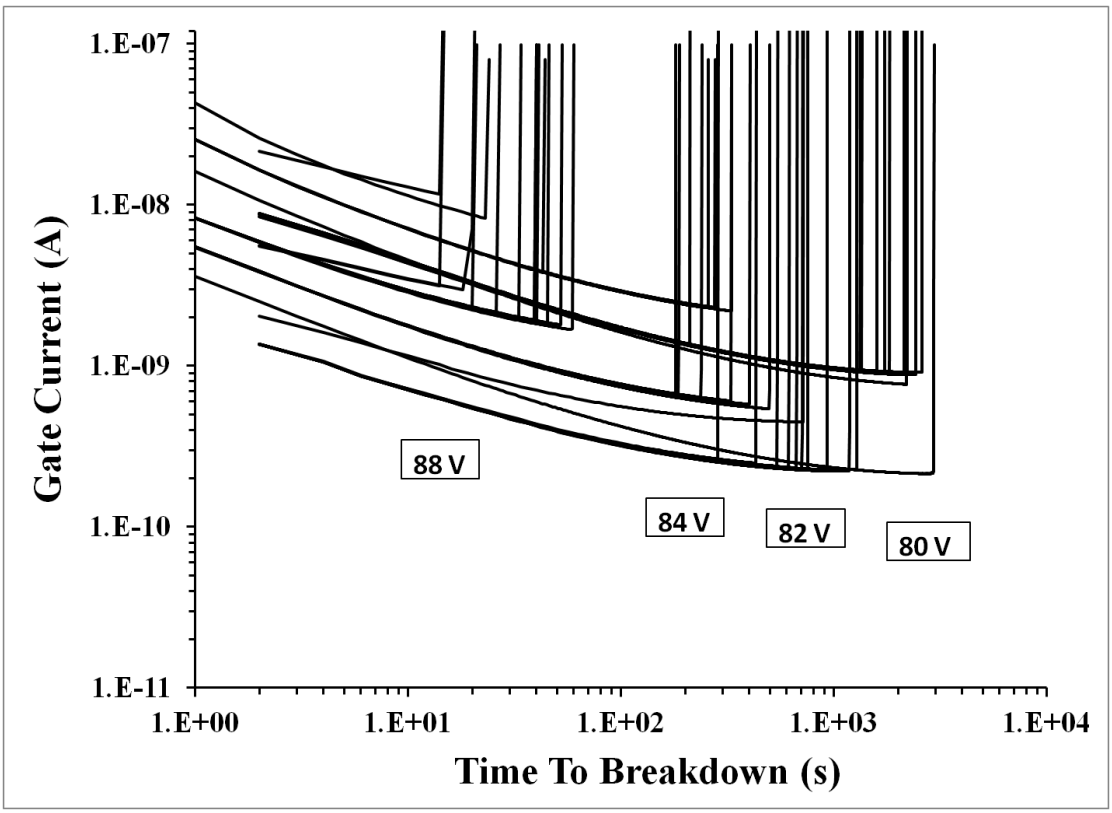

Figure 3.6 I-t traces corresponding to constant voltage stress (CVS) data at 88, 84, 82 and 80 V for the 78 krad(Si) gamma-ray irradiated sample. All measurements were performed with a positive CVS on the gate.

Approximately 110 CVS measurements were taken according to the time dependent dielectric breakdown (TDDB) methodology between the 16 and 78 krad(Si) samples. This time to breakdown (t_{BD}) data was analysed using a two parameter Weibull. The measurements consisted of four distributions per sample from which the shape

parameter (β) and the scale factor (n) which is normally determined at 63% cumulative failure (n_{63}) were determined by maximum likelihood algorithm fitting.

The Weibull distributions of the t_{BD} at four stress voltages for the 16 krad(Si) sample are shown below in Figure 3.7 and the average value of β for the four distributions was ~ 3.3. This compares very well with the value for the control sample that was determined previously β ~ 3.4 (Chapter 2). In addition, the t_{BD} at 63% cumulative failure, n_{63}, is indicated at each voltage in Figure 3.7. The distributions for the 16 krad(Si) sample are broadly similar to the control sample (not shown) and the radiation dosage does not appear to affect the Weibull parameters.

Again, a two parameter Weibull analysis was performed on the t_{BD} data for the 78 krad(Si) sample as shown in Figure 3.8. The average value for β from the four distributions was ~ 3.2 which would suggest good agreement with the control sample and the n_{63} values are indicated in Figure 3.8 and they would point to degradation in the values compared to the control sample.

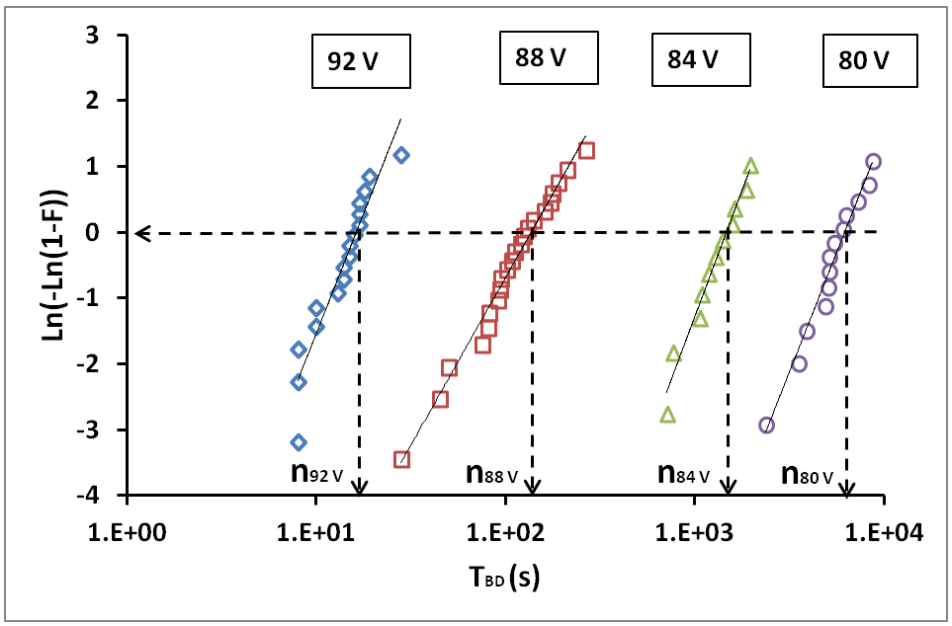

Figure 3.7 Weibull distributions for breakdown time results from CVS with positive bias on the gate for 16 krad(Si) gamma ray irradiated sample. The median value of β ~ 3.3 and the n63 values for each voltage are indicated on the plot.

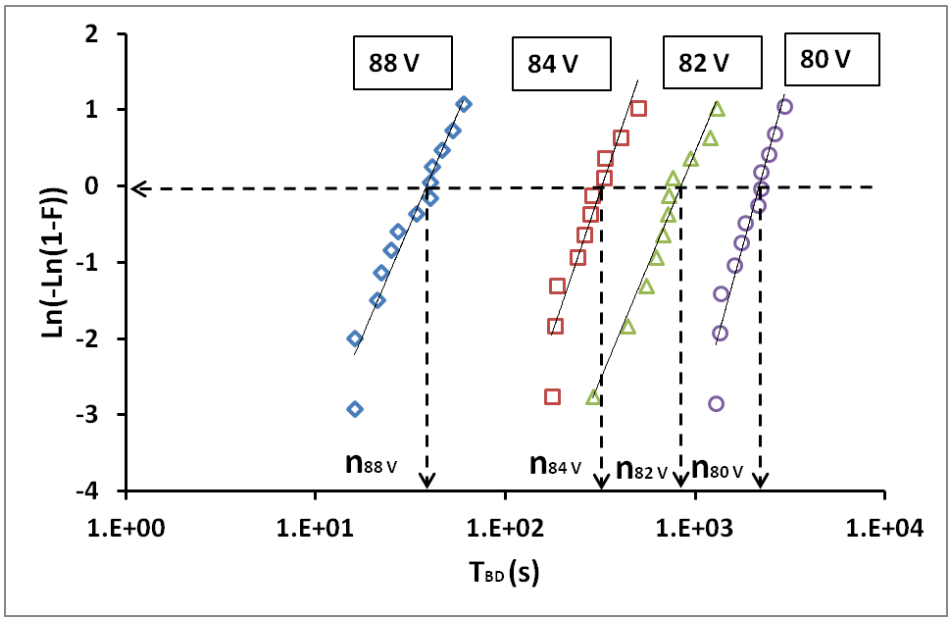

Figure 3.8 Weibull distributions for breakdown time results from CVS with positive bias on the gate for 78 krad(Si) gamma ray irradiated sample. The median value of β ~ 3.2 and the n63 values for each voltage are indicated on the plot.

The n_{63} values of the of the control and 16 krad(Si) samples are in excellent agreement as shown in Figure 3.9. As alluded to earlier, the 78 krad(Si) n_{63} values have decreased in a uniform manner for the four distributions compared to the control sample in Figure 3.9 and this strongly indicates that minor gamma ray radiation induced damage has occurred relatively uniformly across the sample.

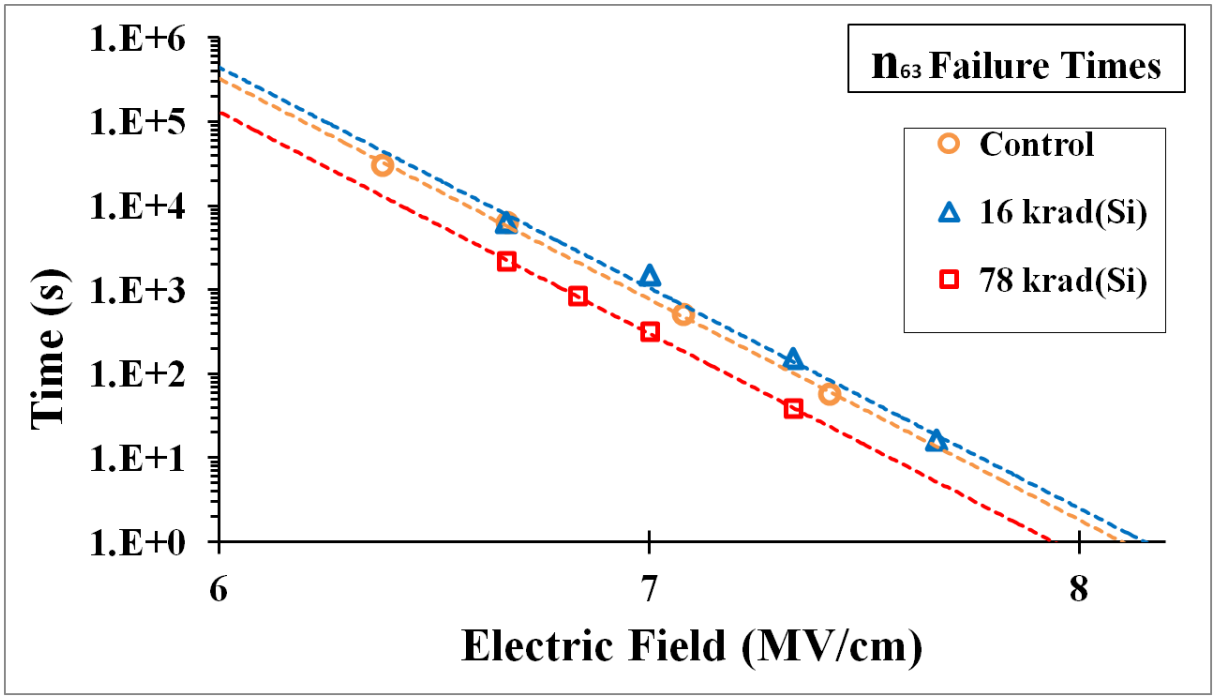

Figure 3.9 Time to breakdown values for 63% cumulative failure, n63, for each of the four distributions per sample, control, 16 krad(Si) and 78 krad(Si).

The values shown in table 1 (left) tend to indicate an increasing spread in β as the dosage of gamma ray radiation increases. This trend is not apparent from the average β values discussed earlier. The β and n_{63} values for the 80 V CVS distributions are

shown in table 1 (right) and the indicated trend in β is apparent. Also, the 80 CVS n_{63} values for the 78 krad(Si) sample have show a considerable decrease (~ 60%) when compared to the other two samples.

Table 3-1 (left) Comparison of spread in β values for all CVS distributions at various voltages for the three samples. (right) Comparison of Weibull parameters for the 80 V CVS distributions for Control, 16 krad(Si) and 78 krad(Si) samples.

β	**β**	**β**
0 krad(Si)	**16 krad(Si)**	**78 krad(Si)**
3.4	3.1	2.7
3.3	2.8	3.2
3	3.8	2.8
3.2	3.5	4.2

CVS @ 80 V		
Radiation Dose krad(Si)	**β**	**n_{63} (s)**
None	3.0	6296.1
16	3.5	6199.3
78	4.2	2173.5

A representative selection of the I-t traces at 80 V CVS for the three samples are shown below in Figure 3.10. A trend was observed in all of the CVS traces of leakage

current decreasing with time according to a Power Law dependence, Curie-von Schweidler law, for which defect generation and/or electron trapping have been shown to be responsible [177]–[179].

However, there was a tendency to deviate from this Power Law dependence as shown in Figure 3.10, it has been suggested that stress induced leakage current (SILC) is responsible for this deviation [180]. However, the SILC component is larger for the 78 krad(Si) sample, Figure 3.10, and this increase may possibly be attributed to radiation induced leakage current (RILC) [181]. Both 78 krad(Si) I-t traces below have approximately the same shape but their leakage current values differ by almost an order of magnitude which may indicate localised neutral traps generated by the radiation.

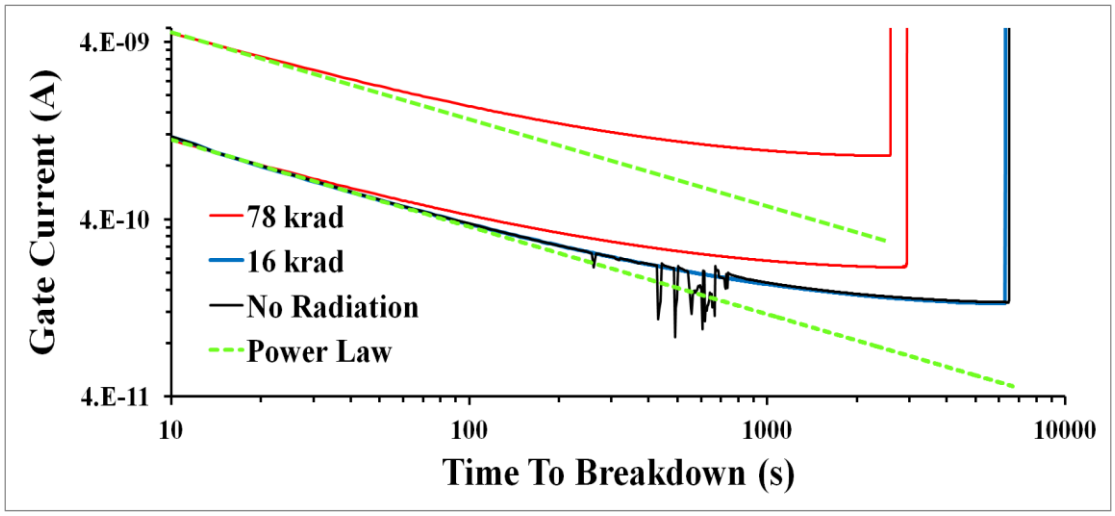

Figure 3.10 I-t traces for at 80 V CVS for control (black), 16 krad(Si) (blue) and 78 krad(Si) (red) samples. Leakage current under CVS has been shown to follow a Power Law dependence and this is extrapolated (green) for comparison with the leakage current traces.

The lifetime at specification conditions was determined as follows. The n_{63} values are determined by extrapolating the gate voltage to the operational range of interest ((30, 35 and 40) V 30% to 40% of E_{BD} for analogue device operation) using the Linear E-model below.

$$t_{BD} = t_0 e^{-\gamma E} \qquad (2)$$

where t_{BD} is the time to electrical breakdown, E is the electric field and γ is the field acceleration parameter. The values are area scaled to specification area of 0.1 cm^2 [151] and then scaled to failure percentiles of 0.01%. The scaling equations for voltage, area and failure percentiles, (3), (4) and (5) respectively are specified below.

$$n_2 = t_0 exp(c v_2) \qquad (3)$$

$$n_2 = n_1 \left(\frac{A_1}{A_2}\right)^{1/\beta} \qquad (4)$$

$$\ln[-\ln(1-F)] = \beta \ln t - \beta \ln n \qquad (5)$$

where n_2 is the scaled or extrapolated lifetime, c is a constant, v_2 is the voltage chosen to calculate the lifetime, n_1 is 63% cumulative failure lifetime, A_1 and A_2 are the measured device area and approximate chip area respectively, F is the cumulative failure, t is the time and n is the lifetime.

The maximum operating voltage of the control sample to guarantee 20 years lifetime was ~ 48 V as shown in Figure 3.11. The field acceleration parameter as determined from the Linear E-model fit (2) to the n_{63} value was determined previously as γ = 6.0 cm/MV (Chapter 2), Figure 3.11 (inset).

According to the Thermochemical model the local electric field distorts and weakens the enthalpy of activation (with E = 0) for bond breakage (ΔH_0^*) of polar molecules. The weakened bonds are more susceptible to breaking and this may result in the generation of neutral traps which may eventually lead to a conductive path (percolation theory) and then electrical breakdown of the dielectric [25]. The activation energy required for bond breakage in the absence of an electric field (ΔH_0^*) can be calculated from the following

$$\gamma E_{BD} = \frac{\Delta H_0^*}{k_B T} \qquad (6)$$

where k_B is the Boltzmann constant and T is the absolute temperature.

The effective dipole moment for bond breakage (a) can be determined from the following equation

$$\gamma = \frac{a}{k_B T} \qquad (7)$$

where the effective dipole moment for bond breakage $a = P_0(2 + k)/3$, the active molecular dipole moment is P_0 and k is the dielectric constant.

The extracted activation energy of bond breakage ΔH_0^* value calculated from (6) was ~ 1.23 eV and a ~ 15.2 eÅ was also determined from (7).

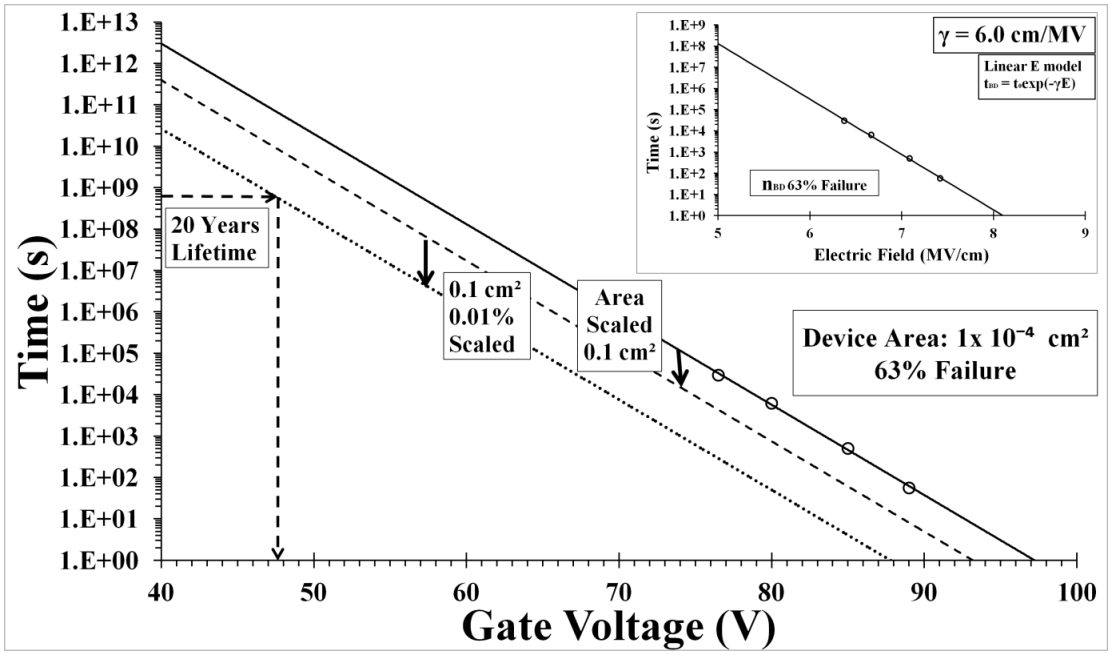

Figure 3.11 TDDB lifetime extrapolation of control sample. A linear E-model extrapolation of the n63 data was scaled to 0.1 cm2 and 0.01% failure, a maximum gate voltage of ~ 48 V was extrapolated to a guarantee a lifetime value of 20 years without hard breakdown and determination of the associated field acceleration parameter γ (inset).

The maximum operating voltage of the 16 krad(Si) sample to guarantee 20 years lifetime was ~ 48 V as shown in Figure 3.12. The field acceleration parameter, γ = 6.0 cm/MV as shown in Figure 3.12 (inset), was calculated from (2). The activation energy of bond breakage was determined from (6), ΔH_0^* ~ 1.23 eV, and the effective dipole moment for bond breakage a ~ 15.2 eÅ was also determined from (7). All three values compare very well with the control sample and the total radiation dosage of 16 krad(Si) appears to have had no impact on the reliability of the hafnium silicate.

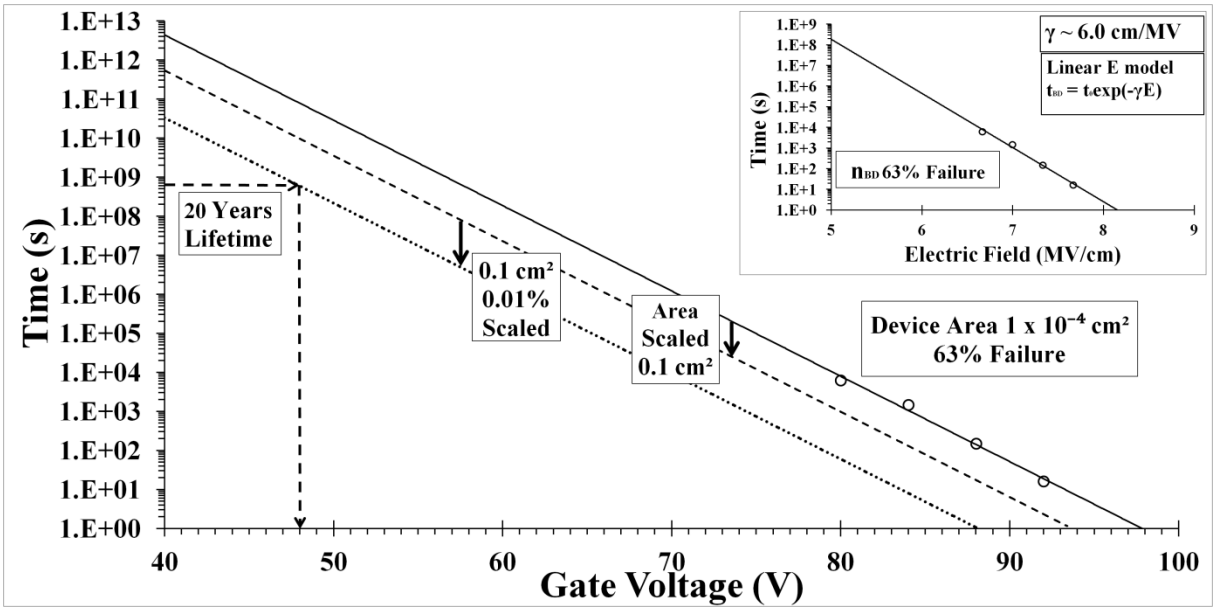

Figure 3.12 TDDB lifetime extrapolation of 16 krad(Si) sample. A linear E-model extrapolation of the n63 data was scaled to 0.1 cm2 and 0.01% failure, a maximum gate voltage of 48 V was extrapolated to a guarantee a lifetime value of 20 years without hard breakdown and determination of the associated field acceleration parameter γ (inset).

The same analysis of the 78 krad(Si) sample resulted in a 20 years lifetime maximum operating voltage of ~ 44 V as shown in Figure 3.13. The field acceleration parameter, from (2), showed a slight increase, γ = 6.1 cm/MV as shown in Figure 3.13 (inset). The activation energy of bond breakage, from (6), was similar, ΔH_0^* ~ 1.21 eV, and the effective dipole moment for bond breakage from (7) also increased, a ~ 15.5 eÅ. The total radiation dosage of 78 krad(Si) had resulted in a slight increase in γ and a while ΔH_0^* showed a slight decrease compared to the control sample. These small deviations along with the slight reduction in E_{BD} indicate that this level of total

gamma ray radiation dosage may have induced defects such as oxygen vacancies through the breaking of Hf-O bonds [176] by electron photon coupling. The overall effect on the hafnium silicate lifetime for space applications was a noticeable reduction of ~ 8%, however, the maximum V_{op} ~ 44 V was still considerably in excess of estimated requirements for analogue applications, ~ 29 – 38 V (~ 30 – 40% of E_{BD}).

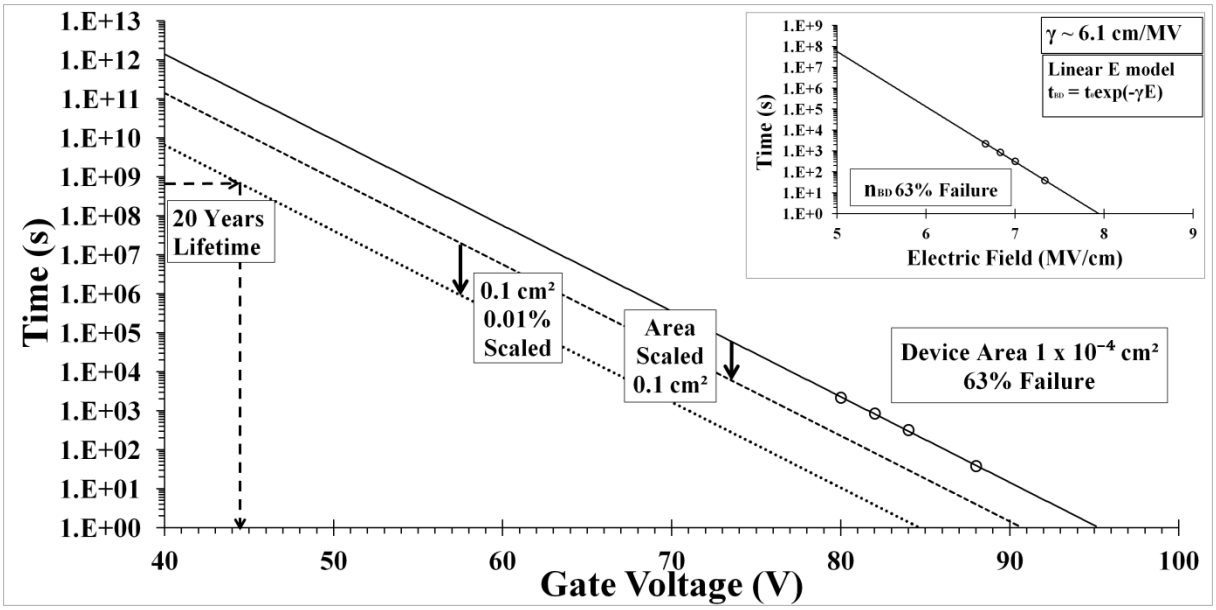

Figure 3.13 TDDB lifetime extrapolation of 78 krad(Si) sample. A linear E-model extrapolation of the n63 data was scaled to 0.1 cm2 and 0.01% failure, a maximum gate voltage of ~ 44 V was extrapolated to a guarantee a lifetime value of 20 years without hard breakdown and determination of the associated field acceleration parameter γ (inset).

3.4 Conclusions

An amorphous hafnium silicate film grown by ALD in MIM structures with sputtered top and bottom electrodes was subjected to gamma ray radiation at 210 rad/s from a C^{60} source. The total radiation dosages were 16 krad(Si) and 78 krad(Si) which were equivalent to shielded and unshielded total dosages for LEO satellites respectfully. The samples were characterised electrically (CV and IV) and TDDB reliability characterisation was also carried out.

E_{BD} for the 16 krad(Si) sample ~ 8.1 MV/cm and the C_D ~ 0.940 fF/um^2 compared very well with the non-irradiated control sample (E_{BD} ~8.1 MV/cm and C_D ~ 0.975 fF/um^2). The quadratic coefficient of capacitance α ~ 15.4 ppm V^{-2} (1 kHz), 11.3 ppm V^{-2} (100 kHz), 9.7 ppm V^{-2} (1 MHz) compared well with the control sample over a range of frequencies, α ~ 15.0 ppm V^{-2} (1 kHz), 11.0 ppm V^{-2} (100 kHz), 9.5 ppm V^{-2} (1 MHz). Also, leakage current from IV sweeps for electron injection from both electrodes was very consistent with the control sample. TDDB measurements were performed and similarly to the control sample, the shape of the CVS I-t traces generally followed a Curie-von Schweidler law dependency for which defect generation and/or electron trapping have been shown to be responsible. However, there was a little dispersion evident in the I-t traces compared to the control sample. A two parameter Weibull analysis in conjunction with maximum likelihood algorithm fitting was applied to the TDDB data, a β ~ 3.3 and a field acceleration parameter λ ~ 6.0 MV/cm were determined and this agrees remarkably well with the control sample. The maximum operational voltage for 20 year lifetime was area and percentile scaled from the n_{63} values at 63% cumulative failure to 0.1 cm^2 and 0.01% 20 year lifetime

where the maximum operational voltage was 48 V. The activation energy for bond breakage ΔH_0^* ~ 1.23 eV and the effective dipole moment a ~ 15.2 eÅ were also determined and were not impacted by the radiation dosage. In general, the properties of this 16 krad(Si) sample compared favourably with the control sample and it was concluded that this level of total radiation dosage (16 krad(Si)) does not impact the C_D, E_{BD} or reliability of this material.

E_{BD} of the 78 krad(Si) sample was ~ 7.8 MV/cm and there was slight reduction compared to the control sample, E_{BD} ~ 8.1 MV/cm. Leakage current was very similar for electron injection from the gate interface, however, there was some dispersion in the leakage current at low electric field (≤ 40 V) for electron injection from the bottom electrode. The C_D ~ 0.965 fF/um^2 and α ~ 15.4 ppm V^{-2} (1 kHz), 11.3 ppm V^{-2} (100 kHz), 9.7 ppm V^{-2} (1 MHz) compared well with the control sample. There was a large dispersion in the I-t traces for the TDDB CVS measurements and also, an overall reduction in t_{BD} which is reflected in the lifetime scaling and extrapolation of the n_{63} values. Furthermore, this reduction was consistent across the four voltages used for these CVS measurements, hence, the field acceleration parameter remained almost unchanged. Although, the maximum operational voltage for 20 year lifetime, area and percentile scaled was ~ 44 V which reflected this general reduction in t_{BD}. Though, the average shape parameter β ~ 3.2 and field acceleration parameter λ ~ 6.1 MV/cm were both reasonably consistent with the control sample. However, there was more spread in the β values which is not obvious from the presented average. The activation energy for bond breakage ΔH_0^* ~ 1.21 eV and the effective dipole moment a ~ 15.5 eÅ both showed minor deviation from the control sample which reflected the

deviations in E_{BD} and γ. This total radiation dosage of 78 krad(Si) had a slight effect on the reliability of this sample whereby a reduction of ~ 8% was observed in the 20 year lifetime maximum operational voltage. However, this value is still considerably above most operational ranges for analogue applications.

4. Reliability and Structural Investigation of Hafnium Silicate Grown on Various Electrodes

4.1 Introduction

Metal insulator metal (MIM) capacitors are fundamental components of the electronic circuitry commonly found in devices in areas such as analogue to digital conversion, micro-electromechanical systems, medical, automotive and memory applications [40], [73], [143], [144]. Current MIM capacitors generally employ optimised low dielectric constant (*k*) materials (*k*~3.9 - 7) to attain the target electrical properties of high breakdown field and low current leakage. However, device scaling is limited due to the low *k* value of these materials and this presents a significant challenge to the future development of these technologies [145]. Many high *k* materials are under investigation to replace these lower *k* dielectrics to substantially increase the maximum capacitance density and reduce the area associated with the integration of MIM structures. In previously published work [140] hafnium silicate MIM capacitors with excellent electrical properties were obtained, including an electric breakdown field of ~ 7.5 $MVcm^{-1}$, a k value ~ 14 and no hysteresis or dispersion at frequencies of 1 kHz – 100 kHz. These MIM capacitors were produced on a range of electrode materials with no apparent significant variation in the electrical properties. In this chapter we aimed to investigate the dielectric material by using a bottom platinum electrode which due to its controlled chemical nature (does not easily form a native oxide) would potentially allow clearer insight into the intrinsic properties of the dielectric material.

4.2 Materials and Methods

The dielectric films, in both chapter's 2 and 3 and this chapter, were grown by atomic layer deposition at 250˚C. The metal sources, Tetrakis(dimethylamino) hafnium and Tetrakis(dimethylamino) silane were pulsed simultaneously as the first half cycle with a remote oxygen plasma (300 W) pulse completing the cycle. In this study ~ 50 nm dielectric was deposited simultaneously on to 3 separate samples, sputtered bottom platinum, titanium tungsten and aluminium electrodes with a sputtered titanium adhesion layer (~ 10 nm) between the platinum and the silicon dioxide isolation layer. The top aluminium electrode was deposited by an e-beam process. The reliability results for the platinum and titanium tungsten alloy bottom electrodes will be compared to the previous results for an aluminium bottom electrode in chapter 2, the dielectric was deposited by identical means for that sample. In this previously reported sample the aluminium bottom electrode was sputtered directly on to silicon dioxide and the top aluminium electrode was sputtered on to the dielectric [140]. For both the current and previous samples discussed, devices, defined by lift-off, were 1×10^{-8} m^2.

Capacitance voltage measurements were recorded using an Agilent E4980a LCR meter following open-circuit calibration. Current - voltage measurements were recorded using an Agilent 4156C precision semiconductor parameter analyzer. All electrical measurements were performed at room temperature in a microchamber

probe station Cascade Microtech, model Summit 12971B. Transmission electron microscopy (TEM) specimens for cross section analysis (XTEM) were prepared using the conventional method: gluing face to face small pieces cut from the area of interest using M-bond, followed by mechanical polishing and ion milling in a Gatan PIPS model 691 apparatus. TEM was performed using a Jeol ARM 200F electron microscope, performing TEM imaging, high resolution (HRTEM), scanning transmission electron microscopy-high angle annular dark field (STEM-HAADF) imaging and energy-dispersive x-ray (EDX) line analysis spectroscopy. In addition, Raman spectroscopy employed a Renishaw InVia Reflex microscope, in a backscattering configuration, with an excitation wavelength of 514.5 nm and energy of < 2mW to prevent thermal effects.

4.3 Results and Discussion – Electrical Characterisation and Analysis

It is evident from Figure 4.1 (top) that the change of electrode can strongly influence the nature of the dielectric. Both the TiW and Al samples were grown in the same batch, however, the breakdown voltage of the TiW sample was superior in both polarities when compared to the Al sample. Additionally, there was a noticeable increase in leakage current in both polarities for the Al sample. The general shape of the J-V trace was similar to the TiW sample which may suggest that the same leakage mechanisms are responsible for conduction in the oxides.

However, the Pt sample which was grown separately under the same conditions is distinctly different from the other two samples. The breakdown voltages in both

polarities have greatly reduced in comparison and there is an obvious asymmetry in the J-V traces, Figure 4.1 (bottom). In particular, the positive gate sweep has some interesting features such as practically constant leakage current to ~ 10 V. This is then followed by a rapid increase in leakage current and soft breakdown events leading to hard breakdown. In the negative voltage sweep, we observe a more standard evolution of current with voltage increase followed by hard breakdown. This strongly indicates that different leakage current mechanisms are responsible for the conduction in each polarity. During the positive sweep on the gate electrons are injected from the bottom electrode interface and the properties of this interface appear to inhibit electron transport up to ~ 10 V.

It has also been observed in Figure 4.1 (bottom) for both the Al and TiW samples that there is an increase in leakage current for the in the J-V traces for the positive sweep (solid lines) on the gate compared to the negative sweep (dashed lines). This may possibly be attributed to a native oxide or interface layer on the substrate or perhaps the different work functions of the top and bottom metal electrodes. However, similar behaviour in the J-V traces for the sample in chapter 2 was observed, figure 2.12, where both electrodes were sputtered Al, furthermore, an interface layer was observed on the bottom electrode of that sample by TEM as shown in figure 2.21. Also, the E_{BD} tended to be slightly increased for the negative sweep on the gate compared to the positive sweep.

The C-V sweeps for the Al sample showed negligible hysteresis and dispersion, from 1 kHz to 100 kHz, as shown in Figure 4.2. Furthermore, the minimum capacitance at

1 kHz was C_0 ~ 2.41 fF/um^2, however, this was offset from 0 V by -2 V at 1 kHz. This would indicate the presence of positive charge in the dielectric bulk or at the interfaces and this charge is highly frequency dependent. A k value ~ 13.6 was determined from C_0 at 1 kHz and a nominal thickness of 50 nm (500 ALD cycles) from the capacitance equation below

$$C = \frac{\kappa \varepsilon_0 A}{d} \qquad (1)$$

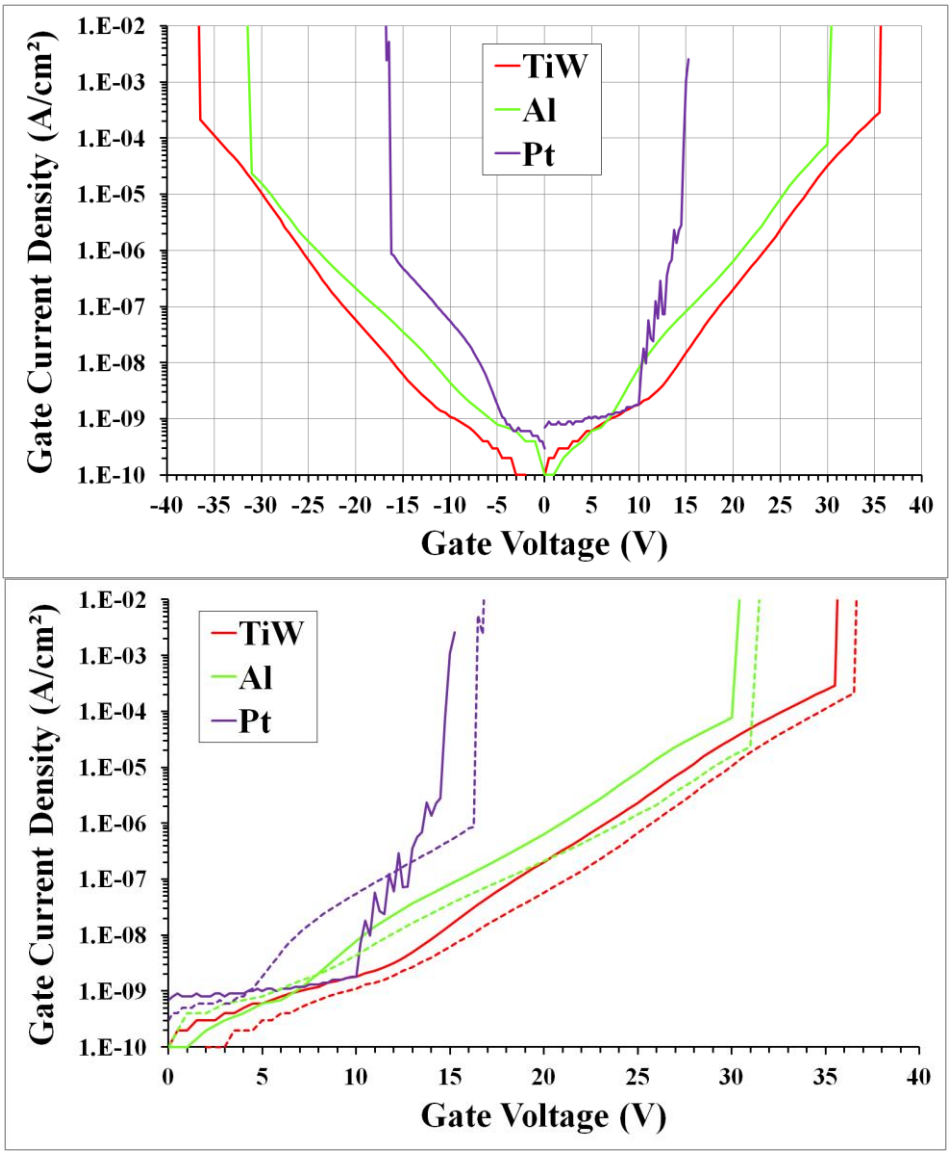

Figure 4.1 (top) J-VG traces for hafnium silicate grown by ALD (500 cycles) on TiW, Al and Pt bottom electrodes. (Bottom) Absolute voltage values for the same data for negative (dashed line) and positive sweep (solid line) leakage current comparison.

where k is the dielectric constant, ε_0 is the permittivity of free space, A is the area of the capacitor and d is the thickness of the dielectric film. The value of k compares

very well with a 120 nm film, k ~ 13.2, grown under the same conditions and the same electrode in chapter 3.

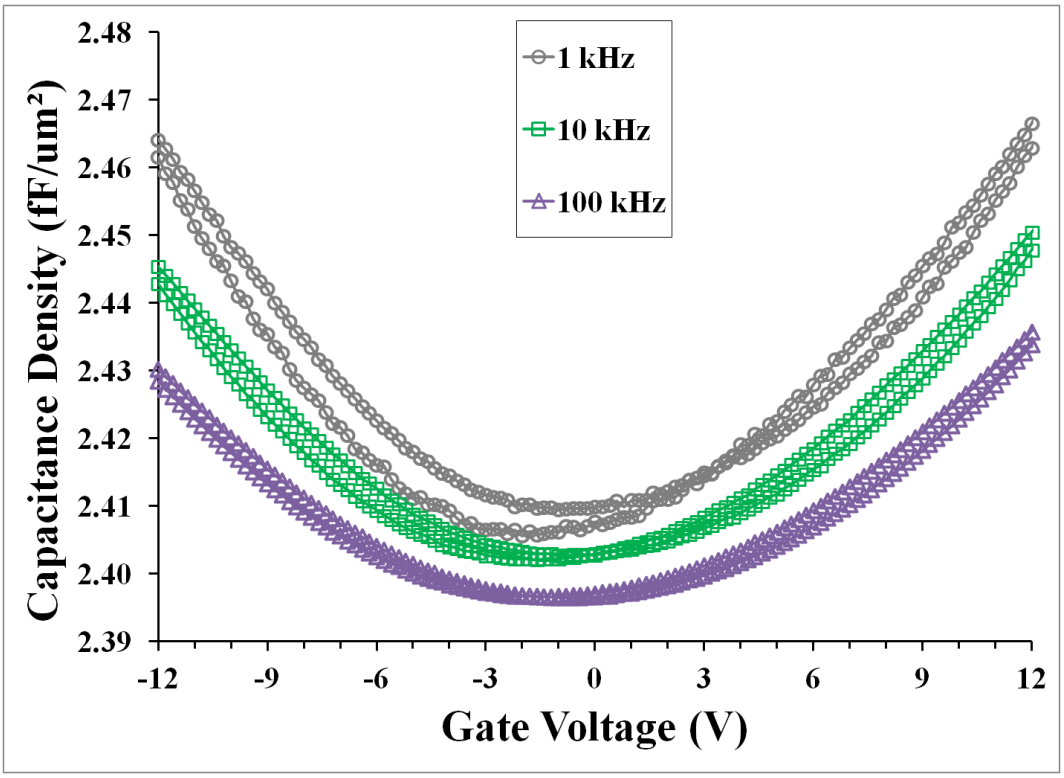

Figure 4.2 CD-VG double sweeps for the Al sample at 1 kHz, 10 kHz and 100 kHz.

In Figure 4.3 the C-V sweeps for the TiW sample showed zero hysteresis and negligible dispersion, from 1 kHz to 100 kHz. Additionally, C_0 ~ 2.43 fF/um^2 at 1 kHz, however, the minimum was offset from 0 V by -1.2 V at 1 kHz and also at 1 MHz (not shown). This would indicate the presence of positive charge in the dielectric bulk or at the interfaces. However, this sample appears to have less positive charge than the Al sample and also shows little frequency dependence up to 1 MHz.

There was some asymmetry in the C-V sweeps probably due to the dissimilar top and bottom electrodes. Again, k ~ 13.7 was determined with a nominal 50 nm thickness. The k value and capacitance density of both Al and TiW samples were very consistent.

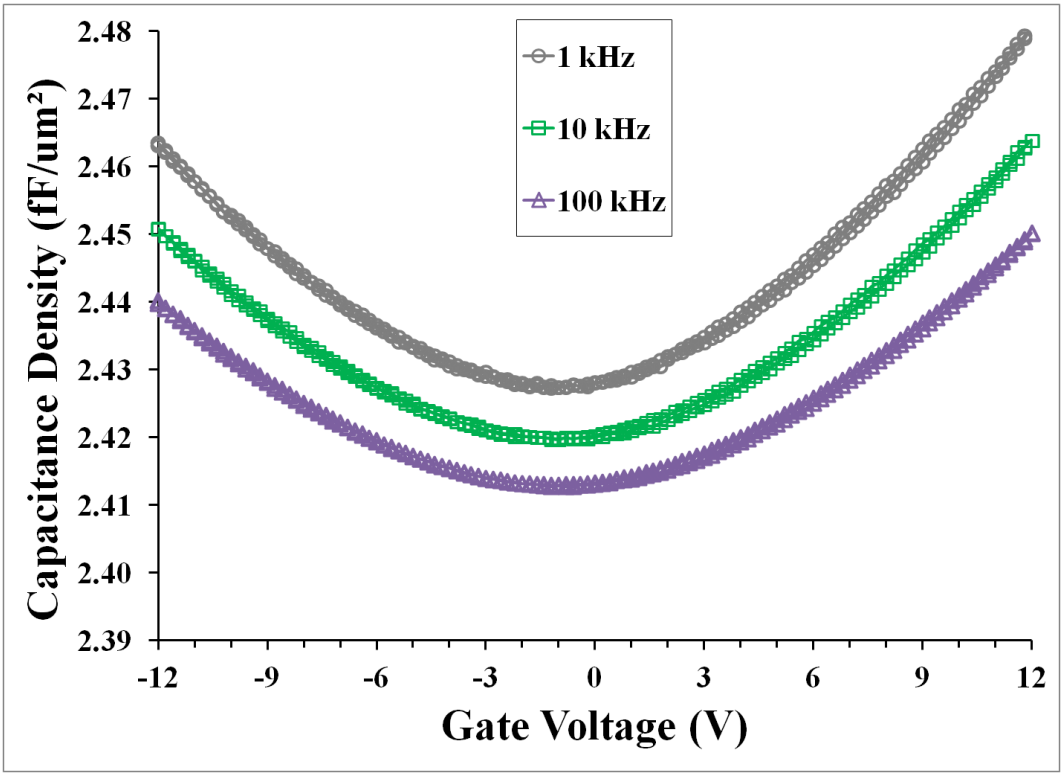

Figure 4.3 CD-VG double sweeps for the TiW sample at 1 kHz, 10 kHz and 100 kHz.

Again, there was zero hysteresis and negligible dispersion from 1 kHz to 100 kHz for the Pt sample in Figure 4.4. However, C_0 ~ 3.31 fF/um^2 at 1 kHz and this was considerably larger than the equivalent figure for both the Al and TiW samples. Once again, there was an offset from 0 V by ~ -1 V at 1 kHz and this value decreased to ~ -

0.8 V at 1 MHz (not shown). There was also some asymmetry in the sweeps for the reason stated previously. A *k* value of ~ 18.7 was determined from a film thickness ~ 50 nm, confirmed by TEM. The *k* value and capacitance density of this film were significantly larger than the Al or TiW sample.

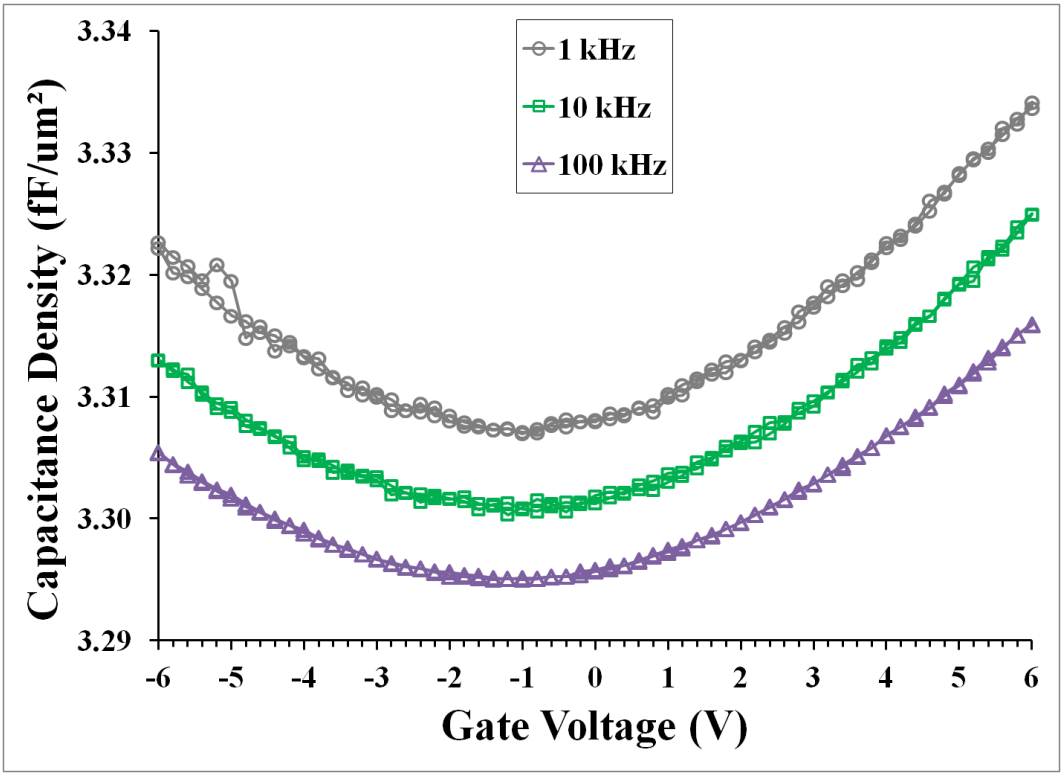

Figure 4.4 CD-VG double sweeps for the Pt sample at 1 kHz, 10 kHz and 100 kHz.

The quality factors (Q) (reciprocal of the dissipation factor) for the Al sample were ~ 700 at 1 kHz, ~ 480 for both 10 kHz and 100 kHz as shown in Figure 4.5. This indicated some losses in the dielectric between 1 kHz and 10 kHz; however, no further losses occurred up to 100 kHz.

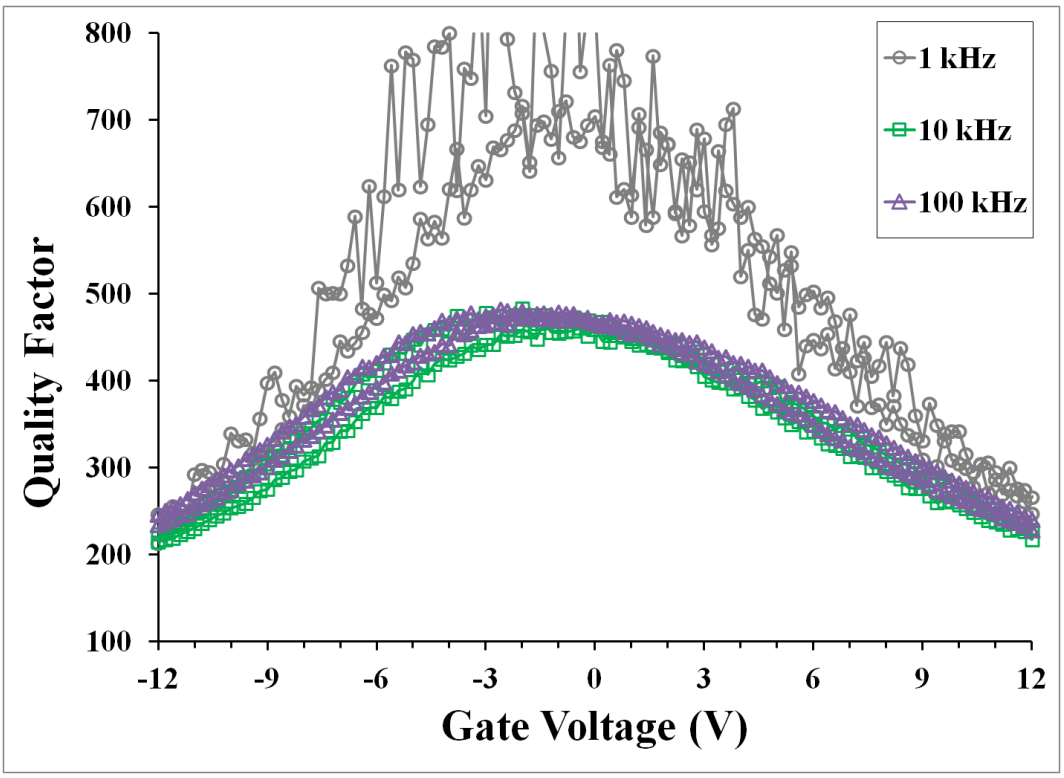

Figure 4.5 Q- VG double sweeps for the Al sample at 1 kHz, 10 kHz and 100 kHz.

The TiW sample had the following Q values, ~ 750 at 1 kHz, ~ 450 for 10 kHz and ~ 240 for 100 kHz, Figure 4.6. There was an increase in frequency related dielectric losses in the TiW sample compared to the Al sample. This may be related to native oxide growth at the dielectric / bottom metal electrode interfaces.

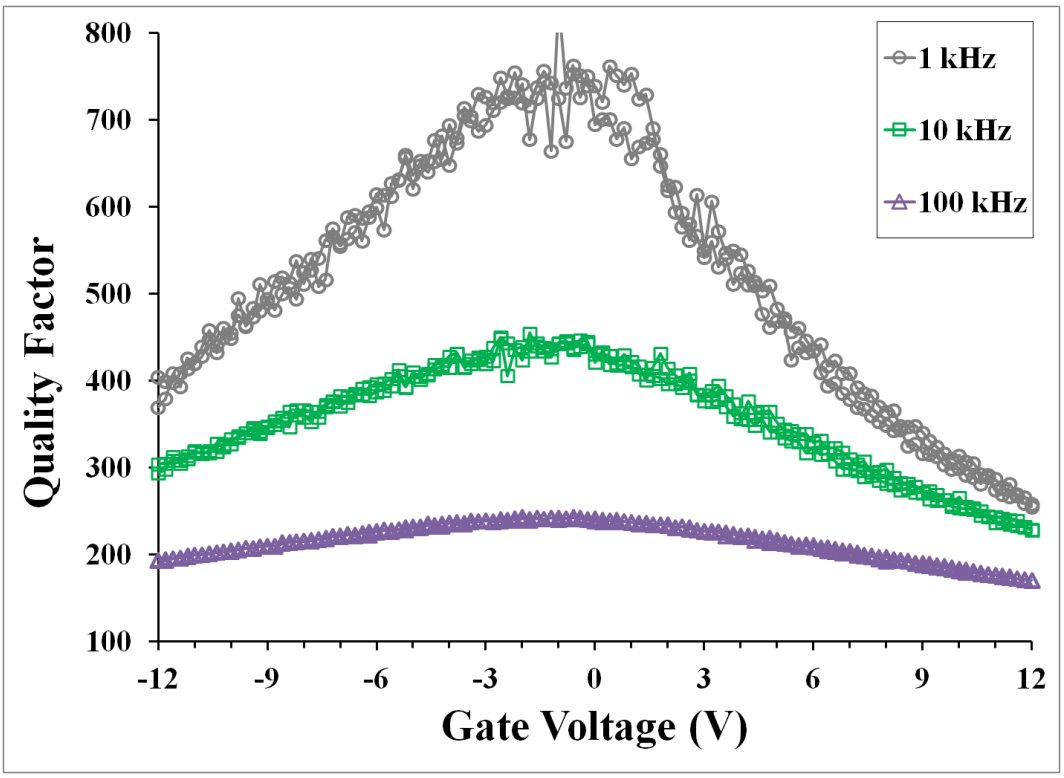

Figure 4.6 Q- VG double sweeps for the TiW sample at 1 kHz, 10 kHz and 100 kHz.

In Figure 4.7, the Q values for the Pt sample were, ~ 1000 at 1 kHz, ~ 360 for 10 kHz and ~ 60 for 100 kHz. This dielectric film had very encouraging Q value at 1 kHz, although, there were very large losses with increasing frequency and this sample compared poorly to both of the previous samples.

The non-linear change in capacitance with voltage is important for certain applications such as RF or AMS and it tends to increase significantly with decreasing film thickness. Capacitance-voltage linearity can be analysed by fitting the change in capacitance normalised to the capacitance minimum ($\Delta C/C_0$) versus voltage with a second order polynomial [35].

$$C(V) = C_0(\alpha V^2 + \beta V + 1) \qquad (2)$$

where α and β are quadratic and linear voltage coefficients of capacitance respectively. The value of α according to the ITRS roadmap must be < 100 ppm/V^2 for RF or AMS applications and β can be minimised by circuit design [81]. The fit to (2) for the Al sample data at 1 MHz in Figure 4.8 resulted in α ~ 81 ppm/V^2, also, the value determined for the TiW data in Figure 4.9 was α ~ 77 ppm/V^2. Both of these values are < 100 ppm/V^2 and meet the ITRS criteria.

However, the value in Figure 4.10 for the Pt sample was α ~ 108 ppm/V^2, and this was slightly above the ITRS roadmap acceptable limit.

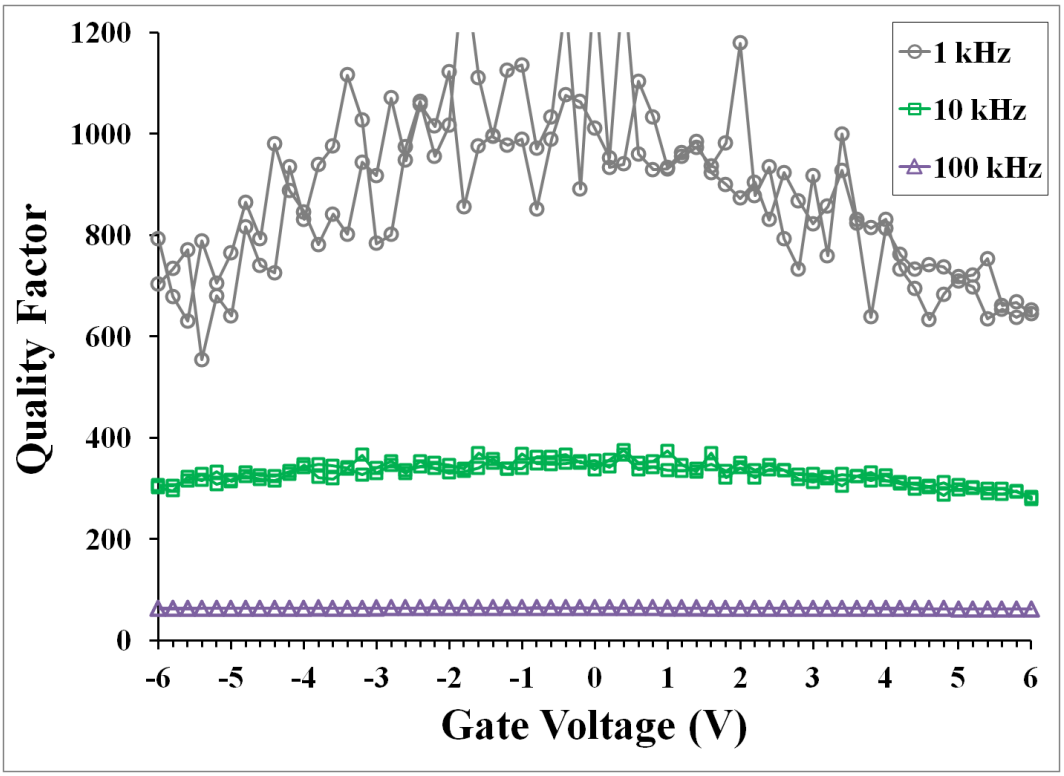

Figure 4.7 Q- VG double sweeps for the Pt sample at 1 kHz, 10 kHz and 100 kHz.

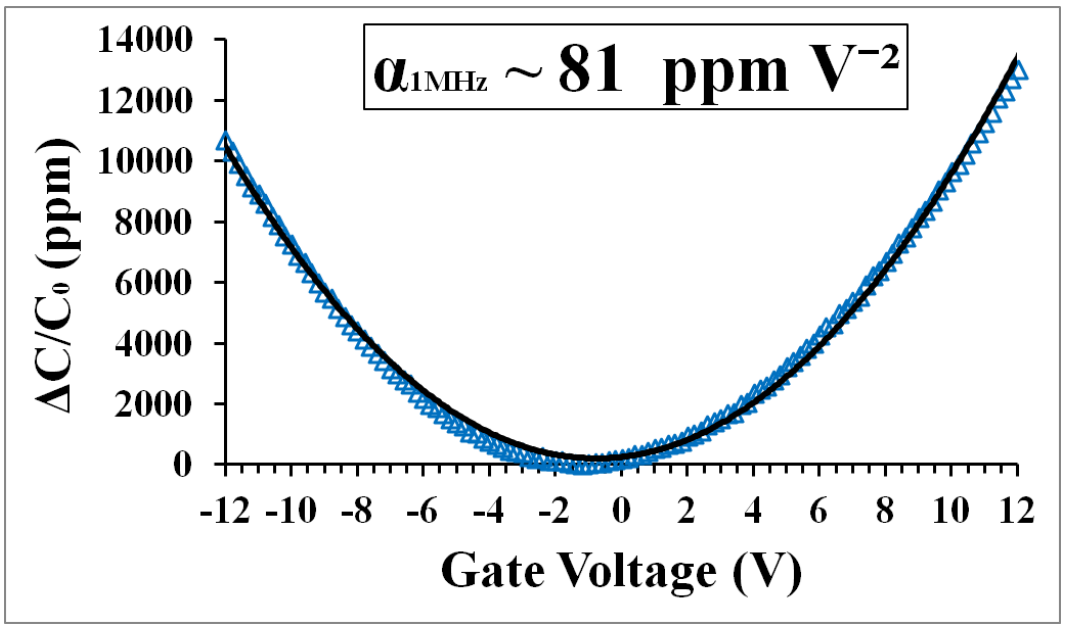

Figure 4.8 Quadratic voltage coefficient of capacitance (α) extracted from polynomial fit to normalised capacitance at 1 MHz for the Al sample.

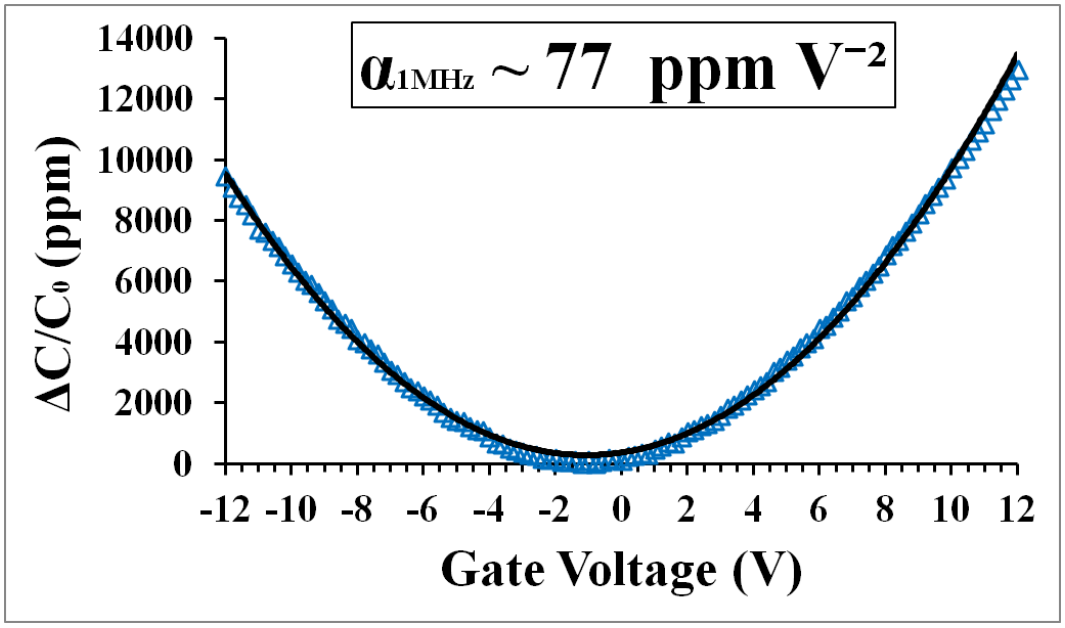

Figure 4.9 Quadratic voltage coefficient of capacitance (α) extracted from polynomial fit to normalised capacitance at 1 MHz for the TiW sample.

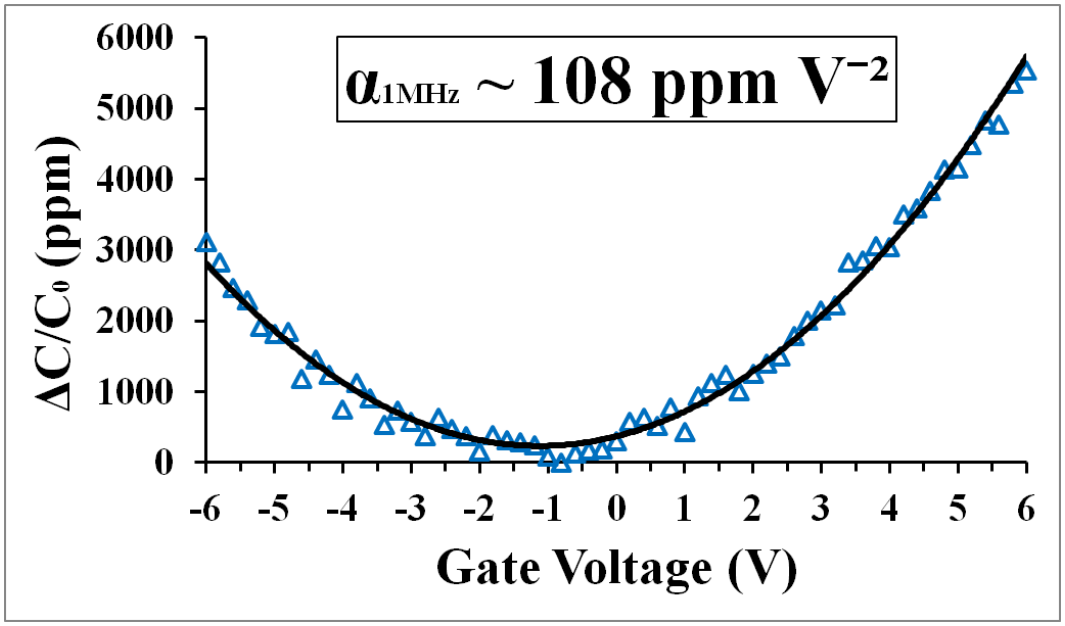

Figure 4.10 Quadratic voltage coefficient of capacitance (α) extracted from polynomial fit to normalised capacitance at 1 MHz for the Pt sample.

4.3.1 TiW Reliability Characterisation and Analysis

The reliability of the TiW sample was investigated and 74 CVS measurements were taken at five stress voltages according to the time dependent dielectric breakdown (TDDB) methodology. This time to breakdown (t_{BD}) data was analysed using a two parameter Weibull. From this analysis of the five distributions the shape parameter (β) and the scale factor (n), which is normally determined at 63% cumulative failure (n_{63}), were estimated by maximum likelihood algorithm fitting.

The average value of β for the five breakdown distributions was ~ 3.6. This compares reasonably well with the value for the 120 nm sample that was determined previously

in chapter 2, $\beta \sim 3.4$. However, there was a larger spread in the β values for the TiW sample, 4.7 to 1.9, compared to the 120 nm sample on an Al substrate in chapter 1, 3.0 to 3.4.

The maximum operating voltage of the control sample to give a 10 years lifetime (0.1 cm^2 & 0.01 % scaled) was ~ 17 V as shown in Figure 4.11. Furthermore, the field acceleration parameter as determined for nominal film thickness (50 nm) from the Linear E-model fit to the n_{63} values was $\gamma \sim 6.3$ cm/MV, Figure 4.11 (inset). The 10 year lifetime is ~ 47% of the breakdown voltage which compares well to the comparable figure, ~ 50%, for the 120 nm $HfSiO_x$ dielectric grown on an Al substrate in chapter 3. Also, $\gamma \sim 6.3$ cm/MV is similar to the value determined for the sample in chapter 3, $\gamma \sim 6.0$ cm/MV.

The extracted activation energy of bond breakage ΔH_0^* value calculated from was ~ 1.20 eV and the effective dipole moment for bond breakage was ~ 16.0 eÅ. Both of these values were reasonably consistent with previous values ($\Delta H_0^* \sim 1.3$eV and a ~ 15.2 eÅ) for the sample in chapter 3, 120 nm hafnium silicate with sputtered Al electrodes.

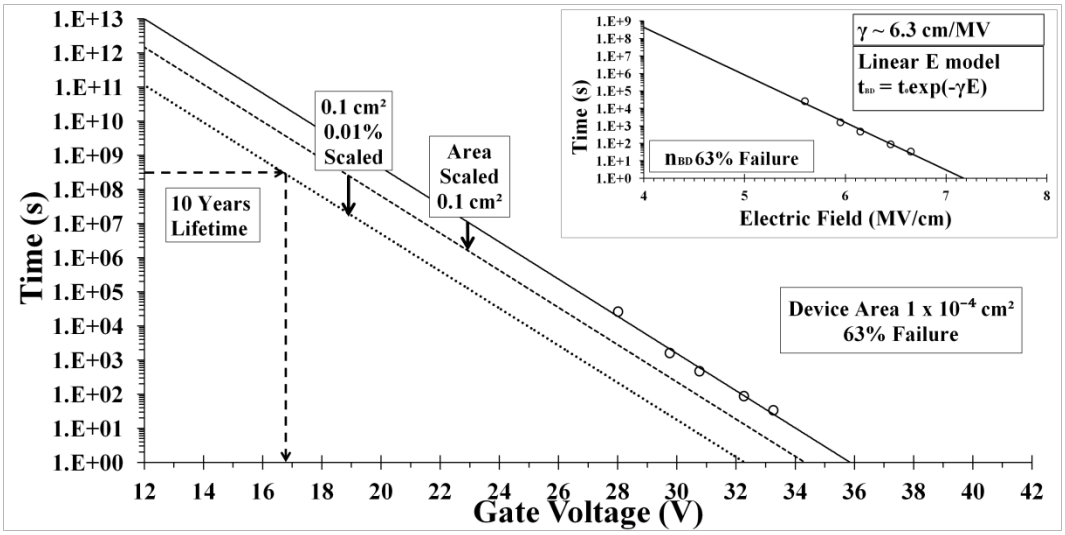

Figure 4.11 TDDB lifetime extrapolation of TiW sample. A linear E-model extrapolation of the n63 data was scaled to 0.1 cm2 and 0.01% failure, a maximum gate voltage of ~ 17 V was extrapolated to a guarantee a lifetime value of 10 years without hard breakdown and determination of the associated field acceleration parameter γ (inset).

4.3.2 Pt Reliability Characterisation and Analysis

The reliability was of the Pt sample was investigated and the maximum operating voltage of the control sample to give a 10 years lifetime (0.1 cm^2 & 0.01 % scaled) was ~ 6.5 V as shown in Figure 4.12. The field acceleration parameter as determined for nominal film thickness (50 nm) from the Linear E-model fit (3) to the n_{63} values was $\gamma \sim 22.2$ cm/MV, Figure 4.12 (inset).

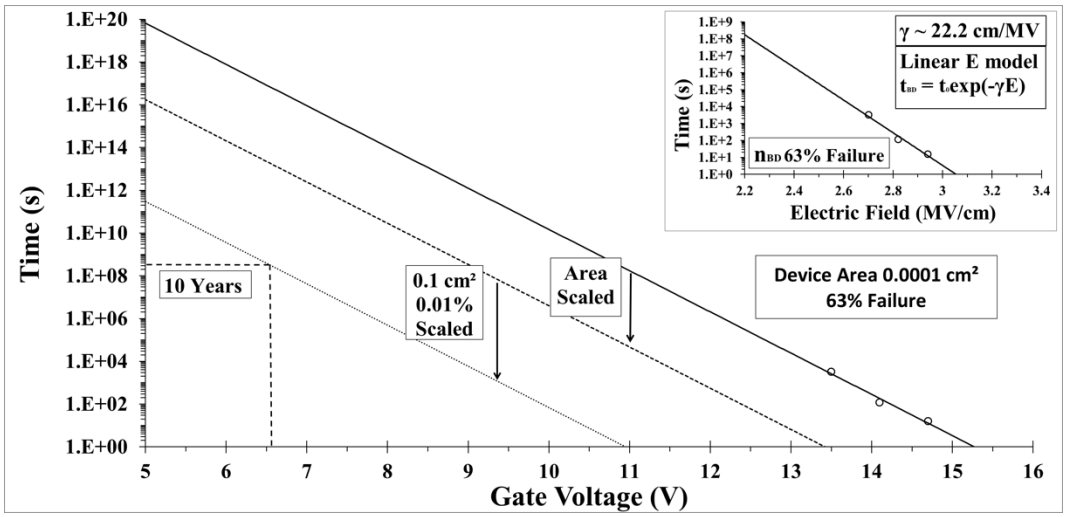

Figure 4.12 TDDB lifetime extrapolation of Pt sample. A linear E-model extrapolation of the n63 data was scaled to 0.1 cm2 and 0.01% failure, a maximum gate voltage of ~ 6.5 V was extrapolated to a guarantee a lifetime value of 10 years without hard breakdown and determination of the associated field acceleration parameter γ (inset).

The results showed a dramatic decrease in maximum operational voltage coupled with a large increase in the associated field acceleration parameter when compared to the results for the TiW and Al samples stated previously.

Furthermore, on analysis of the CVS data a large amount of dispersion is evident as shown in Figure 4.13 (top) and on closer examination of the individual measurements, as shown in Figure 4.13 (bottom), soft breakdown events are observed prior to hard breakdown. Also, the leakage current was generally not observed to decrease with time as observed with the Al sample. Consequently, the shape of the Pt I-t traces are very different to the Al sample and with the addition of soft breakdown events this would imply that different breakdown mechanisms may be responsible for failure in this sample.

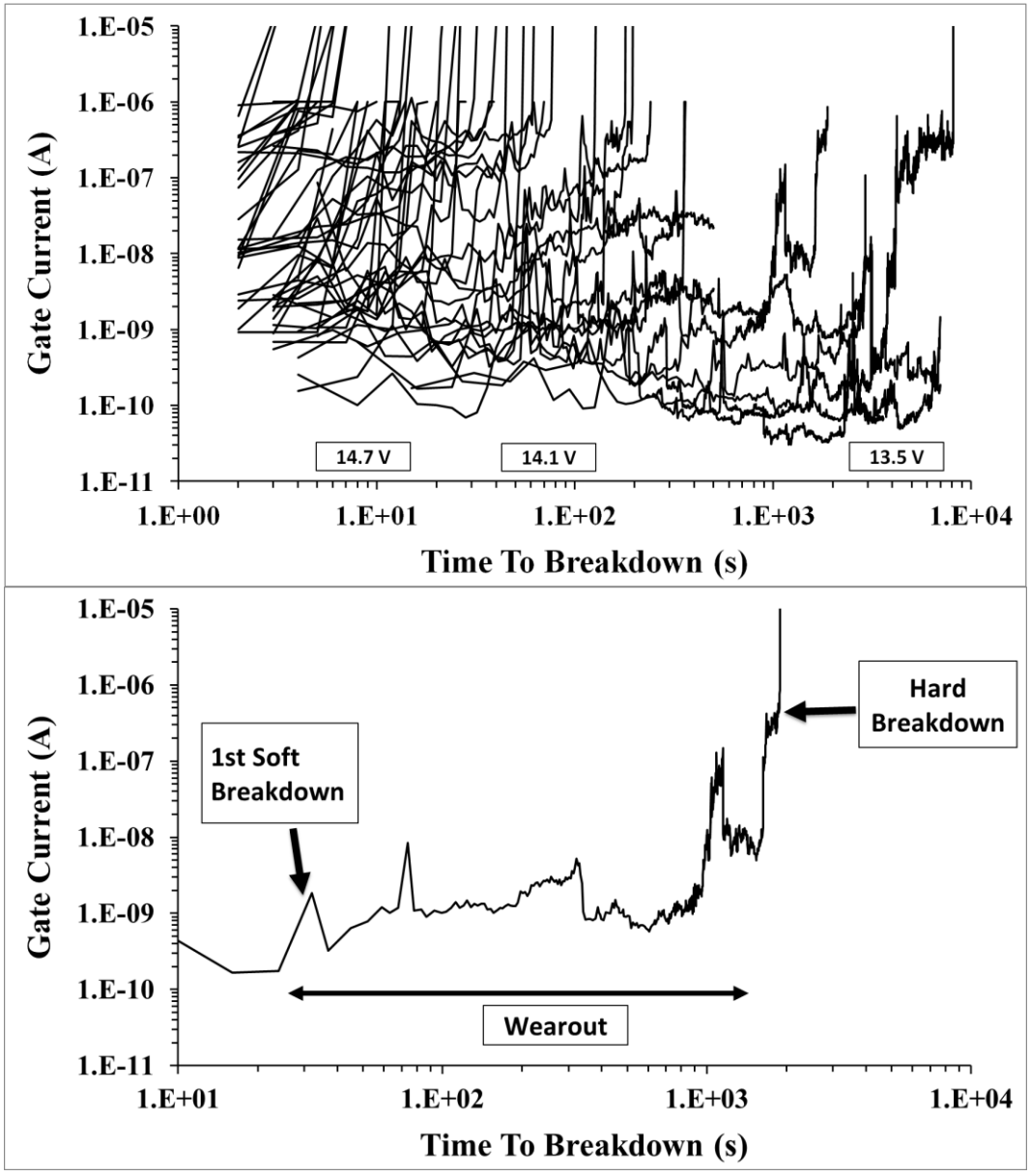

Figure 4.13 I-t traces for CVS measurements at 14.7, 14.1 and 13.5 V on the Pt sample (top) and an individual I-t trace at 13.5 V (bottom). All measurements were performed with a positive CVS on the gate.

Again, a two parameter Weibull analysis was performed on the t_{BD} data for the Pt sample as shown in Figure 4.14. The average value for β from the three distributions

was ~ 0.84 (0.99 – 14.7 V, 0.76 – 14.1 V and 0.77 – 13.5 V) and this compares very poorly with the previous results for TiW and Al. As β represents failure rate behaviour then a value of < 1 implies that the failure rate is decreasing with time and this may point to extrinsic influences on the failure distribution rather than purely TDDB. Furthermore, the evidence indicates that the reliability properties of the dielectric on the Pt substrate have degraded substantially compared to the TiW and Al substrates.

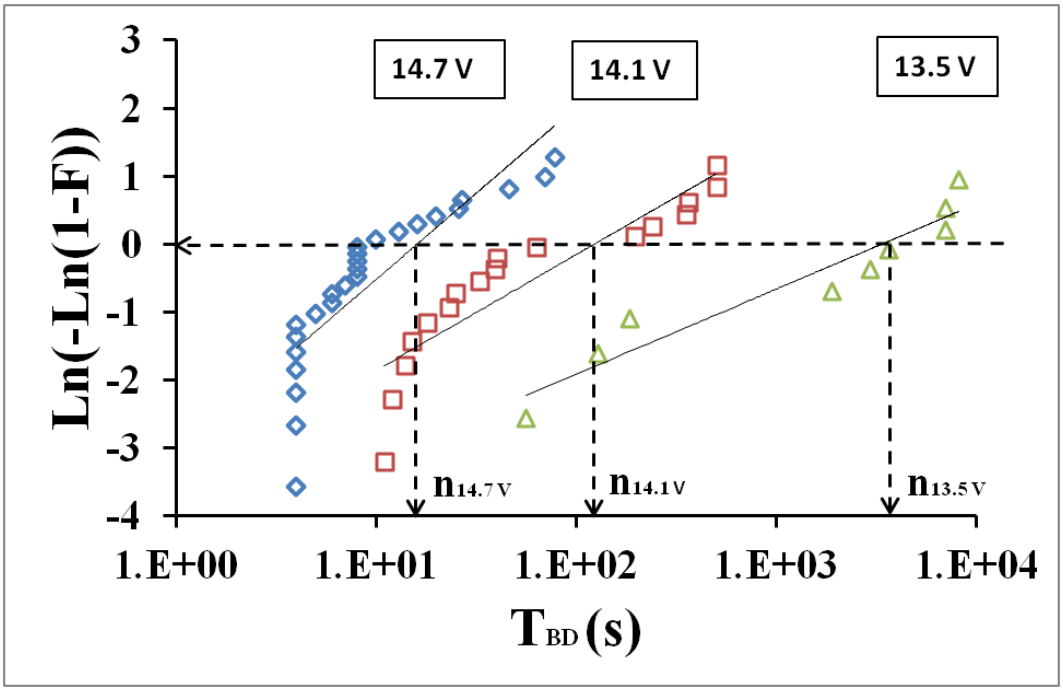

Figure 4.14 Weibull distributions for breakdown time results from CVS with positive bias on the gate for Pt sample. The median value of β ~ 0.84 and the n63 values for each voltage are indicated on the plot.

4.3.3 Pt Physical Characterisation and Analysis

Physical analysis was performed on the Pt sample to further investigate this degradation of the electrical properties. This involved a high resolution transmission electron microscope micrograph (HRTEM) analysis on the sample to investigate the bulk material structure and interfaces. A representative portion of the sample was removed prior to top metallisation and this was for used for the TEM lamella extraction.

A cross section of the Pt sample lamella is shown in Figure 4.15 and the material system stack can be clearly observed.

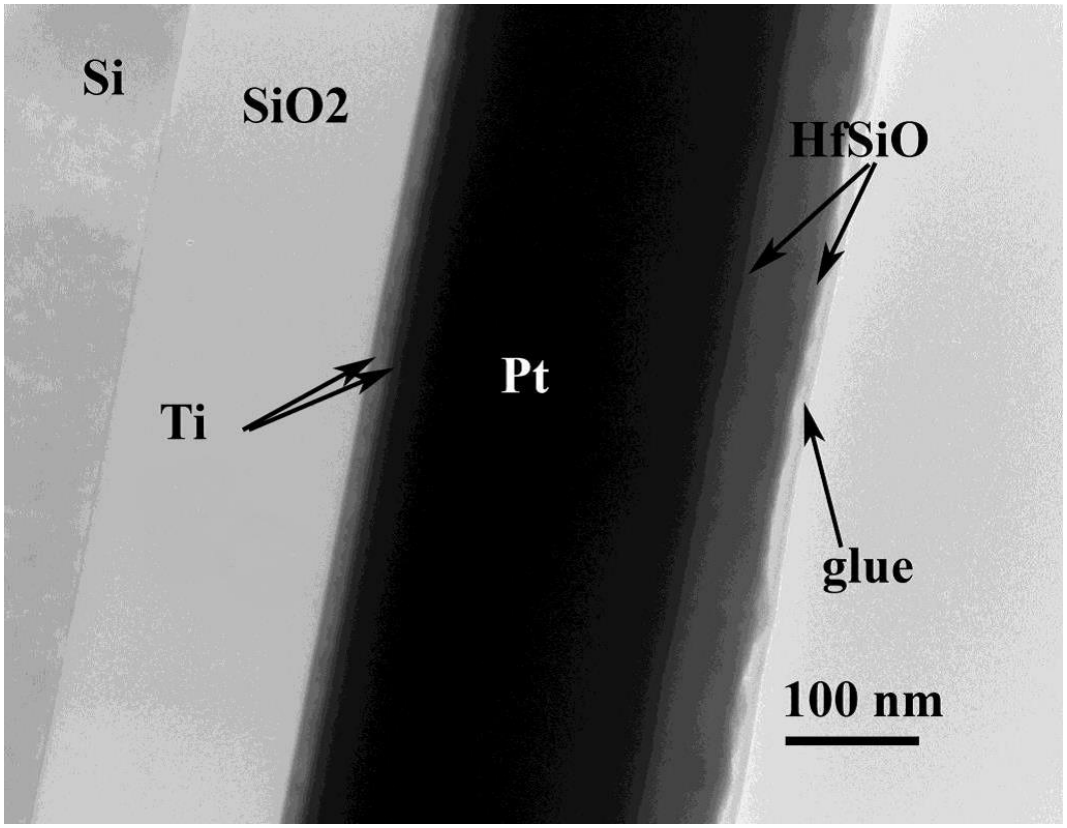

Figure 4.15 Cross section TEM of the Pt sample showing the Si substrate, SiO2 insulation layer, a titanium adhesion layer, platinum bottom electrode, the dielectric layer labelled as HfSiO (~ 50 nm) and a glue layer (for TEM lamella preparation).

In Figure 4.16, the ALD hafnium silicate layer is shown to be polycrystalline in the HRTEM cross section. Furthermore, Raman spectroscopy indicates that the film is monoclinic hafnium oxide, no evidence of hafnium silicates is observed within the detectable limits of this measurement.

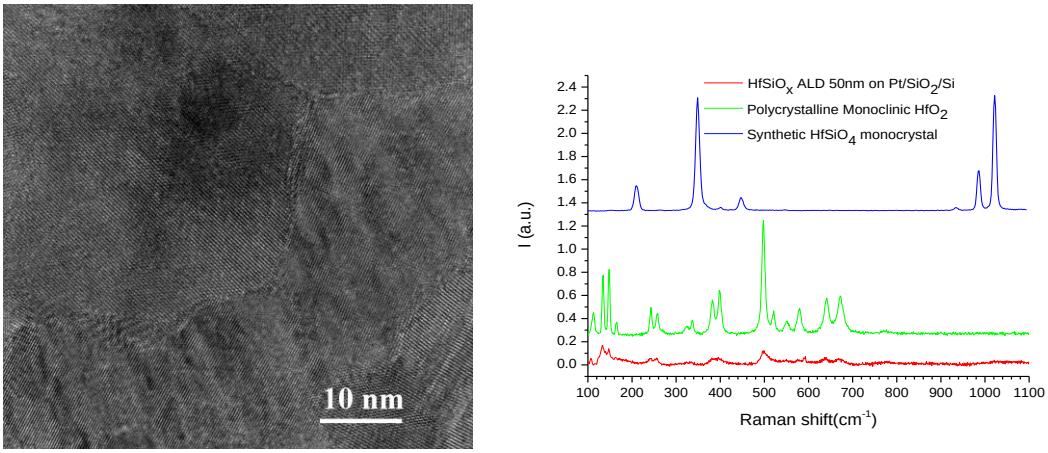

Figure 4.16 HRTEM (left) and Raman spectrum (right) of the ~ 50 nm dielectric on a platinum (bottom) electrode. Both The TEM and Raman spectrum indicate that the structure is polycrystalline monoclinic hafnium oxide.

Further HRTEM analysis concentrated on the Pt / polycrystalline dielectric interface. The crystalline structure of the dielectric layer was observed to "template" from Pt layer lattice as shown in Figure 4.17.

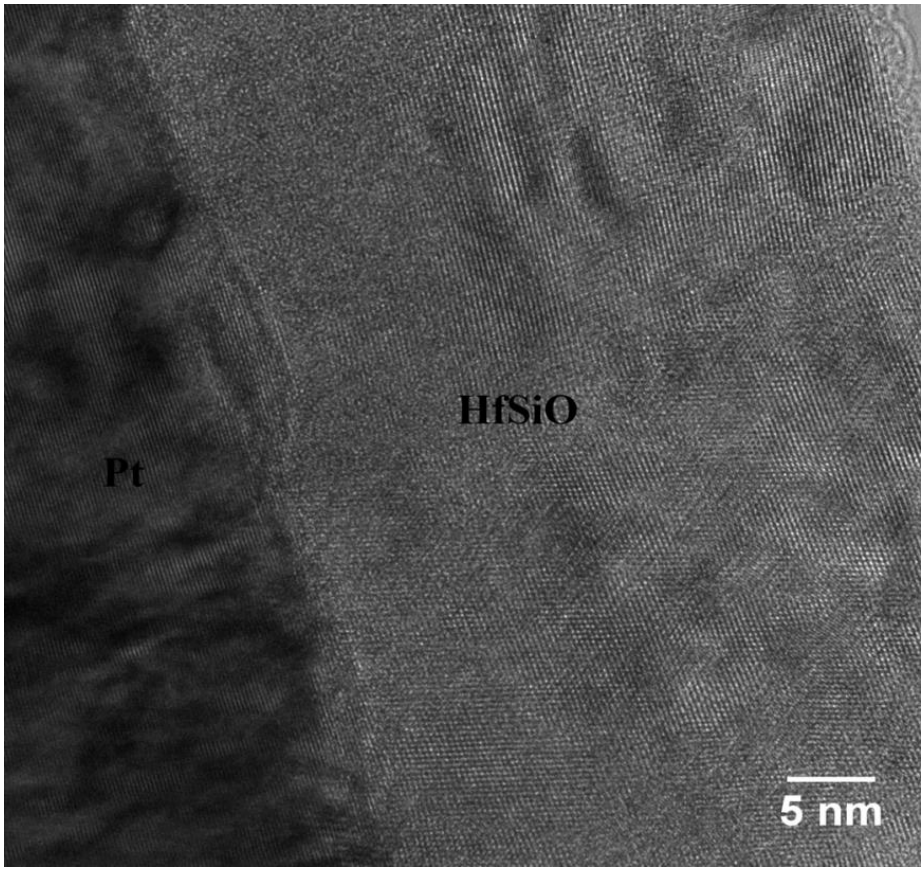

Figure 4.17 HRTEM of the Pt / polycrystalline dielectric interface from the 50 nm dielectric film with platinum (bottom) electrode.

Additional analysis resulted in the identification of the origin of the "templating", at the Pt / Ti interface the Pt layer was observed to "template" from the Ti layer lattice as shown in Figure 4.18. Hence, the nucleation and growth of the polycrystalline dielectric layer may have been indirectly influenced by the Ti adhesion layer.

The lattice spacing was observed to change at some grain boundaries within the polycrystalline dielectric bulk as shown in Figure 4.19.

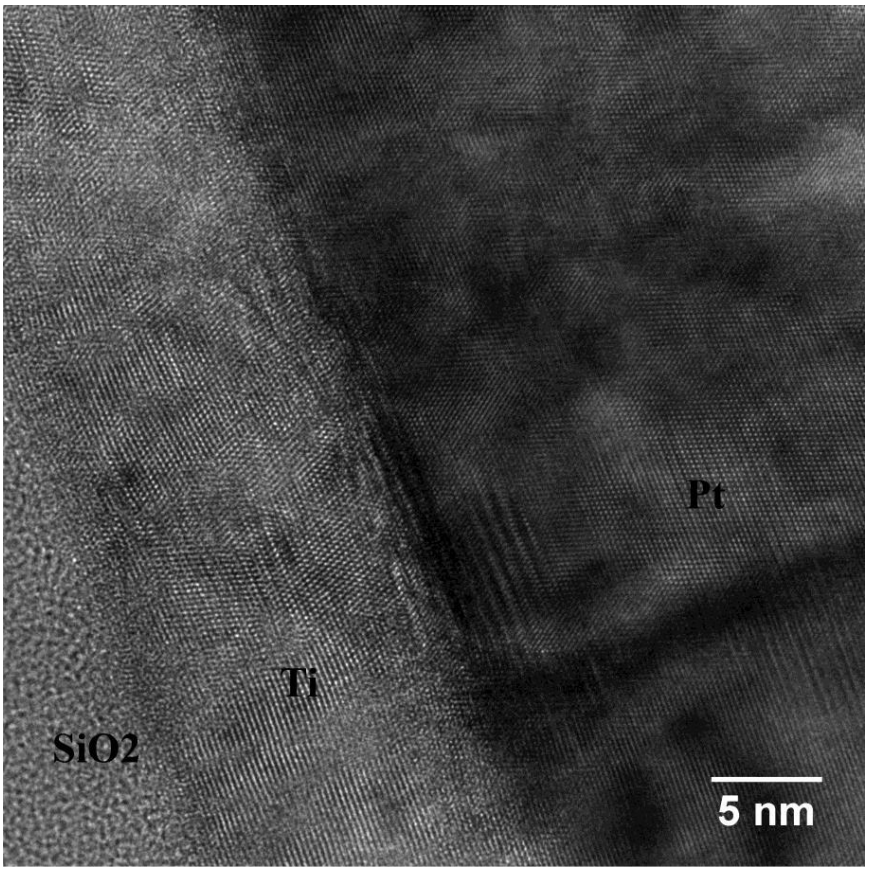

Figure 4.18 HRTEM of the Ti / Pt interface from the 50 nm polycrystalline dielectric film with platinum (bottom) electrode.

As no evidence of silicon containing material was observed in Raman and HRTEM, further analysis techniques were required to confirm the materials composition. An EDX line scan was employed across the lamella, Figure 4.20, in which the elements hafnium, silicon and oxygen are clearly resolved.

The inclusion of silicon was further investigated using Scanning transmission electron microscopy-high angle annular dark field (STEM-HAADF) as illustrated in Figure 4.21, from which it can be seen that low atomic number nanoparticles are

present. These particles are believed to be silicon containing, most likely silica, and are predominately located at the hafnium oxide grain boundaries. Furthermore, these particles appear to be more frequent towards the bottom electrode.

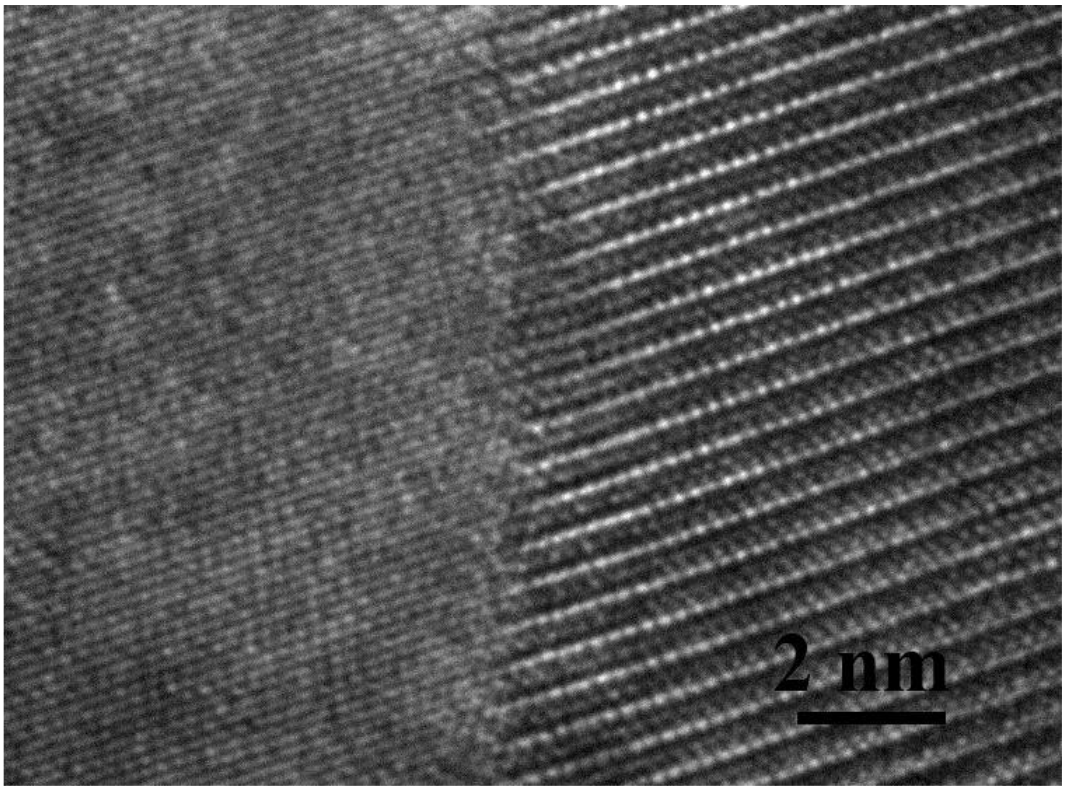

Figure 4.19 HRTEM of a grain boundary within the polycrystalline dielectric bulk of the 50 nm dielectric film with platinum (bottom) electrode.

The structural analysis implies that there may be silicon containing nanoparticles in the dielectric film on platinum. The nature of these particles would have an influence on the resultant electrical properties, if the nanoparticles were silicon, these would be electron trapping sites, and the MIM capacitor would have very high hysteresis, the

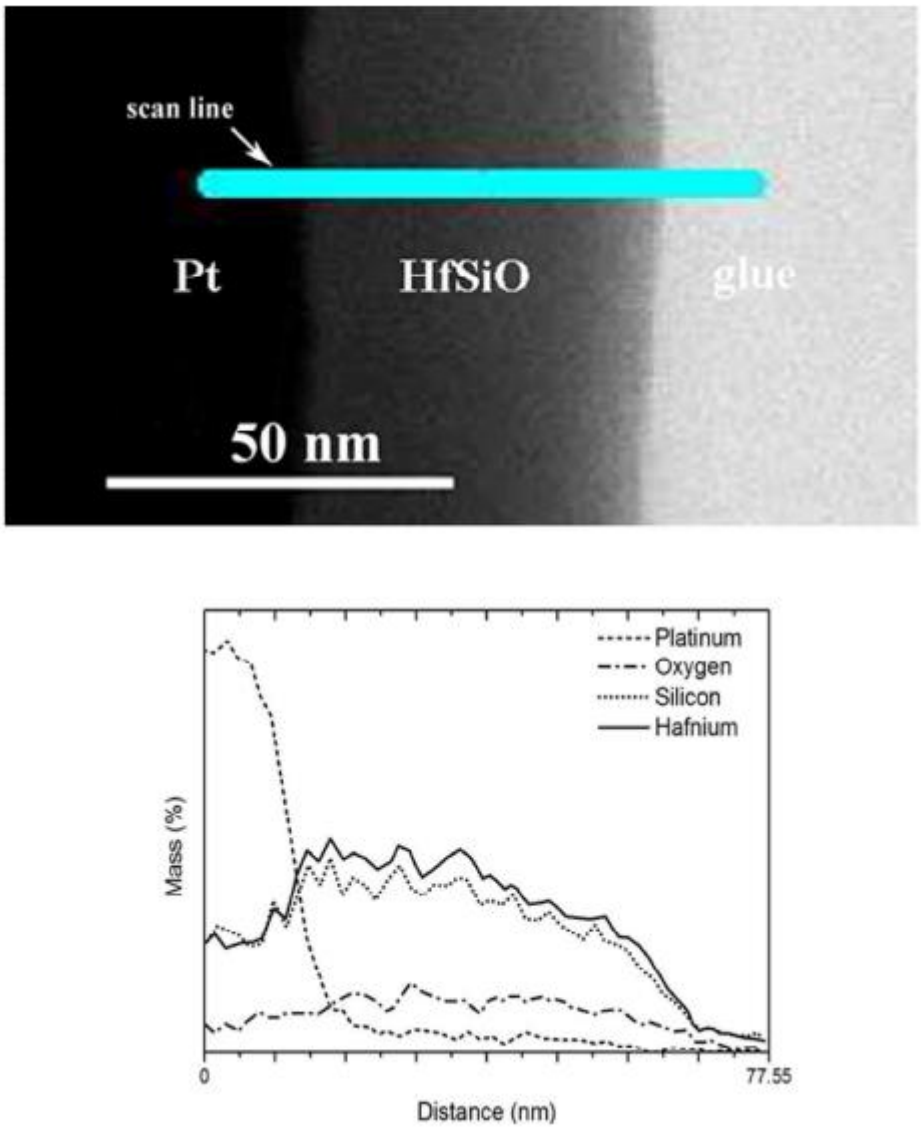

Figure 4.20 EDX line scan across the 50 nm dielectric on platinum lamella. Hafnium, silicon and oxygen can be seen throughout the dielectric layer.

fact that no hysteresis was observed in Figure 4.4 indicates they are oxidised silicon. Furthermore, as can be seen in Figure 4.1 the leakage current density at low electric field is significantly lower than would be expected for monoclinic hafnia. One hypothesis for this would be that if the particles are silica and primarily located

towards the platinum electrode, a positive bias on the gate will inject electrons from the platinum, which could become trapped in the nanoparticles or the immediate surroundings. This would set up an opposing charge to impede further electron injection and lead to a reduced leakage current density. However, when this section of the dielectric or nanoparticle breaks down, this would lead to an increase in electric field across the remaining dielectric thickness and that may cause rapid electrical breakdown. Rapid increase in leakage current density is observed at a threshold electric field but we currently have no additional evidence to support this theory. In the negative bias this effect is less obvious this may be due to the lower density of silica particles towards the gate electrode.

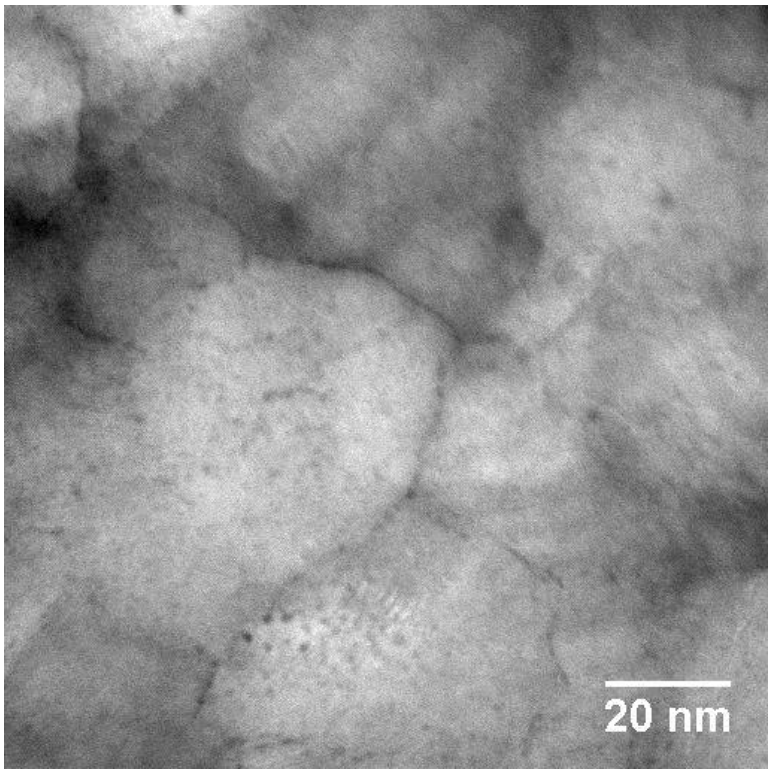

Figure 4.21 STEM-HAADF image of the polycrystalline 50 nm dielectric on platinum sample. The presence of nanoparticles is apparent as dark spots predominately clustered at HfO2 grain boundaries.

4.4 Conclusions

We have observed that the nature of the substrate can have a dramatic effect on the structural and electrical properties of mixed metal dielectrics. Changing the metal substrate in the hafnium silicate growth system can cause a transition from amorphous growth to segregated silica particles within a crystalline hafnia structure. The change in growth mode results in decreased breakdown field but maintains a minimal level of hysteresis in the capacitance voltage characteristics. Furthermore, the reliability was affected with a large decrease in operational voltage for a standard scaled 10 year lifetime. The electrical and reliability characteristics of the TiW sample were determined to be in good agreement to the previous work performed on the Al sample.

5. Summary and Future Work

5.1 Summary

This work investigated the electrical properties, intrinsic reliability and nucleation of a $HfSiO_x$ material system which may be a promising substitute for low-*k* dielectrics in MIM capacitors. This material system was grown by PEALD on various metal substrates and fabricated in to MIM capacitor structures with an aluminium top electrode. The important results are summarised below.

- A study to determine the conduction mechanism for a ~ 120 nm $HfSiO_x$ MIM capacitor sample with sputtered Al electrodes found that Poole-Frenkel emission was a good candidate for the dominant conduction mechanism for electron injection from the gate. However, it could not successfully describe the electron injection from the substrate and this may be attributed to an interlayer, possibly Al_2O_3, at the substrate interface.
- A TDDB reliability study was performed on the ~ 120 nm $HfSiO_x$ MIM capacitor sample and the data was analysed according to the Linear Field Model with Weibull statistics. The maximum operational voltage with a lifetime of 10 years area and percentile scaled (to 0.1 cm^2 0.01%) was determined as 49 V for this ~ 120 nm film. Furthermore, the shape parameter, β = 3.4, was considerably above 1, and the field acceleration factor (~ 6.0 cm/MV), activation energy for bond breakage (ΔH_0^* value ~ 1.3eV) and a ~ 15.2 eÅ were also determined.

- Further samples of the ~ 120 nm $HfSiO_x$ MIM capacitor with sputtered Al electrodes were irradiated with total radiation dosages of 16 krad(Si) and 78 krad(Si) which were equivalent to shielded and unshielded total dosages for LEO satellites respectfully. The 16 krad(Si) sample's maximum operational voltage for 20 year lifetime was area and percentile scaled (to 0.1 cm^2 0.01%) and determined to be 48 V. In general, the properties of this 16 krad(Si) sample compared favourably with the control sample and it was concluded that this level of total radiation dosage (16 krad(Si)) does not impact the CD, EBD or reliability of this material.
- The 78 krad(Si) sample's maximum operational voltage for 20 year lifetime was area and percentile scaled (to 0.1 cm^2 0.01%) and determined to be 44 V. This higher total radiation dosage had a slight effect on the reliability of this sample whereby a reduction of ~ 8% was observed in the 20 year lifetime maximum operational voltage. However, this value is still considerably above most operational ranges for analogue applications. The average shape parameter $\beta \sim 3.2$ was consistent with the control sample, however, there was more spread in the β values which is not obvious from the presented average.
- Alternative substrates, TiW and Pt, were investigated for the $HfSiO_x$ material system and these samples were subsequently fabricated in to MIM capacitors with an Al top electrode. The electrical properties and reliability of the TiW sample broadly agreed with the Al substrate control

sample. However, changing the substrate to Pt resulted in a transition of the hafnium silicate material system from amorphous growth to segregated silica particles within a crystalline hafnia structure. This change in growth mode resulted in a considerable decrease in both breakdown field and operational voltage for a standard scaled 10 year lifetime. The instigator of this phase change was determined to be the Ti adhesion layer under the Pt layer and this was found to template both the Pt layer and $HfSiO_x$ material system.

- The nucleation of PEALD of the HfSiOx material system was investigated by in-situ spectroscopic ellipsometry. Results suggest that it may be strongly influenced by substrate choice and the reactivity of the metal precursors. Evidence that supports the retardation of material growth by the TDMAS precursor was observed.

5.2 Future Work

There are several areas for future investigation arising out of this work as outlined below.

- A study of the HfSiOx material system as a gate dielectric for GaN MOSHEMT technology would be highly desirable to reduce gate leakage current and reduce overall feature size.
- Investigation of the growth of the HfSiOx material system on a conducting hafnon lattice matched substrate to determine the ALD parameters that may result in a fully crystalline hafnon dielectric. The

properties of hafnon have been simulated and show a considerable improvement over non 1:1 ratio hafnium silicates.

- Further study of the ALD process to optimise the electrical properties and reliability of the HfSiOx material system on various substrates that are relevant to future space technology. Additionally, further radiation hardness testing of these films and developing an understanding of the radiation – dielectric interaction.

6. References

[1] A. Farcy, J.-F. Carpentier, M. Thomas, J. Torres, and P. Ancey, 'Integration of high-performance RF passive modules (MIM capacitors and inductors) in advanced BEOL', *Microelectron. Eng.*, vol. 85, no. 10, pp. 1940–1946, 2008.

[2] Y. Neuvo, 'Cellular phones as embedded systems', in *Solid-State Circuits Conference, 2004. Digest of Technical Papers. ISSCC. 2004 IEEE International*, 2004, pp. 32–37.

[3] H. Iwai, 'CMOS technology-year 2010 and beyond', *IEEE J. Solid-State Circuits*, vol. 34, no. 3, pp. 357–366, 1999.

[4] W. Krenik, D. D. Buss, and P. Rickert, 'Cellular handset integration-SIP versus SOC', *IEEE J. Solid-State Circuits*, vol. 40, no. 9, pp. 1839–1846, 2005.

[5] J. Mitola, 'The software radio architecture', *IEEE Commun. Mag.*, vol. 33, no. 5, pp. 26–38, 1995.

[6] W. H. W. Tuttlebee, 'Advances in software-defined radio', *IEE Electron. Syst. Softw.*, vol. 1, no. 1, pp. 26–31, 2003.

[7] B. Razavi, 'CMOS technology characterization for analog and RF design', *IEEE J. Solid-State Circuits*, vol. 34, no. 3, pp. 268–276, 1999.

[8] A. A. Abidi, 'RF-CMOS comes of age', *IEICE Trans. Electron.*, vol. 87, no. 6, pp. 840–853, 2004.

[9] J. G. Atallah and M. Ismail, 'Future 4G front-ends enabling smooth vertical handovers', *IEEE Circuits Devices Mag.*, vol. 22, no. 1, pp. 6–15, 2006.

[10] B. Razavi, *RF microelectronics*, vol. 2. Prentice Hall New Jersey, 1998.

[11] T. H. Lee, *The design of CMOS radio-frequency integrated circuits*. Cambridge university press, 2003.

[12] K. Boucart and A. M. Ionescu, 'Double-Gate Tunnel FET With High-k Gate Dielectric', *IEEE Trans. Electron Devices*, vol. 54, no. 7, pp. 1725–1733, 2007.

[13] M. Yang, S. Wang, Y. Feng, G. Peng, and Y. Sun, 'Electronic structure of germanium nitride considered for gate dielectrics', *J. Appl. Phys.*, vol. 102, no. 1, p. 013507, 2007.

[14] C. Chen *et al.*, 'A 90 nm CMOS MS/RF based foundry SOC technology comprising superb 185 GHz f/sub T/RFMOS and versatile, high-Q passive components for cost/performance optimization', in *Electron Devices Meeting, 2003. IEDM'03 Technical Digest. IEEE International*, 2003, pp. 2–5.

[15] A. Kar-Roy *et al.*, 'High density metal insulator metal capacitors using PECVD nitride for mixed signal and RF circuits', in *Interconnect Technology, 1999. IEEE International Conference*, 1999, pp. 245–247.

[16] J. A. Babcock *et al.*, 'Analog characteristics of metal-insulator-metal capacitors using PECVD nitride dielectrics', *IEEE Electron Device Lett.*, vol. 22, no. 5, pp. 230–232, 2001.

[17] S. Van Huylenbroeck, S. Decoutere, R. Venegas, S. Jenei, and G. Winderickx, 'Investigation of PECVD dielectrics for nondispersive metal-insulator-metal capacitors', *IEEE Electron Device Lett.*, vol. 23, no. 4, pp. 191–193, 2002.

[18] S. Jenei, S. Decoutere, S. Van Huylenbroeck, G. Vanhorebeek, and B. Nauwelaers, 'High Q inductors and capacitors on Si substrate', in *Silicon Monolithic Integrated Circuits in RF Systems, 2001. Digest of Papers. 2001 Topical Meeting on*, 2001, pp. 64–70.

[19] A. Kar-Roy *et al.*, 'Mixed-signal 0.18 µm CMOS and SiGe BiCMOS foundry technologies for ROIC applications', in *Security+ Defence*, 2010, p. 78340R–78340R.

[20] *RF and Analog/Mixed Signal Technologies, International Roadmap for Semiconductors*. 2013.

[21] S. M. Guralnick, 'The contexts of Faraday's electrochemical laws', *Isis*, vol. 70, no. 1, pp. 59–75, 1979.

[22] G. Lupina *et al.*, 'Praseodymium silicate films on Si (100) for gate dielectric applications: Physical and electrical characterization', *J. Appl. Phys.*, vol. 99, no. 11, p. 114109, 2006.

[23] J. Robertson, 'High dielectric constant gate oxides for metal oxide Si transistors', *Rep. Prog. Phys.*, vol. 69, no. 2, p. 327, 2005.

[24] R. M. Wallace and G. D. Wilk, 'High-κ dielectric materials for microelectronics', *Crit. Rev. Solid State Mater. Sci.*, vol. 28, no. 4, pp. 231–285, 2003.

[25] J. W. McPherson, J. Kim, A. Shanware, H. Mogul, and J. Rodriguez, 'Trends in the ultimate breakdown strength of high dielectric-constant materials', *IEEE Trans. Electron Devices*, vol. 50, no. 8, pp. 1771–1778, 2003.

[26] J. Robertson, 'Band offsets of wide-band-gap oxides and implications for future electronic devices', *J. Vac. Sci. Technol. B Microelectron. Nanometer Struct. Process. Meas. Phenom.*, vol. 18, no. 3, pp. 1785–1791, 2000.

[27] J. McPherson, J. Kim, A. Shanware, H. Mogul, and J. Rodriguez, 'Proposed universal relationship between dielectric breakdown and dielectric constant', in *Electron Devices Meeting, 2002. IEDM'02. International*, 2002, pp. 633–636.

[28] K. Chiang *et al.*, 'High-temperature leakage improvement in metal–insulator–metal capacitors by work–function tuning', *IEEE Electron Device Lett.*, vol. 28, no. 3, pp. 235–237, 2007.

[29] S. P. Pavunny *et al.*, 'Holmium hafnate: An emerging electronic device material', *Appl. Phys. Lett.*, vol. 106, no. 11, p. 112902, 2015.

[30] T. Ma *et al.*, 'Special reliability features for Hf-based high-k gate dielectrics', *IEEE Trans. Device Mater. Reliab.*, vol. 5, no. 1, pp. 36–44, 2005.

[31] S. Pan *et al.*, 'High-temperature conduction behaviors of HfO_2/TaN -based metal-insulator-metal capacitors', *J. Appl. Phys.*, vol. 102, no. 7, 2007.

[32] H. Chen *et al.*, 'Electrical characterization and carrier transportation in Hf-silicate dielectrics using ALD gate stacks for 90nm node MOSFETs', *Appl. Surf. Sci.*, vol. 254, no. 19, pp. 6127–6130, 2008.

[33] D. S. Jeong, H. B. Park, and C. S. Hwang, 'Reasons for obtaining an optical dielectric constant from the Poole–Frenkel conduction behavior of atomic-layer-deposited HfO_2 films', *Appl. Phys. Lett.*, vol. 86, no. 7, p. 072903, 2005.

[34] C. Walczyk *et al.*, 'Pulse-induced low-power resistive switching in HfO_2 metal-insulator-metal diodes for nonvolatile memory applications', *J. Appl. Phys.*, vol. 105, no. 11, p. 114103, 2009.

[35] R. K. Hester, K.-S. Tan, M. de Wit, J. Fattaruso, S. Kiriaki, and J. Hellums, 'Fully differential ADC with rail-to-rail common-mode range and nonlinear capacitor compensation', *IEEE J. Solid-State Circuits*, vol. 25, no. 1, pp. 173–183, 1990.

[36] M.-J. Chen and C.-S. Hou, 'A novel cross-coupled inter-poly-oxide capacitor for mixed-mode CMOS processes', *IEEE Electron Device Lett.*, vol. 20, no. 7, pp. 360–362, 1999.

[37] K.-S. Tan *et al.*, 'Error correction techniques for high-performance differential A/D converters', *IEEE J. Solid-State Circuits*, vol. 25, no. 6, pp. 1318–1327, 1990.

[38] X. Yu *et al.*, 'A high-density MIM capacitor (13 fF/μm^2) using ALD HfO_2 dielectrics', *IEEE Electron Device Lett.*, vol. 24, no. 2, pp. 63–65, 2003.

[39] A. Zanchi, F. Tsay, and I. Papantonopoulos, 'Impact of capacitor dielectric relaxation on a 14-bit 70-MS/s pipeline ADC in 3-V BiCMOS', *IEEE J. Solid-State Circuits*, vol. 38, no. 12, pp. 2077–2086, 2003.

[40] C. Zhu *et al.*, 'Voltage and temperature dependence of capacitance of high-K HfO_2 MIM capacitors: A unified understanding and prediction', *IEDM Tech. Dig.*, 2003.

[41] H. Hu *et al.*, 'Physical and electrical characterization of HfO_2 metal–insulator–metal capacitors for Si analog circuit applications', *J. Appl. Phys.*, vol. 94, no. 1, pp. 551–557, 2003.

[42] S. Becu, S. Cremer, and J. Autran, 'Capacitance non-linearity study in Al_2O_3 MIM capacitors using an ionic polarization model', *Microelectron. Eng.*, vol. 83, no. 11, pp. 2422–2426, 2006.

[43] R. Van Dover, R. Fleming, L. Schneemeyer, G. Alers, and D. Werder, 'Advanced dielectrics for gate oxide, DRAM and RF capacitors', in *Electron Devices Meeting, 1998. IEDM'98. Technical Digest., International*, 1998, pp. 823–826.

[44] J.-D. Chen *et al.*, 'Physical and Electrical Characterization of Metal-Insulator-Metal Capacitors With Sm_2O_3 and Sm_2O_3/SiO_2 Laminated Dielectrics for Analog Circuit Applications', *IEEE Trans. Electron Devices*, vol. 56, no. 11, p. 2683, 2009.

[45] P. Gonon and C. Vallée, 'Modeling of nonlinearities in the capacitance-voltage characteristics of high-k metal-insulator-metal capacitors', *Appl. Phys. Lett.*, vol. 90, no. 14, p. 142906, 2007.

[46] S. Becu, S. Cremer, O. Noblanc, J.-L. Autran, and P. Delpech, 'Characterization and modeling of Al_2O_3 MIM capacitors: temperature and electrical field effects', in *Solid-State Device Research Conference, 2005. ESSDERC 2005. Proceedings of 35th European*, 2005, pp. 265–268.

[47] S. Bécu, S. Crémer, and J.-L. Autran, 'Microscopic model for dielectric constant in metal-insulator-metal capacitors with high-permittivity metallic oxides', *Appl. Phys. Lett.*, vol. 88, no. 5, p. 052902, 2006.

[48] C. Wenger *et al.*, 'Microscopic model for the nonlinear behavior of high-k metal-insulator-metal capacitors', *J. Appl. Phys.*, vol. 103, no. 10, p. 104103, 2008.

[49] S. Blonkowski, 'Nonlinear capacitance variations in amorphous oxide metal-insulator-metal structures', *Appl. Phys. Lett.*, vol. 91, no. 17, p. 172903, 2007.

[50] T. H. Phung, P. Steinmann, R. Wise, Y.-C. Yeo, and C. Zhu, 'Modeling the Negative Quadratic VCC of SiO_2 in MIM Capacitor', *IEEE Electron Device Lett.*, vol. 32, no. 12, pp. 1671–1673, 2011.

[51] P. Gonon and C. Vallée, 'Understanding capacitance-voltage nonlinearities in microelectronic metal-insulator-metal (MIM) capacitors', in *Properties and Applications of Dielectric Materials (ICPADM), 2015 IEEE 11th International Conference on the*, 2015, pp. 636–639.

[52] S. Blonkowski, 'Filamentary model of dielectric breakdown', *J. Appl. Phys.*, vol. 107, no. 8, p. 084109, 2010.

[53] D. L. Crook, 'Method of determining reliability screens for time dependent dielectric breakdown', in *Reliability Physics Symposium, 1979. 17th Annual*, 1979, pp. 1–7.

[54] E. S. Anolick and G. R. Nelson, 'Low-field time-dependent dielectric integrity', *IEEE Trans. Reliab.*, vol. 29, no. 3, pp. 217–221, 1980.

[55] A. Berman, 'Time-zero dielectric reliability test by a ramp method', in *Reliability Physics Symposium, 1981. 19th Annual*, 1981, pp. 204–209.

[56] I. Chen, S. Holland, and C. Hut, 'A quantitative physical model for time-dependent breakdown in SiO_2', in *Reliability Physics Symposium, 1985. 23rd Annual*, 1985, pp. 24–31.

[57] J. Lee, I.-C. Chen, and C. Hu, 'Statistical modeling of silicon dioxide reliability', in *Reliability Physics Symposium 1988. 26th Annual Proceedings, International*, 1988, pp. 131–138.

[58] K. F. Schuegraf and C. Hu, 'Hole injection SiO_2 breakdown model for very low voltage lifetime extrapolation', *IEEE Trans. Electron Devices*, vol. 41, no. 5, pp. 761–767, 1994.

[59] J. Sune and E. Wu, 'A new quantitative hydrogen-based model for ultra-thin oxide breakdown', in *VLSI Technology, 2001. Digest of Technical Papers. 2001 Symposium on*, 2001, pp. 97–98.

[60] J. Lloyd, E. Liniger, and T. Shaw, 'Simple model for time-dependent dielectric breakdown in inter-and intralevel low-k dielectrics', *J. Appl. Phys.*, vol. 98, no. 8, p. 084109, 2005.

[61] F. Chen *et al.*, 'A comprehensive study of low-k SiCOH TDDB phenomena and its reliability lifetime model development', in *Reliability Physics Symposium Proceedings, 2006. 44th Annual. IEEE International*, 2006, pp. 46–53.

[62] R. S. Achanta, J. L. Plawsky, and W. N. Gill, 'A time dependent dielectric breakdown model for field accelerated low-k breakdown due to copper ions', *Appl. Phys. Lett.*, vol. 91, no. 23, p. 234106, 2007.

[63] E. Y. Wu and J. Suné, 'Power-law voltage acceleration: A key element for ultra-thin gate oxide reliability', *Microelectron. Reliab.*, vol. 45, no. 12, pp. 1809–1834, 2005.

[64] E. Y. Wu *et al.*, 'Experimental evidence of T_{BD} power-law for voltage dependence of oxide breakdown in ultrathin gate oxides', *IEEE Trans. Electron Devices*, vol. 49, no. 12, pp. 2244–2253, 2002.

[65] K. Ohgata *et al.*, 'Universality of power-law voltage dependence for TDDB lifetime in thin gate oxide PMOSFETs', in *Reliability Physics Symposium, 2005. Proceedings. 43rd Annual. 2005 IEEE International*, 2005, pp. 372–376.

[66] J. McPherson and H. Mogul, 'Underlying physics of the thermochemical E model in describing low-field time-dependent dielectric breakdown in SiO_2 thin films', *J. Appl. Phys.*, vol. 84, no. 3, pp. 1513–1523, 1998.

[67] J. McPherson and R. Khamankar, 'Molecular model for intrinsic time-dependent dielectric breakdown in SiO_2 dielectrics and the reliability implications for hyper-thin gate oxide', *Semicond. Sci. Technol.*, vol. 15, no. 5, p. 462, 2000.

[68] J. McPherson and H. Mogul, 'Disturbed bonding states in SiO_2 thin-films and their impact on time-dependent dielectric breakdown', in *Reliability Physics Symposium Proceedings, 1998. 36th Annual. 1998 IEEE International*, 1998, pp. 47–56.

[69] P. Lenahan and J. Conley Jr, 'What can electron paramagnetic resonance tell us about the Si/SiO_2 system?', *J. Vac. Sci. Technol. B Microelectron. Nanometer Struct. Process. Meas. Phenom.*, vol. 16, no. 4, pp. 2134–2153, 1998.

[70] I.-C. Chen, S. E. Holland, and C. Hu, 'Electrical breakdown in thin gate and tunneling oxides', *IEEE Trans. Electron Devices*, vol. 32, no. 2, pp. 413–422, 1985.

[71] R. Moazzami, J. C. Lee, and C. Hu, 'Temperature acceleration of time-dependent dielectric breakdown', *IEEE Trans. Electron Devices*, vol. 36, no. 11, pp. 2462–2465, 1989.

[72] I. Chen, S. Holland, K. Young, C. Chang, and C. Hu, 'Substrate hole current and oxide breakdown', *Appl. Phys. Lett.*, vol. 49, no. 11, pp. 669–671, 1986.

[73] S. J. Kim *et al.*, 'Improvement of voltage linearity in high-/spl kappa/MIM capacitors using HfO_2-SiO_2 stacked dielectric', *IEEE Electron Device Lett.*, vol. 25, no. 8, pp. 538–540, 2004.

[74] C. Vallée, P. Gonon, C. Jorel, and F. El Kamel, 'Electrode oxygen-affinity influence on voltage nonlinearities in high-k metal-insulator-metal capacitors', *Appl. Phys. Lett.*, vol. 96, no. 23, p. 233504, 2010.

[75] T. Kawanago *et al.*, 'Covalent nature in La-silicate gate dielectrics for oxygen vacancy removal', *IEEE Electron Device Lett.*, vol. 33, no. 3, pp. 423–425, 2012.

[76] S. Saito, D. Hisamoto, S. Kimura, and M. Hiratani, 'Unified Mobility Model for High-κ Gate Stacks', in *Technical Digest - International Electron Devices Meeting*, 2003, pp. 797–800.

[77] *Joint Electron Device Engineering Council (JEDEC) Solid State Technology Association*.

[78] U. Schwalke, M. Pölzl, T. Sekinger, and M. Kerber, 'Ultra-thick gate oxides: charge generation and its impact on reliability', *Microelectron. Reliab.*, vol. 41, no. 7, pp. 1007–1010, 2001.

[79] S.-L. Jeng, J.-C. Lu, and K. Wang, 'A review of reliability research on nanotechnology', *IEEE Trans. Reliab.*, vol. 56, no. 3, pp. 401–410, 2007.

[80] R. Degraeve *et al.*, 'New insights in the relation between electron trap generation and the statistical properties of oxide breakdown', *IEEE Trans. Electron Devices*, vol. 45, no. 4, pp. 904–911, 1998.

[81] 'ITRS 2.0 Home Page', *International Technology Roadmap for Semiconductors*, 2015. [Online]. Available: http://www.itrs2.net/. [Accessed: 13-Jan-2018].

[82] S. George, A. Ott, and J. Klaus, 'Surface chemistry for atomic layer growth', *J. Phys. Chem.*, vol. 100, no. 31, pp. 13121–13131, 1996.

[83] T. Suntola, 'Atomic layer epitaxy', *Mater. Sci. Rep.*, vol. 4, no. 5, pp. 261–312, 1989.

[84] M. Ritala and M. Leskelä, 'Chapter 2 - Atomic layer deposition', in *Handbook of Thin Films*, H. S. Nalwa, Ed. Burlington: Academic Press, 2002, pp. 103–159.

[85] M. Leskelä and M. Ritala, 'Atomic layer deposition (ALD): from precursors to thin film structures', *Thin Solid Films*, vol. 409, no. 1, pp. 138–146, 2002.

[86] R. L. Puurunen, 'Surface chemistry of atomic layer deposition: A case study for the trimethylaluminum/water process', *J. Appl. Phys.*, vol. 97, no. 12, p. 9, 2005.

[87] H. Profijt, S. Potts, M. Van de Sanden, and W. Kessels, 'Plasma-assisted atomic layer deposition: basics, opportunities, and challenges', *J. Vac. Sci. Technol. Vac. Surf. Films*, vol. 29, no. 5, p. 050801, 2011.

[88] *http://www.jawoollam.com/tutorial_4.html*. .

[89] H. G. Tompkins and E. A. Irene, *Handbook of Ellipsometry*. New York: William Andrew Publishing, 2005.

[90] H. Fujiwara, *Spectroscopic ellipsometry: principles and applications*. John Wiley & Sons, 2007.

[91] E. Langereis, S. Heil, M. Van De Sanden, and W. Kessels, 'In situ spectroscopic ellipsometry study on the growth of ultrathin TiN films by plasma-assisted atomic layer deposition', *J. Appl. Phys.*, vol. 100, no. 2, p. 023534, 2006.

[92] S. Heil, E. Langereis, A. Kemmeren, F. Roozeboom, M. Van De Sanden, and W. Kessels, 'Plasma-assisted atomic layer deposition of TiN monitored by in situ spectroscopic ellipsometry', *J. Vac. Sci. Technol. Vac. Surf. Films*, vol. 23, no. 4, pp. L5–L8, 2005.

[93] J. Isidorsson, I. Giebels, H. Arwin, and R. Griessen, 'Optical properties of MgH_2 measured in situ by ellipsometry and spectrophotometry', *Phys. Rev. B*, vol. 68, no. 11, p. 115112, 2003.

[94] H. Knoops, A. Mackus, M. Donders, M. Van De Sanden, P. Notten, and W. Kessels, 'Remote plasma ALD of platinum and platinum oxide films', *Electrochem. Solid-State Lett.*, vol. 12, no. 7, pp. G34–G36, 2009.

[95] H. Van Bui, A. Groenland, A. Aarnink, R. Wolters, J. Schmitz, and A. Kovalgin, 'Growth kinetics and oxidation mechanism of ALD TiN thin films monitored by in situ spectroscopic ellipsometry', *J. Electrochem. Soc.*, vol. 158, no. 3, pp. H214–H220, 2011.

[96] W. Cabrera, M. Halls, I. Povey, and Y. Chabal, 'Surface Oxide Characterization and Interface Evolution in Atomic Layer Deposition of Al_2O_3 on InP (100) Studied by in Situ Infrared Spectroscopy', *J. Phys. Chem. C*, vol. 118, no. 11, pp. 5862–5871, 2014.

[97] E. Langereis, S. Heil, H. Knoops, W. Keuning, M. Van De Sanden, and W. Kessels, 'In situ spectroscopic ellipsometry as a versatile tool for studying atomic layer deposition', *J. Phys. Appl. Phys.*, vol. 42, no. 7, p. 073001, 2009.

[98] M. T. Bohr, R. S. Chau, T. Ghani, and K. Mistry, 'The high-k solution', *IEEE Spectr.*, vol. 44, no. 10, pp. 29–35, 2007.

[99] K. Mistry *et al.*, 'A 45nm logic technology with high-k+ metal gate transistors, strained silicon, 9 Cu interconnect layers, 193nm dry patterning, and 100% Pb-free packaging', in *Technical Digest - International Electron Devices Meeting, IEDM*, 2007, pp. 247–250.

[100] K. Chiang *et al.*, 'Very high-density (23 fF/um^2) RF MIM capacitors using high- k TaTiO as the dielectric', *IEEE Electron Device Lett.*, vol. 26, no. 10, pp. 728–730, 2005.

[101] M. Yang *et al.*, 'Very high density RF MIM capacitors (17 fF/ um^2) using high- k Al_2O_3 doped Ta_2O_5 dielectrics', *IEEE Microw. Wirel. Compon. Lett.*, vol. 13, no. 10, pp. 431–433, 2003.

[102] J.-Y. Choi *et al.*, 'Structural and Electrical Properties of Mn-Doped $Bi_4Ti_3O_{12}$ Thin Film Grown on TiN/SiO_2/Si Substrate for RF MIM Capacitors', *IEEE Trans. Electron Devices*, vol. 56, no. 8, pp. 1631–1636, 2009.

[103] K.-H. Cho *et al.*, 'Electrical Properties of Amorphous $Bi_5Nb_3O_{15}$ Thin Film for RF MIM Capacitors', *IEEE Electron Device Lett.*, vol. 29, no. 7, pp. 684–687, 2008.

[104] T. Lacrevaz *et al.*, 'Wide Band Frequency Characterization of High Permittivity Dielectrics (High-K) for RF MIM Capacitors Integrated in BEOL', in *Interconnect Technology Conference, 2006 International*, 2006, pp. 78–80.

[105] K. C. Chiang, C. H. Lai, A. Chin, H. L. Kao, S. P. McAlister, and C. C. Chi, 'Very high density RF MIM capacitor compatible with VLSI', in *IEEE MTT-S International Microwave Symposium Digest*, 2005, vol. 2005, pp. 287–290.

[106] S. Mondal, S.-J. Shih, F.-H. Chen, and T.-M. Pan, 'Structural and Electrical Characteristics of Lu_2O_3 Dielectric Embedded MIM Capacitors for Analog IC Applications', *IEEE Trans. Electron Devices*, vol. 59, no. 6, pp. 1750–1756, 2012.

[107] A. Srivastava, O. Mangla, and V. Gupta, 'Study of La-Incorporated HfO_2 MIM Structure Fabricated Using PLD System for Analog/Mixed Signal Applications', *IEEE Trans. Nanotechnol.*, vol. 14, no. 4, pp. 612–618, 2015.

[108] S. Chen, C. Lai, A. Chin, J. Hsieh, and J. Liu, 'High-density MIM capacitors using Al_2O_3 and $AlTiO_x$ dielectrics', *IEEE Electron Device Lett.*, vol. 23, no. 4, pp. 185–187, 2002.

[109] K. Allers, P. Brenner, and M. Schrenk, 'Dielectric reliability and material properties of Al_2O_3 in metal insulator metal capacitors (MIMCAP) for RF bipolar technologies in comparison to SiO_2, Si_3N_4 and Ta_2O_5', in *Proceedings of the Bipolar/BiCMOS Circuits and Technology Meeting*, 2003, pp. 35–38.

[110] J. Robertson and R. M. Wallace, 'High-K materials and metal gates for CMOS applications', *Mater. Sci. Eng. R Rep.*, vol. 88, pp. 1–41, 2015.

[111] Y. Tu *et al.*, 'Characterization and comparison of high-k metal-insulator-metal (MiM) capacitors in 0.13 um Cu BEOL for mixed-mode and RF applications', in *VLSI Technology, 2003. Digest of Technical Papers. 2003 Symposium on*, 2003, pp. 79–80.

[112] V. Djara *et al.*, 'Low D_{it} $HfO_2/Al_2O_3/In_{0.53}Ga_{0.47}As$ gate stack achieved with plasma-enhanced atomic layer deposition', *Microelectron. Eng.*, vol. 147, pp. 231–234, 2015.

[113] J. Ho Lee, I.-H. Yu, S. Young Lee, and C. Seong Hwang, 'Phase control of HfO_2-based dielectric films for higher-k materials', *J. Vac. Sci. Technol. B Nanotechnol. Microelectron. Mater. Process. Meas. Phenom.*, vol. 32, no. 3, p. 03D109, 2014.

[114] K.-H. Allers, R. Schwab, W. Walter, M. Schrenk, and H. Korner, 'Thermal and dielectric breakdown for metal insulator metal capacitors (MIMCAP) with tantalum pentoxide dielectric', in *Integrated Reliability Workshop Final Report, 2002. IEEE International*, 2002, pp. 96–101.

[115] M. Richard, T. Dean, and S. Delage, 'RF, DC, and reliability characteristics of Ta_2O_5 MIM capacitors', in *Microwave Conference, 2008. EuMC 2008. 38th European*, 2008, pp. 127–130.

[116] J.-J. Yang, J.-D. Chen, R. Wise, P. Steinmann, Y.-C. Yeo, and C. Zhu, 'Performance Improvement of Sm_2O_3 MIM Capacitors by Using Plasma Treatment After Dielectric Formation', *IEEE Electron Device Lett.*, vol. 30, no. 10, pp. 1033–1035, 2009.

[117] S.-H. Wu, C.-K. Deng, T.-H. Hou, and B.-S. Chiou, 'Stability of La_2O_3 metal–insulator–metal capacitors under constant voltage stress', *Jpn. J. Appl. Phys.*, vol. 49, no. 4S, p. 04DB16, 2010.

[118] C. Durand *et al.*, 'Electrical property improvements of yttrium oxide-based metal-insulator-metal capacitors', *J. Vac. Sci. Technol. Vac. Surf. Films*, vol. 24, no. 3, pp. 459–466, 2006.

[119] N. Inoue *et al.*, 'High Performance High-k MIM Capacitor with Plug-in Plate (PiP) for Power Delivery Line Hige-Speed MPUs', in *Interconnect Technology Conference, 2006 International*, 2006, pp. 63–65.

[120] K. Chiang *et al.*, 'Very High Density (44 $fF/\mu m^2$) $SrTiO_3$ MIM Capacitors for RF Applications', *J. Electrochem. Soc.*, vol. 154, no. 3, pp. H214–H216, 2007.

[121] M. Hota *et al.*, 'Characterization of RF sputter deposited $HfAlO_x$ dielectrics for MIM capacitor applications', in *Electron Devices and Semiconductor Technology, 2009. IEDST'09. 2nd International Workshop on*, 2009, pp. 1–4.

[122] X. Yu *et al.*, 'Mim Capacitors with HfO_2 and $HfAlO_x$ for Si RF and Analog Applications', in *MRS Proceedings*, 2003, vol. 766, pp. E5–9.

[123] L. Zhang, W. He, D. S. Chan, and B. J. Cho, 'High-performance MIM capacitors using HfLaO-based dielectrics', *IEEE Electron Device Lett.*, vol. 31, no. 1, pp. 17–19, 2010.

[124] D. Z. Austin, D. Allman, D. Price, S. Hose, and J. F. Conley, 'Plasma Enhanced Atomic Layer Deposition of Al_2O_3/SiO_2 MIM Capacitors', *IEEE Electron Device Lett.*, vol. 36, no. 5, pp. 496–498, 2015.

[125] C. Jorel, C. Vallée, P. Gonon, E. Gourvest, C. Dubarry, and E. Defay, 'High performance metal-insulator-metal capacitor using a $SrTiO_3/ZrO_2$ bilayer', *Appl. Phys. Lett.*, vol. 94, no. 25, p. 253502, 2009.

[126] J.-J. Yang *et al.*, 'Effective Modulation of Quadratic Voltage Coefficient of Capacitance in MIM Capacitors Using Sm_2O_3/SiO_2 Dielectric Stack', *IEEE Electron Device Lett.*, vol. 30, no. 5, pp. 460–462, 2009.

[127] T. H. Phung *et al.*, 'High performance metal-insulator-metal capacitors with Er_2O_3 on ALD SiO_2 for RF applications', *J. Electrochem. Soc.*, vol. 158, no. 12, pp. H1289–H1292, 2011.

[128] J. Lee, Y. Lin, B. Chen, and C. Tsai, 'New metal-insulator-metal capacitor based on $SrTiO_3/Al_2O_3/SrTiO_3$ laminate dielectric', in *Solid-State and Integrated Circuit Technology (ICSICT), 2010 10th IEEE International Conference on*, 2010, pp. 1024–1026.

[129] C.-C. Lin, Y.-H. Wu, R.-S. Jiang, and M.-T. Yu, 'MIM Capacitors Based on $ZrTiO_x/BaZr_yTi_{1-y}O_3$ Featuring Record-Low VCC and Excellent Reliability', *IEEE Electron Device Lett.*, vol. 34, no. 11, pp. 1418–1420, 2013.

[130] S.-U. Park *et al.*, 'Analysis of reliability characteristics of high capacitance density MIM capacitors with SiO_2–HfO_2–SiO_2 dielectrics', *Microelectron. Eng.*, vol. 88, no. 12, pp. 3389–3392, 2011.

[131] C.-S. Ho, S.-J. Chang, S.-C. Chen, J. J. Liou, and H. Li, 'A Reliable Si_3N_4/Al_2O_3-HfO_2 Stack MIM Capacitor for High-Voltage Analog Applications', *IEEE Trans. Electron Devices*, vol. 61, no. 8, pp. 2944–2949, 2014.

[132] Q.-X. Zhang *et al.*, 'Full ALD $Al_2O_3/ZrO_2/SiO_2/ZrO_2/Al_2O_3$ Stacks for High-Performance MIM Capacitors', *IEEE Electron Device Lett.*, vol. 35, no. 11, pp. 1121–1123, 2014.

[133] G. D. Wilk, R. M. Wallace, and J. Anthony, 'High-κ gate dielectrics: Current status and materials properties considerations', *J. Appl. Phys.*, vol. 89, no. 10, pp. 5243–5275, 2001.

[134] H. Kim *et al.*, 'Characteristics of Thin Hf-Silicate Gate Dielectrics after Remote N_2 and N_2O Plasma Post-Treatments', *J. Electrochem. Soc.*, vol. 155, no. 12, pp. G299–G303, 2008.

[135] K. Chung *et al.*, 'Growth Kinetics of Atomic Layer Deposited Hf Silicate-Like Films using $Hf[N(CH_3)(C_2H_5)]_4$ and $SiH[N(CH_3)_2]_3$ Precursors via an H_2O Oxidant', *Electrochem. Solid-State Lett.*, vol. 10, no. 1, pp. G1–G4, 2007.

[136] Z. Zhang, M. Li, and S. A. Campbell, 'A study on charge reduction in HfO_2 gate stacks', *IEEE Trans. Electron Devices*, vol. 52, no. 8, pp. 1839–1844, 2005.

[137] M. Hiratani, K. Torii, Y. Shimamoto, and S.-I. Saito, 'Built-in interface in high-κ gate stacks', *Appl. Surf. Sci.*, vol. 216, no. 1, pp. 208–214, 2003.

[138] H. Takeuchi and T.-J. King, 'Scaling limits of hafnium–silicate films for gate-dielectric applications', *Appl. Phys. Lett.*, vol. 83, no. 4, pp. 788–790, 2003.

[139] B. H. Lee *et al.*, 'Electric-field-driven dielectric breakdown of metal-insulator-metal hafnium silicate', *Appl. Phys. Lett.*, vol. 91, no. 24, p. 243514, 2007.

[140] S. Monaghan and I. Povey, 'Scalable high-k metal-insulator-metal capacitors with low leakage, high breakdown fields and improved voltage linearity', *Electron. Lett.*, vol. 48, no. 4, pp. 230–232, 2012.

[141] J. A. Speer and B. J. Cooper, 'Crystal structure of synthetic hafnon, $HfSiO_4$, comparison with zircon and the actinide orthosilicates.', *Am. Mineral.*, vol. 67, no. 7–8, pp. 804–808, 1982.

[142] K. Suzuki, H. Kouta, and H. Nagasawa, 'Hf-Zr interdiffusion in single crystal zircon', *Geochem. J.*, vol. 26, no. 2, pp. 99–104, 1992.

[143] F. El Kamel, P. Gonon, and C. Vallée, 'Experimental evidence for the role of electrodes and oxygen vacancies in voltage nonlinearities observed in high-k metal-insulator-metal capacitors', *Appl. Phys. Lett.*, vol. 91, no. 17, p. 172909, 2007.

[144] A. Hastings, *The Art of Analog Layout*. Pearson Prentice Hall, 2001.

[145] C. Ng, K. Chew, and S. Chu, 'Characterization and comparison of PECVD silicon nitride and silicon oxynitride dielectric for MIM capacitors', *IEEE Electron Device Lett.*, vol. 24, no. 8, pp. 506–508, 2003.

[146] R. Scott and D. Dumin, 'The Transient Nature of Excess Low-Level Leakage Currents in Thin Oxides', *J. Electrochem. Soc.*, vol. 142, no. 2, pp. 586–590, 1995.

[147] S. Yamamichi, A. Yamamichi, D. Park, T.-J. King, and C. Hu, 'Impact of time dependent dielectric breakdown and stress-induced leakage current on the reliability of high dielectric constant (Ba, Sr)TiO_3 thin-film capacitors for Gbit-scale DRAMs', *IEEE Trans. Electron Devices*, vol. 46, no. 2, pp. 342–347, 1999.

[148] D. DiMaria and E. Cartier, 'Mechanism for stress-induced leakage currents in thin silicon dioxide films', *J. Appl. Phys.*, vol. 78, no. 6, pp. 3883–3894, 1995.

[149] R. Degraeve, G. Groeseneken, R. Bellens, M. Depas, and H. E. Maes, 'A consistent model for the thickness dependence of intrinsic breakdown in ultra-thin oxides', in *Electron Devices Meeting, 1995. IEDM'95., International*, 1995, pp. 863–866.

[150] J. S. Suehle, 'Ultrathin gate oxide reliability: Physical models, statistics, and characterization', *IEEE Trans. Electron Devices*, vol. 49, no. 6, pp. 958–971, 2002.

[151] T. Nigam, R. Degraeve, G. Groeseneken, M. Heyns, and H. Maes, 'Constant current charge-to-breakdown: Still a valid tool to study the reliability of MOS structures?', in *Reliability Physics Symposium Proceedings, 1998. 36th Annual. 1998 IEEE International*, 1998, pp. 62–69.

[152] H.-M. Kwon *et al.*, 'A Correlation Between Oxygen Vacancies and Reliability Characteristics in a Single Zirconium Oxide Metal-Insulator-Metal Capacitor', *IEEE Trans. Electron Devices*, vol. 61, no. 8, pp. 2619–2627, 2014.

[153] J. McPherson, R. Khamankar, and A. Shanware, 'Complementary model for intrinsic time-dependent dielectric breakdown in SiO_2 dielectrics', *J. Appl. Phys.*, vol. 88, no. 9, pp. 5351–5359, 2000.

[154] J. McPherson, 'Determination of the nature of molecular bonding in silica from time-dependent dielectric breakdown data', *J. Appl. Phys.*, vol. 95, no. 12, pp. 8101–8109, 2004.

[155] D. DiMaria, 'Explanation for the polarity dependence of breakdown in ultrathin silicon dioxide films', *Appl. Phys. Lett.*, vol. 68, no. 21, pp. 3004–3006, 1996.

[156] A. Shanware, 'Reliability evaluation of HfSiON gate dielectric film with 12.8A SiO_2 equivalent thickness', *Proc. IEDM Tech Dig. 2001*, 2001.

[157] D.-Y. Cho, C.-H. Min, J. Kim, S.-J. Oh, and M. G. Kim, 'Bond nature of oxygen-deficient HfO_2/ Si (100) film', *Appl. Phys. Lett.*, vol. 89, no. 25, p. 253510, 2006.

[158] S. Kasap and P. Capper, *Springer handbook of electronic and photonic materials*. Springer Science & Business Media, 2006.

[159] J. J. Kim *et al.*, 'Intrinsic time zero dielectric breakdown characteristics of HfAlO alloys', *IEEE Trans. Electron Devices*, vol. 60, no. 11, pp. 3683–3689, 2013.

[160] C.-M. Hsu and J.-G. Hwu, 'Improvement of electrical performance of HfO_2/SiO_2/4H-SiC structure with thin SiO_2', *ECS J. Solid State Sci. Technol.*, vol. 2, no. 8, pp. N3072–N3078, 2013.

[161] C.-C. Yeh *et al.*, 'Frenkel-Poole trap energy extraction of atomic layer deposited Al_2O_3 and Hf_xAl_yO thin films', *Appl. Phys. Lett.*, vol. 91, no. 11, p. 113521, 2007.

[162] J. Grepstad, P. Gartland, and B. Slagsvold, 'Anisotropic work function of clean and smooth low-index faces of aluminium', *Surf. Sci.*, vol. 57, no. 1, pp. 348–362, 1976.

[163] S. Monaghan, P. Hurley, K. Cherkaoui, M. Negara, and A. Schenk, 'Determination of electron effective mass and electron affinity in HfO_2 using MOS and MOSFET structures', *Solid-State Electron.*, vol. 53, no. 4, pp. 438–444, 2009.

[164] V. Re, M. Manghisoni, L. Ratti, V. Speziali, and G. Traversi, 'Total ionizing dose effects on the analog performance of a 0.13um CMOS technology', in *Radiation Effects Data Workshop, 2005. IEEE*, 2005, pp. 122–126.

[165] M. Manghisoni, L. Ratti, V. Re, V. Speziali, G. Traversi, and A. Candelori, 'Comparison of ionizing radiation effects in 0.18 and 0.25um CMOS technologies for analog applications', *IEEE Trans. Nucl. Sci.*, vol. 50, no. 6, pp. 1827–1833, 2003.

[166] J. Osborn, R. Lacoe, D. Mayer, and G. Yabiku, 'Total dose hardness of three commercial CMOS microelectronics foundries', in *Radiation and Its Effects on Components and Systems, 1997. RADECS 97. Fourth European Conference on*, 1997, pp. 265–270.

[167] J. R. Schwank *et al.*, 'Radiation effects in MOS oxides', *IEEE Trans. Nucl. Sci.*, vol. 55, no. 4, pp. 1833–1853, 2008.

[168] R. Schrimpf, 'Radiation effects in microelectronics', in *Radiation Effects on Embedded Systems*, Springer, 2007, pp. 11–29.

[169] R. Velazco, P. Fouillat, and R. Reis, *Radiation effects on embedded systems*. Springer Science & Business Media, 2007.

[170] T.-P. Ma and P. V. Dressendorfer, *Ionizing radiation effects in MOS devices and circuits*. John Wiley & Sons, 1989.

[171] V. Singh, N. Shashank, D. Kumar, and R. Nahar, 'Effects of heavy-ion irradiation on the electrical properties of RF-sputtered HfO_2 thin films for advanced CMOS devices', *Radiat. Eff. Defects Solids*, vol. 167, no. 3, pp. 204–211, 2012.

[172] F. B. Ergin, R. Turan, S. T. Shishiyanu, and E. Yilmaz, 'Effect of γ-radiation on HfO_2 based MOS capacitor', *Nucl. Instrum. Methods Phys. Res. Sect. B Beam Interact. Mater. At.*, vol. 268, no. 9, pp. 1482–1485, 2010.

[173] C. Zhao *et al.*, 'High-k materials and their response to gamma ray radiation', *J. Vac. Sci. Technol. B Microelectron. Nanometer Struct. Process. Meas. Phenom.*, vol. 27, no. 1, pp. 411–415, 2009.

[174] D. M. Fleetwood *et al.*, 'Effects of device aging on microelectronics radiation response and reliability', *Microelectron. Reliab.*, vol. 47, no. 7, pp. 1075–1085, 2007.

[175] G. Lucovsky *et al.*, 'Differences between charge trapping states in irradiated nano-crystalline HfO_2 and non-crystalline Hf silicates', *IEEE Trans. Nucl. Sci.*, vol. 53, no. 6, pp. 3644–3648, 2006.

[176] M. Ding, Y. Cheng, X. Liu, and X. Li, 'Total dose response of hafnium oxide based metal-oxide-semiconductor structure under gamma-ray irradiation', *IEEE Trans. Dielectr. Electr. Insul.*, vol. 21, no. 4, pp. 1792–1800, 2014.

[177] S. Zafar, A. Callegari, E. Gusev, and M. V. Fischetti, 'Charge trapping related threshold voltage instabilities in high permittivity gate dielectric stacks', *J. Appl. Phys.*, vol. 93, no. 11, pp. 9298–9303, 2003.

[178] E. Miranda *et al.*, 'Effects of the electrical stress on the conduction characteristics of metal gate/MgO/InP stacks', *Microelectron. Reliab.*, vol. 49, no. 9, pp. 1052–1055, 2009.

[179] M. Rahman, E. Evangelou, I. Androulidakis, A. Dimoulas, G. Mavrou, and S. Galata, 'SILC decay in La_2O_3 gate dielectrics grown on Ge substrates subjected to constant voltage stress', *Solid-State Electron.*, vol. 54, no. 9, pp. 979–984, 2010.

[180] R. O'Connor, G. Hughes, P. Casey, and S. B. Newcomb, 'Degradation and breakdown characteristics of thin MgO dielectric layers', *J. Appl. Phys.*, vol. 107, no. 2, p. 024501, 2010.

[181] A. Scarpa *et al.*, 'Ionizing radiation induced leakage current on ultra-thin gate oxides', *IEEE Trans. Nucl. Sci.*, vol. 44, no. 6, pp. 1818–1825, 1997.

Appendix A

A.1 Journal Publications and Presentations

A.1.1 Journal Publications

- B. J. Hutchinson, V. S. Teodorescu, R. Negrea, B. Sheehan, P. Carolan, S. O'Brien, M. Modreanu, M.E. Pemble and I. M. Povey, Influence of Substrate on Hafnium Silicate Metal-Insulator-Metal Capacitors Grown by Atomic Layer Deposition, ECS Transactions 66 (5) 269-275 (2015)
- Scott Monaghan, Eamon O'Connor, Ian M. Povey, Brendan J. Sheehan, Karim Cherkaoui, Barry J. A. Hutchinson, and Paul K. Hurley, Effects of Alternating Current Voltage Amplitude and Oxide Capacitance on Mid-gap Interface State Defect Density Extractions in $In_{0.53}Ga_{0.47}As$ Capacitors, Journal of Vacuum Science Technology B 31, 01A119 (2013)

A.1.2 Presentations

- In-situ ellipsometry investigation of hafnium silicate and hafnia films grown by atomic layer deposition, B. J. A. Hutchinson, M. Modreanu, S. O'Brien, M. McCarthy and I. M. Povey, EMRS Lille 2015 - Presentation
- Influence of Substrate on Hafnium Silicate Metal-Insulator-Metal Capacitors Grown by Atomic Layer Deposition, B. J. Hutchinson, V. S. Teodorescu, R. Negrea, B. Sheehan, P. Carolan, S. O'Brien, M. Modreanu, M.E. Pemble and I. M. Povey, ECS Chicago 2015 - Presentation
- Electrical Characterisation of Gamma-ray Irradiated High-κ Metal-Insulator-Metal Capacitors for Space Applications EvaluationEuropean, B.J.A. Hutchinson, I.M. Povey, B.J. Sheehan, E. Sheehan, O.Z. Olszewski, K. Cherkaoui, É. O'Connor, R. Duane, P.K. Hurley, and S. Monaghan, Space Agency 8th Round Table on Micro and Nano Technologies for Space Applications 2012 - Presentation
- An Investigation into the Electrical Properties of Hafnium Silicate MIM Capacitors, B. J. Hutchinson, Ian M. Povey, Paul K. Hurley and Scott Monaghan, Intel ERIC 2012 - Poster

Appendix B

B.1 Ellipsometry Investigation of Dielectric Metal Oxide Thin Film Growth by Atomic Layer Deposition

Generally, ALD film growth is considered to possess two regimes, nucleation and bulk growth. As nucleation may differ considerably depending on the substrate it is well recognised that the nucleation should be studied in detail. However, it often assumed that bulk growth proceeds at a constant rate irrespective of substrate. Such a hypothesis is not without problems; nucleation may lead to a bulk film of a particular phase (templating), mixed phases, or strain that may influence the bulk GPC. Also, other factors such as changes in reactor temperature, wall deposits, plasma characteristics and precursor condition and delivery can influence film growth at any point in the process. For this reason both the nucleation and bulk growth behaviours of ALD grown films require detailed study.

Spectroscopic ellipsometry is a non-invasive technique that has the sensitivity to detect the nominal thickness changes (sub Angstrom) that are necessary to evaluate ALD on the half cycle scale. For this reason it has become has become increasingly popular not only as a process quality monitor but to study the fundamentals of growth. In this work we employ in-situ spectroscopic ellipsometry to perform preliminary studies on the growth processes of Al_2O_3 and two high-k materials HfO_2 and $HfSiO_x$ in real time, on a range of technologically relevant substrates. In

particular we focus on the nucleation processes and highlight the influence of both process parameters and the nature of the substrate.

B.2 Methods and Materials

B.2.1 Atomic layer Deposition

Aluminium oxide films were grown on $In_{0.53}Ga_{0.47}$ As by atomic layer deposition at 300˚C with a Picosun R200 reactor employing Trimethyl aluminium (TMA) and water as precursors. For the hafnia based dielectrics the growth temperature was reduced to 250˚C. The sources for the hafium oxide thin films were Tetrakis(ethylmethylamino) hafnium (TEMAH) and water. For both binary oxides each half cycle was separated by 6 second purges. For the hafnium silicates, the sources, TEMAH and Tetrakis(dimethylamino) silane (TDMAS) were pulsed simultaneously as the first half cycle with a remote argon-oxygen plasma (2.8 kW) pulse completing the cycle. In this study all depositions were 70 cycles except for the hafnium silicate on titanium nitride which was 30 cycles and the hafnium silicate on the platinum substrate which had 100 cycles. Hafnia deposition was performed on five substrate types; a sputtered bottom platinum electrode (~220 nm) with a sputtered titanium adhesion layer (~ 10 nm) between the platinum and silicon dioxide isolation layer; titanium nitride (20 nm) with native oxide on a silicon dioxide isolation layer; indium phosphide with native oxide; stainless steel.

B.2.2 Ellipsometry

Ellipsometry is a technique which measures the change in polarization as light reflects from and transmits through a material. Electromagnetic waves consist of an electronic component and a magnetic component orthogonal to each other. In ellipsometry it is only necessary to discuss the polarization; the electric field behaviour in space and time. Ellipsometry uses linearly polarized light which when reflected off a sample changes polarization to elliptical. This change in polarization is represented as an amplitude ratio, Ψ, and the phase difference, Δ. The response of the material is dependent on its thickness and optical constants, and can be been used to establish either the thickness or optical constants of thin films.

When applied to ALD in-situ ellipsometry can be used monitor both the growth per cycle and the response within a cycle. For example, for a binary ALD metal oxide system, pulsing the metal precursor results in a surface reaction with the substrate surface and an apparent increase in film thickness; as determined from the spectroscopic ellipsometry data. Following a subsequent purge, an oxidising plasma pulse reacts with the chemisorbed metal precursor molecules and resulting in an apparent decrease in film thickness. The resulting thickness difference not only gives the apparent growth per cycle but also has the potential to give additional insight to the process through examination of the resultant saw tooth shaped growth profile.

B.2.4 Methodology

The film growth in this work was carried out in a Picosun R200 ALD system and monitored by in situ ellipsometry using a Woollam M2000D system with a spectral range of 193 nm to 998.9 nm operating in a dynamic capture mode. All ellipsometry analysis was performed using Woollam's CompleteEASE software using the standard library. A standard Cauchy empirical model was used to describe the dispersion of the refractive index n for the HfO_2, $HfSiO_x$ and Al_2O_3 oxides deposited by ALD in this study in the wavelength range of 280 nm – 998 nm:

$$n = A_n + \frac{B_n}{\lambda^2} + \frac{C_n}{\lambda^4}$$

where *A*, *B* and *C* are constants fitted in the modeling and λ is wavelength.

Prior to experimental data collection the ellipsometer was calibrated in situ using a Woollam calibration standard wafer, window effects were taken in to consideration as part of this calibration procedure. The sample was loaded in to the growth chamber and brought to the desired growth temperature. It was observed that the alignment initially drifted from optimal during sample heating, stabilising when thermal equilibrium of the substrate and chamber was reached. The alignment drift was significant, having a marked influence on the analysis of any in-situ data taken before reaching temperature equilibrium. Therefore, samples were allowed to stabilise in chamber for 40 minutes systems prior to in-situ ellipsometry. The measurement time was set to capture data every 1.6 s which was deemed suitable for these experiments, since the purge times between the oxygen source and amine were far greater (6-9 s).

The measurement was started and the substrate was monitored in situ for a few minutes prior to growth to ensure stability.

B.3 Results and discussion – Spectroscopic Ellipsometry Characterisation and Analysis

Time resolved spectroscopic ellipsometry data was measured for the HfO_2 growth on substrates of silicon (with native SiO_2), titanium nitride, stainless steel, platinum and indium phosphide, all with their native oxides. As illustrated in Figure A.1, the native amorphous SiO_2 on the Si substrate appears to have minimal influence on the nucleation of the HfO_2 film growth. The SiO_2 native oxide surface appears to be quite chemically reactive and readily reacts with the hafnium amine precursor (TEMAH). These nucleation sites where the initial reactions occur are most likely hydroxyl groups (OH) and surface defects. There are a reduced number of chemisorption sites available on the native oxide surface compared to the bulk growth regime which is reflected in the observed initial reduced GPC. After the first seven cycles of the nucleation regime the GPC increases and this may be due to a coalescence of the nucleation sites and a saturation of available chemisorption sites indicating a bulk regime growth. This second change in GPC may suggest a densification of the HfO_2 film or a phase change from an amorphous film to a polycrystalline.

As shown in Figure A.2, the nucleation phase of the HfO_2 film on the native "oxide" of the TiN substrate is slightly longer than on Si requiring nine cycles. This may be due to a lower density of chemisorption sites, principally hydroxyl groups and defects. A linear bulk growth regime is established from cycle 10 onwards, however,

the GPC ~ 0.8 Å is significantly lower than the equivalent GPC ~ 1.0 Å for the Si substrate. This may indicate a denser film growth after nucleation on the TiN substrate, perhaps more crystalline than the film growth on the Si substrate.

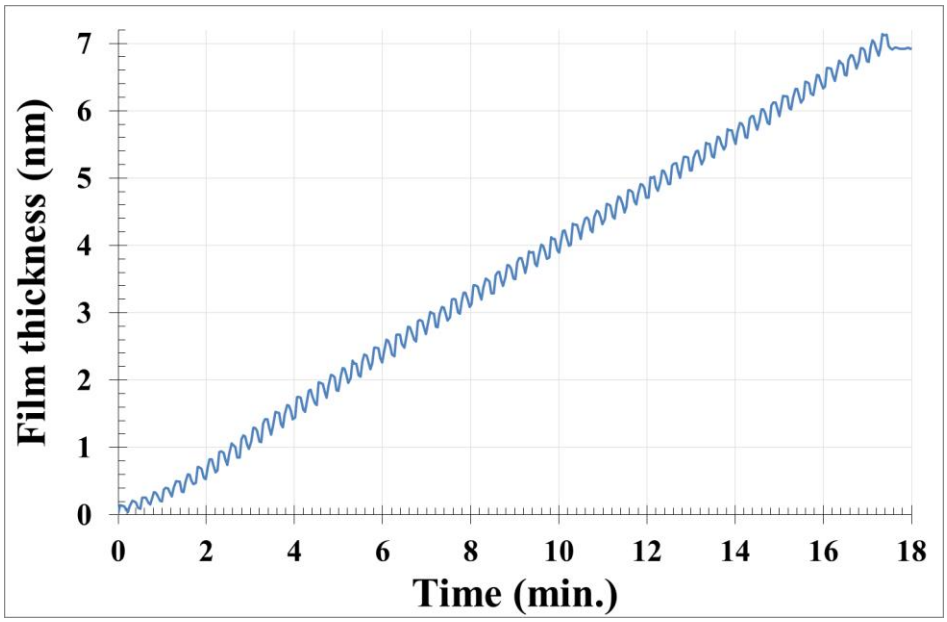

Figure A.1 Optical response of HfO2 growth on a silicon substrate, the SiO2 native oxide seems to have a minimal influence on the nucleation of the film.

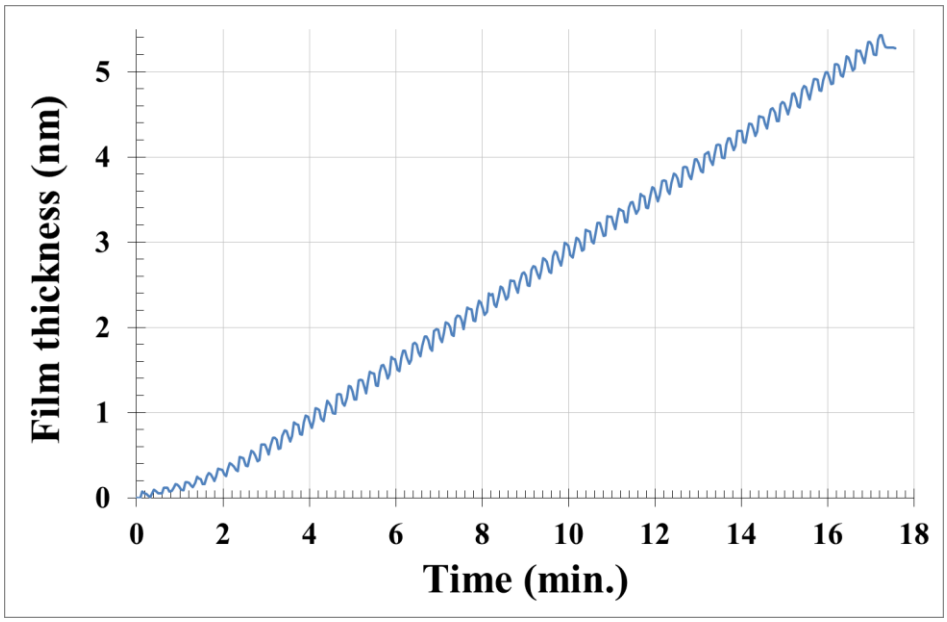

Figure A.2 Optical response of HfO2 growth on a titanium nitride substrate a small nucleation delay is observed but growth shifts to a bulk regime after 9 ALD cycles.

There is a nucleation delay of 12 cycles for the growth of hafnia on the stainless steel substrate, Figure A.3, the native oxide appears to have a very low density of suitable chemisorption sites and hence a low sticking probability. The HfO_2 film starts to nucleate from cycle 13; however, the nucleation phase enters a nonlinear growth phase with increasing GPC for about 11 cycles. This may be as a result of island growth (Volmer-Weber) with the sticking probability at the islands being much more favourable than the substrate; hence the islands areas increases in size with each cycle leading to a nonlinear GPC until the islands coalesce. This is followed by a linear GPC (~1.0 Å) in the bulk regime which is consistent with the bulk GPC on the Si substrate.

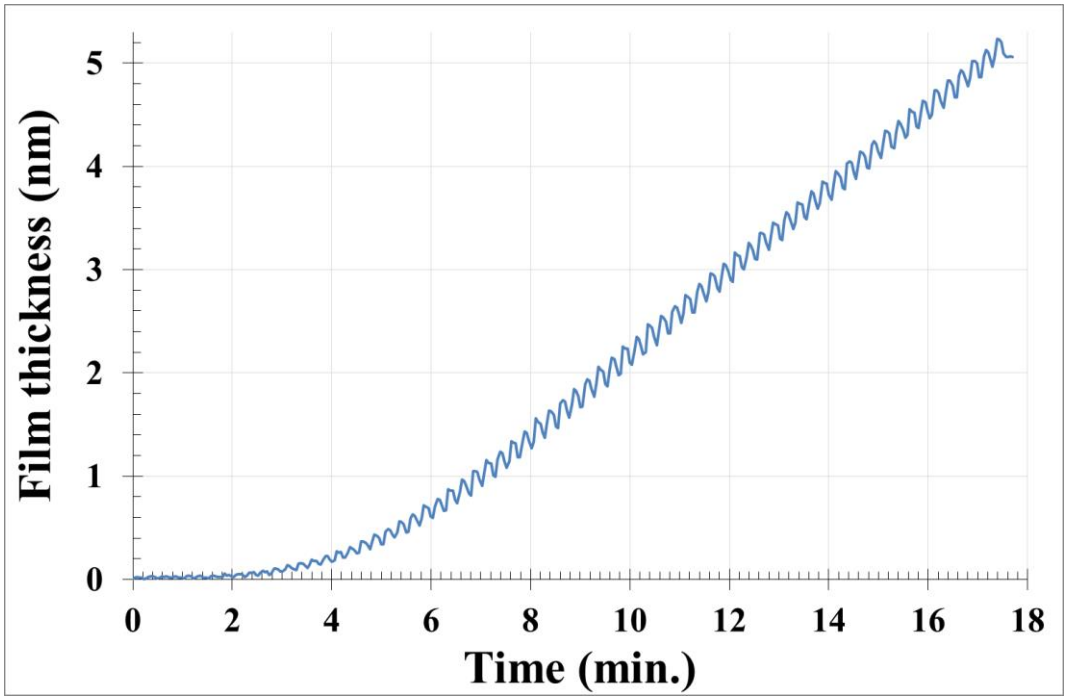

Figure A.3 Optical response of HfO2 growth on a stainless steel substrate 12 cycles of ALD nucleation are required before bulk growth is obtained.

A significant nucleation delay was observed with growth on the InP substrate, Figure A.4, this again indicates a very low density of suitable chemisorption sites. The HfO_2 film takes about 20 cycles to nucleate on the InP native oxide and then enters a nonlinear growth phase with increasing GPC for about 16 cycles. Again, this nonlinear behaviour may be as a result of island growth (Volmer-Weber), this is then followed by a linear GPC (~0.9 Å) in the bulk regime.

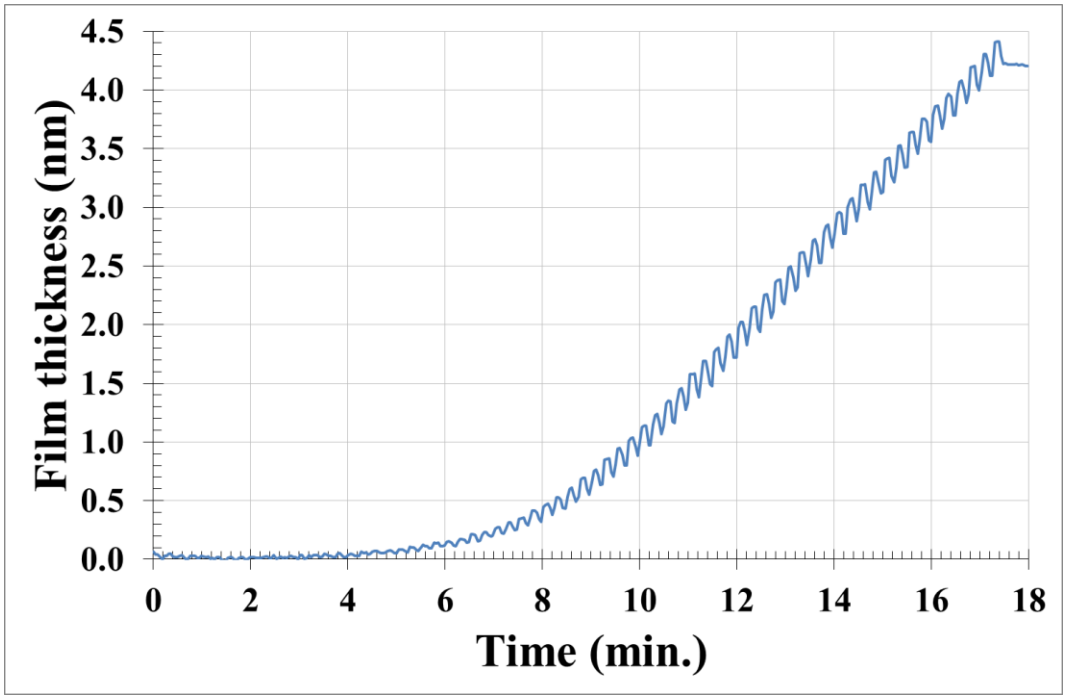

Figure A.4 Optical response of HfO2 growth on an indium phosphide substrate, a significant delay in nucleation is observed followed by a non-linear growth rate until bulk growth is achieved.

The platinum substrate, which has no discernible native oxide, shows no evidence of nucleation retardation, Figure A.5. Although, the HfO_2 film does have two distinct growth phases, initially, the GPC is greater (~ 1.0 Å) for the first 13 cycles and then reduces (~ 0.9 Å) possibly due to densification or crystallisation of the film.

It has been observed that native oxides have a significant influence of the nucleation and growth of HfO_2 by ALD. Stainless steel and InP native oxides have the most pronounced effect while the effect of Si native oxide is minimal by comparison. The trend suggests that the native oxides retard the film growth in the initial nucleation phase, possibly due to a reduction in the density of chemisorption sites on the substrates native oxides.

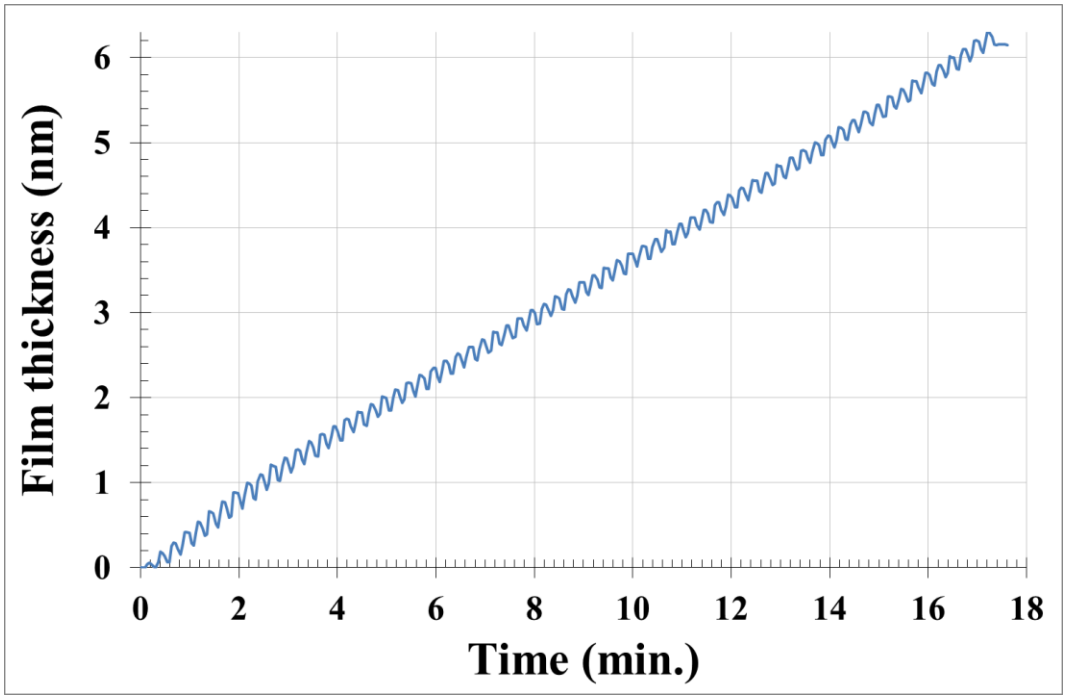

Figure A.5 Optical response of HfO2 growth on a platinum substrate, no nucleation delay is observed.

The growth of HfSiOx on the platinum substrate, in Figure A.6 (top), was initially found to exhibit no nucleation delay with a GPC (~ 1.0 Å). A value that is consistent with the HfO_2 film growth on Pt. However, the nucleation is short lived with the GPC reducing dramatically after the first 2 cycles. This secondary nucleation phase continues for another ~ 33 cycles with an overall increase in the film thickness (~ 0.7 nm). It is proposed that the initial 2 cycles result in the formation of a predominantly silicon-amine interface on the platinum substrate which, due to its unfavourable kinetics for further reaction at this temperature, inhibits the addition of further hafnium or silicon oxide. It has been previously shown that hafnia can catalyse the reaction of silicon amides and conversely that incomplete reactions of silicon amides inhibit the growth of further oxide from metal amides. Thus in order to successfully grow the hafnium silicate fine tuning of the gas phase metal precursor ratio is of

paramount importance, particularly at the nucleation step where excessive TDMAS will effectively poison the growth process. After ~ 35 cycles the film enters a linear bulk growth regime with a large GPC (~ 2.4 Å). This value is higher than expected and the bulk growth mechanism for this film is not fully understood but we suggest that the small fraction of hafnia sites increases through the secondary nucleation until growth can proceed. As seen in Figure A.6 (bottom), on TiN (with native oxide) the nucleation inhibition is complete with no growth even after 30 cycles. Again, the Si molecules are thought to play an important role in preventing nucleation of the film.

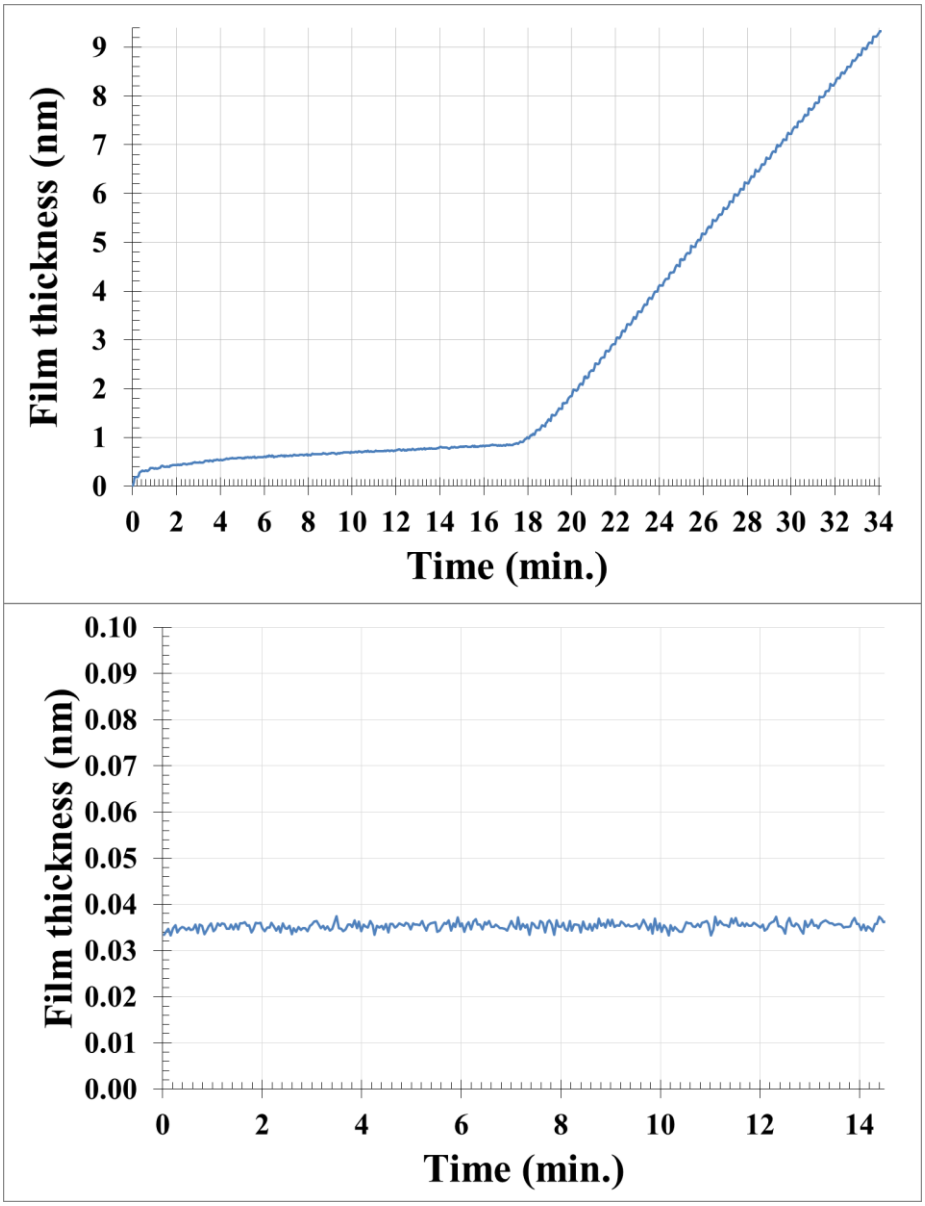

Figure A.6 Optical response from a HfSiOx film grown by PEALD on platinum (top) and titanium nitride (bottom). A complex two stage nucleation process is observed with a platinum substrate, no growth is observed on TiN.

The Al_2O_3 film grown on $In_{0.53}Ga_{0.47}As$ by thermal ALD nucleates immediately (from the first cycle) on both the substrate with native oxide and a 10% $(NH_4)_2S$ etch. The ellipsometry of these two growths are illustrated in **Error! Reference source not**

found.. Although the linear bulk regime GPC is ~ 0.8 Å for both substrates there are obvious differences between the two systems The native oxide substrate has a longer nucleation time (10 cycles) than the etched substrate (4 cycles). This results in an Al_2O_3 film thickness of ~ 3.6 nm on the native oxide substrate and a film thickness of ~ 3.9 nm on the etched substrate. This again leads to the conclusion that nucleation is inhibited by native oxides through a reduced density of chemisorption sites such as hydroxyl groups.

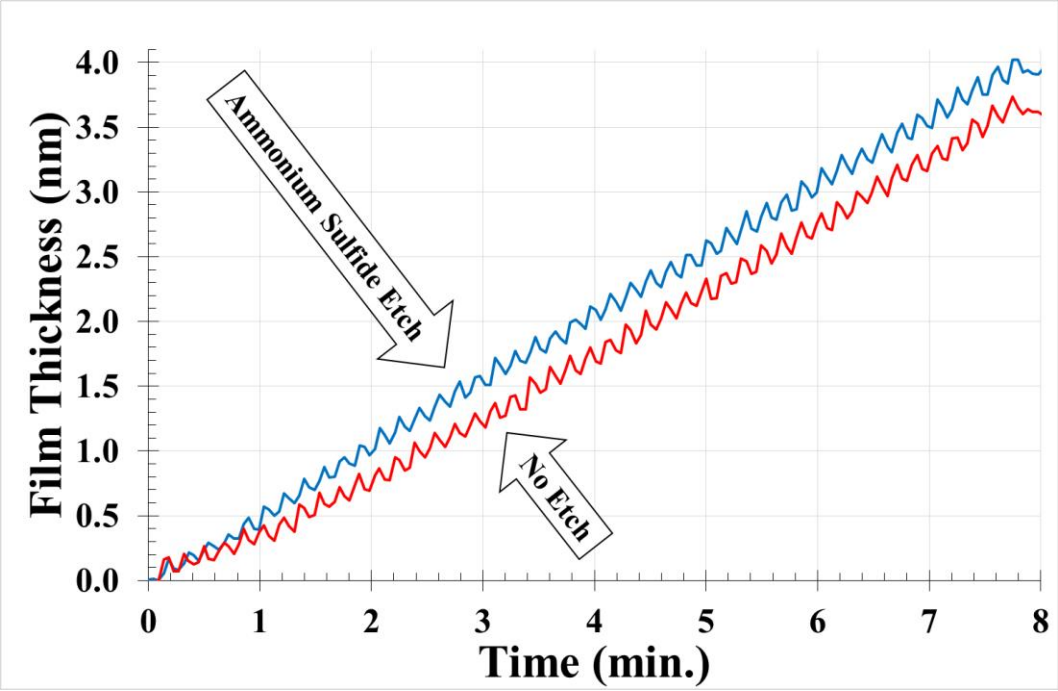

Figure 7 Optical response of thermally grown Al2O3 on InGaAs with and without an (NH4)2S etch step. Note that the wet chemical etch improves the nucleation of the oxide growth.

B.4 Conclusions

The thermal ALD of HfO_2 is influenced by native oxides on silicon, titanium nitride and indium phosphide which appear to retard the nucleation of the dielectric.

However, on the platinum substrate without any native oxide the HfO_2 nucleates immediately with its refractive index response changing after ~ 1nm growth presumably due to densification or crystallisation of the material.

The nucleation of PEALD of the mixed metal oxide HfSiOx appears strongly influenced by substrate choice and the reactivity of the metal precursors. Evidence that supports the retardation of material growth by the TDMAS precursor was observed.

Thermal ALD of Al_2O_3 on $In_{0.53}Ga_{0.47}$ As, which had been wet chemically etched by $(NH_4)_2S$ solution, demonstrated a small but significant improvement to the linearity of growth relative to the equivalent oxide grown on the native oxide. Such an observation is in keeping with the improved electrical performance observed when etching prior to growth of these ultrathin devices.

With all of these preliminary studies caution is required when interpreting, a change in optical response should not be used as a direct measure of growth rate as optical response can also be a measure of composition or crystallinity. Hence, further work is required to correlate the observed ellipsometry data with physical parameters such as thickness (microscopy), chemical composition (x-ray photoelectron spectroscopy) and electrical performance.